Dipl.-Ing. Johannes Raith

Risk Assessment of Power Transformers under the Influence of Geomagnetically Induced Currents (GIC)

DOCTORAL THESIS
to achieve the university degree of
Doktor der technischen Wissenschaften

submitted to
Graz University of Technology

Supervisor
Univ.-Prof. Dr.-Ing. Uwe Schichler
Institute of High Voltage Engineering and System Management
Graz University of Technology, Austria

External Examiner: Prof. Dr. Johan H. Enslin
Department of Electrical and Computer Engineering, Clemson University, USA

Graz, October 2019

AFFIDAVIT

I declare that I have authored this thesis independently, that I have not used other than the declared sources/resources, and that I have explicitly indicated all material which has been quoted either literally or by content from the sources used. The text document uploaded to TUGRAZonline is identical to the present doctoral thesis.

21.10.2019,

Date, Signature

CONTENT

ACKNOWLEDGEMENTS V

ABSTRACT VII

ZUSAMMENFASSUNG (ABSTRACT IN GERMAN) IX

1 INTRODUCTION 1

1.1 Background 1

1.2 Objectives 1

1.3 Thesis Structure 2
- 1.3.1 Fundamentals and solution strategy 2
- 1.3.2 Harmonic calculation 2
- 1.3.3 Hotspot calculation 2
- 1.3.4 Discussion and future work 2

2 FUNDAMENTALS 3

2.1 Solar Activity and Power Grids 3

2.2 GIC problems in the past 4

2.3 Impact of GIC on the operation of power transformers 5
- 2.3.1 GIC characteristics 5
- 2.3.2 Steady-state behavior of power transformers under DC 6
- 2.3.3 Transient behavior of power transformers under DC 7

2.4 Other source for DC occurrence in power grids 9

2.5 Risk Assessment Methods 10
- 2.5.1 General 10
- 2.5.2 State of the Art 10

2.6 Summary 12

3 SOLUTION STRATEGY 13

3.1 Overview 13

3.2 Classification of power transformers 13
- 3.2.1 General 13
- 3.2.2 Core-Type T1 14
- 3.2.3 Core-Type T2 15
- 3.2.4 Core-Type T3 15
- 3.2.5 Core-Type T4 15
- 3.2.6 Core-Type T5 16

3.3 Development of a risk assessment model for transformers 17
- 3.3.1 Calculation of the harmonic behavior 17
- 3.3.2 Calculation of the hotspot behavior 17

3.4 Model verification 18

4 HARMONIC CALCULATION 19

4.1 Basics 19
4.1.1 Example 19
4.1.2 Solving of the equation system 21

4.2 Single-Phase Transformers 22
4.2.1 Model for core designs with one wounded limb 22
4.2.1.1 Electro-magnetic network for Core-Type T1 22
4.2.1.2 Determination of magnetic resistances 23
4.2.2 Model for core designs with two wounded limbs 25
4.2.2.1 Electro-magnetic network for Core-Type T2 25
4.2.2.2 Electro-magnetic network for Core-Type T4 26
4.2.3 Analysis 27

4.3 Three-Phase Transformers 31
4.3.1 Model for core designs with three wounded limbs 31
4.3.1.1 Electro-magnetic network for Core-Type T3 31
4.3.1.2 Electro-magnetic network for Core-Type T5 32
4.3.2 Analysis 32

4.4 Verification 36
4.4.1 DC experiments with single-phase transformers 36
4.4.1.1 Measurement setup 36
4.4.1.2 Comparison of test results with simulations 38
4.4.2 DC experiments with 3-phase transformers (T3 Core-Types) 41
4.4.2.1 Measurement setup 41
4.4.2.2 Comparison of test results with simulations 42
4.4.2.3 Behavior of fundamental reactive power 43
4.4.3 DC experiments with 3-phase transformers (T5 Core-Type) 44
4.4.3.1 Measurement setup 44
4.4.3.2 Comparison of test results with simulations 46

4.5 Alternative calculation method based on Ψ-I curve 46
4.5.1 Calculation procedure for single-phase cores 46
4.5.2 Calculation procedure for T3 Core-Types 48
4.5.3 Basic transformer parameter to determine DC behavior 48

4.6 Comparison of calculation methods and measurements 49
4.6.1 Single-Phase transformers 49
4.6.2 Three-Phase transformers with T3 cores 50

4.7 Summary 50

5 HOTSPOT CALCULATION 53

5.1 Thermal model for tie bars 53
5.1.1 Model approach 53
5.1.2 Calculation of tie bar losses 55
5.1.2.1 Parameter for an electro-magnetic tie bar model 57
5.1.2.2 Behavior of an electro-magnetic tie bar model 57
5.1.3 Consideration of inhomogeneous loss distribution 58
5.1.4 Analysis 59

5.2 Verification 60
5.2.1 Experimental setup 60
5.2.2 Test results vs. simulation (Hotspot Test no. 1) 60
5.2.2.1 Comparison of magnetic flux in tie bar 60
5.2.2.2 Calculated tie bar losses during DC experiment 62
5.2.2.3 Comparison of tie bar temperatures 62

5.2.3 Influence of voltage wave form on temperature 63
5.2.4 Further DC experiments to verify the hotspot calculation 65
5.2.5 Analysis 66
    5.2.5.1 Statistic – measured vs. calculated hotspot temperature 66
    5.2.5.2 Resume 67

5.3 Summary 69

6 DISCUSSION 71

6.1 Grid stability 71

6.2 DC withstand capability of transformers 72

6.3 GIC withstand capability of transformers 73

6.4 Simplification of GIC signatures for requirements in transformer specifications 75

6.5 Screening criteria for GIC affected transformers 77

7 FUTURE WORK 79

8 SUMMARY 81

9 REFERENCES 83

APPENDIX A – SYMBOLS 87

APPENDIX B – MAGNETIC RESISTANCES 91

APPENDIX C – EXPERIMENTS TO VERIFY HOTSPOT CALCULATION 95

APPENDIX D – LIST OF FIGURES 99

APPENDIX E – LIST OF TABLES 103

Acknowledgements

First, I like to express my gratitude to Prof. Uwe Schichler, head of the High Voltage Engineering and System Management institute at Graz University of Technology, Austria. His professional supervising and expertise improved my work and helped me to complete this thesis.

Furthermore I express my thank to Mr. Reinhard Gruenseis, Head of the Test Laboratory at Siemens AG, Transformers Weiz, for enabling detailed and non-standardized GIC experiments on several power transformers. Such kind of measurements bring unique technological knowledge and lead to highest quality in the products. I also want to thank the complete team of the test laboratory for their excellent support, with special thanks to Mr. Markus Lammer, Mr. Ewald Weitzer and Mr. Guenter Karrer for their fruitful conversations and assistance.

My sincere thanks go to Mr. Martin Stoessl, Mr. Gerald Leber and Mr. Mario Scala who encouraged me to make this thesis and have given me the opportunity to do the research. Their expertise and support are always an enrichment in this field of research.

Finally, I would also like to thank my complete family, my wife Marlies and our two children who always motivate me.

Abstract

The reliability of transformers is a topic old as the transformers themselves. To reach highest product dependability, the behavior of power transformer must be also known during abnormal operating conditions, because then suitable countermeasures can be set in order to avoid power outages or damages at the transformer. Common stresses are overload situations in the power grid or malfunctions of required cooling equipment. However, also environmentally impacts, like the occurrence of Geomagnetically Induced Currents (GIC) in the transmission lines influences the operation of power transformers. These currents occur during solar storms in power grids due to a variation of the earth’s magnetic field. This thesis identifies the risks of such GIC events for power transformers and shows how the impacts at different types of transformers can be determined.

For such a risk assessment, previous methods use mostly generic approaches which consider only some rough transformer information. This thesis uses another approach and shows how the design of a specific transformer can be considered in order to allow a qualified design-specific GIC risk assessment. For this reason, calculation models for different critical effects due to GIC are explained. The first one is a model to calculate the additional harmonics in case of GIC in a transformer winding. GIC events in the past showed that the occurrence of harmonics is one of the most critical effect due to GIC which can lead to a complete instability of the power network. The second calculation model explained in this thesis, allows a simulation of the additional heating in the transformer during a GIC storm. In that way, the risk of increased temperatures, in a certain power transformer and for a certain GIC profile, can be evaluated. Such heating problems were also recorded during GIC events in the past.

In order to ensure the validity of the developed simulation models, several GIC experiments with different power transformer designs were carried out in a test laboratory during this thesis. A DC source was used to simulate different GIC profiles and AC/DC transducer measured the voltage and current wave forms to validate the harmonic calculation. To measure the heating in the transformers, also temperature sensors were installed in the tested transformers. Moreover, flux measuring loops were placed at critical locations, in order to compare also the calculated and measured magnetic flux, because this additional stray flux is the reason of the heating in case of GIC.

This means by the help of this thesis, measures for a safely operation of power transformers can be identified and the risk of GIC can be evaluated.

Zusammenfassung (Abstract in German)

Die Zuverlässigkeit von Transformatoren ist ein Thema, das so alt ist wie die Transformatoren selbst. Um höchste Produktzuverlässigkeit zu erreichen, muss das Verhalten von Leistungstransformatoren auch unter abnormalen Betriebsbedingungen bekannt sein. Nur damit können geeignete Gegenmaßnahmen getroffen werden, um Stromausfälle oder Beschädigungen am Transformator zu verhindern. Allgemein bekannte Belastungen sind Überlastsituationen im Stromnetz oder Funktionsstörungen der erforderlichen Kühlgeräte. Jedoch auch Umwelteinflüsse, wie das Auftreten von Geomagnetisch Induzierten Strömen (GIC) in den Übertragungsleitungen, können den Betrieb von Leistungstransformatoren beeinflussen. Diese Ströme treten in Stromnetzen während der Dauer von Sonnenstürmen aufgrund einer Änderung des Erdmagnetfelds auf. Diese Dissertation identifiziert die Risiken solcher GIC-Ereignisse auf Leistungstransformatoren und zeigt, wie die Auswirkungen für verschiedene Arten von Transformatoren bestimmt werden können.

Bisherige Methoden für eine Risikobewertungen durch GIC verwenden meist generische Ansätze, welche nur einige grobe Transformatorinformationen berücksichtigen. Diese Arbeit verfolgt einen anderen Ansatz und zeigt, wie das Design eines bestimmten Transformators berücksichtigt werden kann, um eine qualifizierte, design-spezifische Bewertung des GIC-Risikos zu ermöglichen. Aus diesem Grund werden in dieser Studie Berechnungsmodelle für die Haupteffekte durch GIC erläutert. Das erste ist ein Modell zur Berechnung der zusätzlichen Oberschwingungen im Falle von GIC in einer Transformatorwicklung. GIC-Ereignisse in der Vergangenheit haben gezeigt, dass das Auftreten von Oberwellen einer der kritischsten Effekte durch GIC ist und zu einer vollständigen Instabilität des Stromnetzes führen kann. Das zweite erläuterte Berechnungsmodell in dieser Arbeit ermöglicht eine Simulation der zusätzlichen Erwärmung im Transformator während eines GIC-Sturms. Auf diese Weise kann auch das Risiko durch erhöhte Temperaturen für einen bestimmten Leistungstransformator bei einem bestimmten GIC-Profil bewertet werden. Solche Erwärmungsprobleme wurden ebenfalls immer wieder bei GIC-Ereignissen in der Vergangenheit dokumentiert.

Um die Gültigkeit der Simulationsmodelle zu gewährleisten, wurden im Rahmen dieser Arbeit mehrere GIC-Experimente mit unterschiedlichen Leistungstransformatoren in einem Prüflabor durchgeführt. Eine Gleichstromquelle wurde verwendet, um verschiedene GIC-Profile zu simulieren, und AC/DC Wandler maßen die Spannungs- und Stromwellenformen, um die Berechnung der Oberwellen zu validieren. Zur Messung der Erwärmung wurden auch Temperatursensoren in den geprüften Transformatoren eingebaut. Darüber hinaus wurden Flussmessschleifen an kritischen Stellen platziert, um den berechneten und gemessenen magnetischen Fluss miteinander zu vergleichen, da dieser zusätzliche Streufluss der Grund für die zusätzliche Erwärmung bei GIC ist.

Mit Hilfe dieser Arbeit können also Maßnahmen für einen sicheren Betrieb von Leistungstransformatoren abgeleitet werden und das Risiko durch GIC bewertet werden.

1 Introduction

1.1 Background

The reliability of the electric infrastructure is one of the most important topics in the field of power engineering. Electricity must be available for private households and the industry for 24 hours each day and seven days per week. Possible outages are always associated with enormous economic loss for the utility and the public life. Consequently an advanced power system management is essential to minimize the risk of power blackouts.

A key element of the infrastructure is the transmission system. It is responsible for the energy flow from power plants up to the end users. To handle this energy transport different components are necessary like power transformers, phase shifters and shunt reactors. All these devices are interacting in complex intermeshed power grids with long transmission lines and disturbances in one element can destabilize the whole network. Therefore the behavior of each electrical device should be known, and the condition constantly monitored to manage possible abnormal situations.

Common burdens in power grids are overloading, surges or malfunctions of required cooling apparatus for the equipment. For such conditions monitoring systems and assessment tools are already well advanced to control the performance. However, also unexpected environmentally impacts like the occurrence of Geomagnetically Induced Currents (GIC) can cause critical conditions in the transmission system. These are unwanted currents in the power system caused by solar activity. The consequences of these currents are additional harmonics in the system, together with over-voltages and rising temperatures in the affected equipment. For such events the development of risk assessment tools is not finished and therefore this thesis should bring a progress to evaluate the effects of solar activity on electrical equipment.

1.2 Objectives

The effects of GIC on the power system are well described in [1], but calculation models for a suitable simulation are missing. Consequently the main target of this thesis is the development of design-specific methods to evaluate the risk of GIC events for different types of power transformers. That means that in contrast to existing methods the individual design should be considered in order to calculate critical GIC impacts like rising temperatures or additional harmonics. To reach this ambition, mechanical components in transformers are identified which are stressed by GIC, and simulation models are developed which consider the relevant design properties of the transformer. As a result, measures applicable during the design stage can be derived to ensure a safe transformer operation in case of a solar storm.

Figure 1 illustrates the idea of an innovative GIC risk assessment model. The method uses different calculation models which allow a simulation of the transformer behavior under the influence of GIC. Varying operational conditions and fluctuating GIC magnitudes are taken into account. In this way the risk of different GIC scenarios can be evaluated and the usability of the model in online applications, to monitor the electrical equipment during a critical solar storm, is also possible.

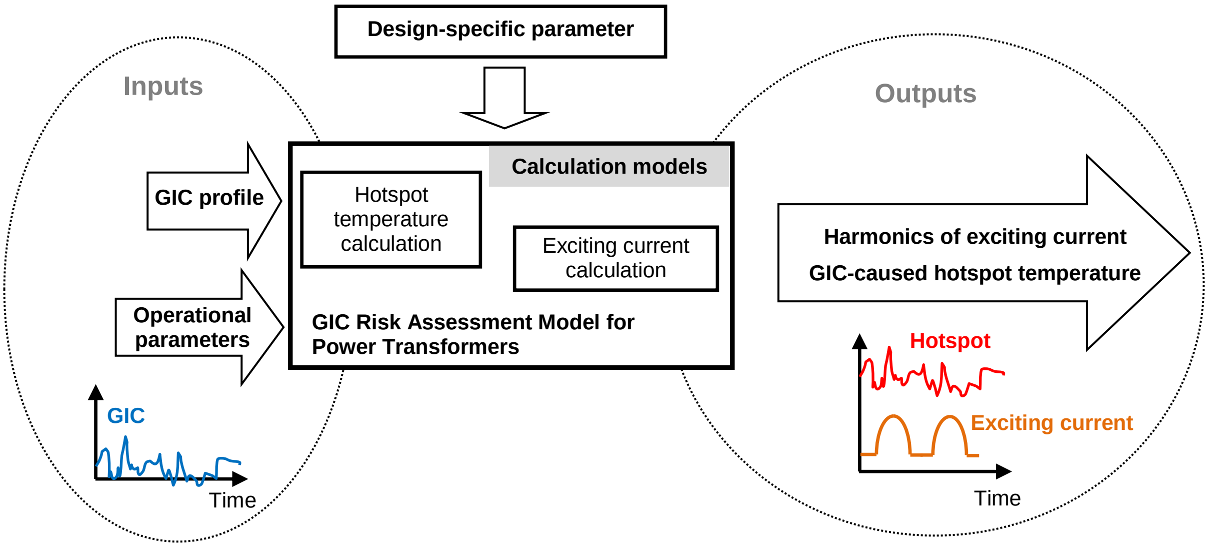
Design-specific parameter
Inputs
GIC profile
Operational parameters
GIC
Time
Calculation models
Hotspot temperature calculation
Exciting current calculation
GIC Risk Assessment Model for Power Transformers
Outputs
Harmonics of exciting current
GIC-caused hotspot temperature
Hotspot
Exciting current
Time

Figure 1: Idea of a design-specific risk assessment method for GIC effects

1.3 Thesis Structure

1.3.1 Fundamentals and solution strategy

The first chapters provide some background information and fundamentals about the topic. At the beginning the source of GIC, the interconnection to the electrical power system and significant GIC-caused problems in power grids are shown. Afterwards the typical impact of GIC on the operation of power transformers is demonstrated. Based on these results the requirements for a suitable risk assessment method are discussed and compared with existing solutions in this field of research. An overview of the whole work in this thesis and the planned developments are given in the solution strategy chapter.

1.3.2 Harmonic calculation

This chapter demonstrates how to calculate the wave form of the exciting current in a transformer if a GIC magnitude is present in the winding. Based on the wave form the harmonics can be easily determined. In order to cover different types of transformers several calculation models and their parameterization are discussed. To ensure the validity of the simulation models, measurement results of different DC experiments are compared with corresponding simulations.

1.3.3 Hotspot calculation

In order to evaluate the hotspot temperature in transformers under GIC a thermal model for significant stressed transformer components is developed in this chapter of the document. To calculate the temperatures, also the losses in the affected components must be known. Consequently not only a temperature model is demonstrated, also a method to calculate the losses for a given GIC magnitude is illustrated in parallel. To verify these developed calculation techniques hotspot and flux measurements at different transformers were performed. Therefore measurement and calculation results are analyzed and compared with each other.

1.3.4 Discussion and future work

To conclude the thesis the results of all investigations are summarized in respect to give answers to the major questions in the field of risk assessment for power transformer under GIC. This includes the grid stability as well as the DC withstand capability of the equipment. At the end some future work in this field of research is suggested.

2 Fundamentals

2.1 Solar Activity and Power Grids

The sun generates an incessantly flow of electric charged particles into the outer space which is known as solar wind. However, the solar activity is not constant and subjected to strong variations. This dynamic behavior of the sun is reflected by the periodic occurrence of spots on the sun surface which is observed since centuries. These spots are regions on the sun with extremely high magnetic fields and lower temperatures than the surrounding areas as explained in [2] and [3]. Figure 2 illustrates that the number of spots changes from a solar maximum to a solar minimum back to a maximum within about 11 years. Within these cycles are enormous events on the sun possible like Coronal Mass Ejections (CME) or Coronal Hole Streams (CHS). Some of them correlate with highly spotted time periods and other ones occur more often around the solar minimum [2]. Nevertheless, both events cause strong variations in the solar wind. Such fluctuations in the solar wind are named solar storms and influence the electric infrastructure on earth. The connection is given by the earth's magnetosphere, because changes in the solar wind are always linked with changes in the magnetic field of the earth. One consequence of such geomagnetic field disturbances is the occurrence of Geomagnetically Induced Currents (GIC) in power systems.

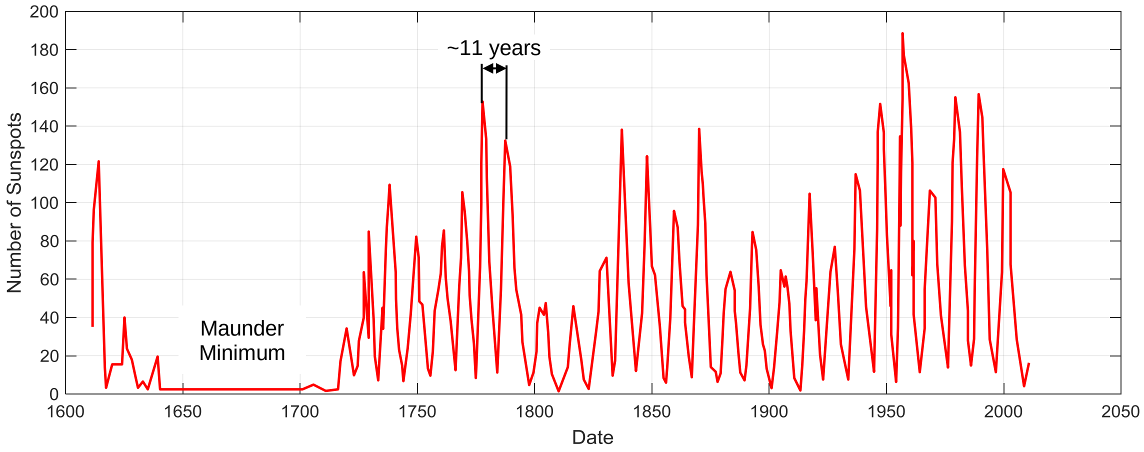

Figure 2: Yearly average sunspot numbers (1960-2010) [4]

Figure 3 demonstrates a simplified GIC flow within a section of a power grid with two transformers. The disturbances in the magnetosphere result in an earth surface potential between the grounded neutrals of the high-voltage windings. The consequence of these induced voltages is a GIC flow from the grounded neutral into the transformer winding and via the transmission lines and the second transformer winding back to the ground. Problems due to GIC were already documented in the past. Section 2.2 of this thesis presents a brief overview of typical failures and problems occurred in power systems due to GIC events.

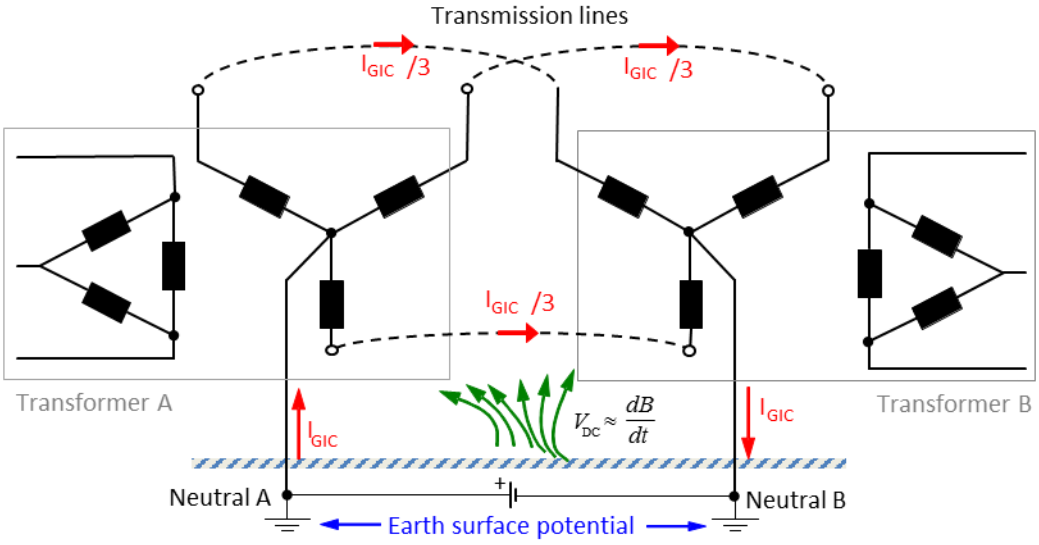

Figure 3: Simplified flow of a Geomagnetically Induced Current (GIC)

2.2 GIC problems in the past

Table 1 summarizes different GIC-related problems in power grids. Other observed issues with electrical equipment during solar storms in the last decades can be found in [5], [6] and [7]. However, it can be seen that all described problems are linked to two major solar events happened in 1989 and in 2003. The consequences of these events were similar. During the occurrence of GIC additional harmonics in the currents and voltages were observed in the system. This led to malfunctions of electrical devices in the power grid because they were not able to handle the extraordinary harmonic content. For instance this was the reason for the black-out of the Hydro-Quebec grid in Canada as well as for the power outage in the city of Malmö in Sweden. A brief overview of potential harmonic impacts is shown in [8]. In parallel to the voltage and current fluctuations, the GIC events in the past caused in some electrical equipment also additional stresses due to higher temperatures. The worst cases are damages within the device as it happened in a power transformer in the PSE&G grid or in two power transformers in the UK system.

All in all the information of Table 1 illustrates that two effects are very important to manage the risk for electric equipment due to GIC, and that the adequate management of these effects can ensure a safe operation during a solar storm. On the one hand the occurrence of additional harmonics must be considered, and on the other hand the effect of rising temperatures in the affected devices must be controlled.

Table 1: Several GIC-caused problems in power grids

Date	Country	Problem description	Ref.
1989 1991	Canada	In 1989 the power grid of Hydro-Quebec was affected by a complete black-out due to a massive coronal mass ejection. The resulting GIC led to current harmonics and over-voltages in the transmission system and caused a tripping of several static compensators. These devices are essential for the grid stability and the consequence was an uncontrollable instability of the power grid.	[9]
1989	US	A winding overheating was experienced in a GSU power transformer. The transformer did not fail during the solar storm, but significant gassing started with the GIC event. After a few weeks the transformer was taken out of service and a winding damage was observed caused by increased winding currents during the additional GIC loading.	[10]
1982 1989 1991 2003	UK	A power system in UK was influenced by GIC several times, especially during the solar storms in 1982, 1989, 1991 and 2003. The effects of these events included large reactive power swings, voltage dips and damaging of two identical 240 MVA power transformers.	[11]
1992	US	In May 1992 a significant transformer heating was observed during a GIC event. The tank wall temperature increased up to about 175 °C within about 10 minutes. The literature did not discuss any failure of the transformer in this period, but it shows the potential of additional heating in a transformer due to GIC.	[12]
2003	Sweden	End of October 2003 a series of Coronal Mass Ejections happened on the sun. These events are known as Halloween GIC storms. On 30th October at 20:07 UT a 130 kV line tripped in the southern of Sweden. This led to a 50-min blackout in the city of Malmö. The reason was the tripping of a relay which was too sensitive to the additional harmonics caused by the GIC.	[13]

2.3 *Impact of GIC on the operation of power transformers*

2.3.1 GIC characteristics

To clarify the impact of GIC on electrical power transformers, the characteristic of GIC profiles is analyzed in this chapter and the properties which are influencing the operation of power transformers are pointed out. Figure 4 demonstrates two examples of GIC signatures in grounded neutrals of power systems. The left side represents a moderate event with only some peaks, whereas the right part of the graphic shows a more intense GIC storm. However, in both cases DC fluctuations can be observed. Monitoring systems which are able to measure such DC pulses in the transformer neutrals show that such GIC phenomena are possible all over the world. Examples for different countries are discussed in [14], [15], [16], [17], [18], [19] and [20].

The duration of the events captured in Figure 4 is about 120 minutes, but literature indicates that such DC fluctuations can last up to several days [21]. Within this time period high DC pulses with magnitudes up to a few hundred of Ampere are possible whereas especially higher-latitude countries are primarily affected. Nevertheless, the exact intensity depends on a lot of parameters like the strength of the solar flare, the latitude of the transformer, the grid structure, etc. as shown in [22]. Furthermore a look in the history indicates that solar flares may be much more intensive as the recorded ones in the last decades. An example of such a super-flare is the Carrington Event which happened 1859 [23]. However, a detailed forecast of GIC events is hardly possible, but Figure 4 demonstrates that GIC events are always potential sources for additional DC components in transformers with grounded windings.

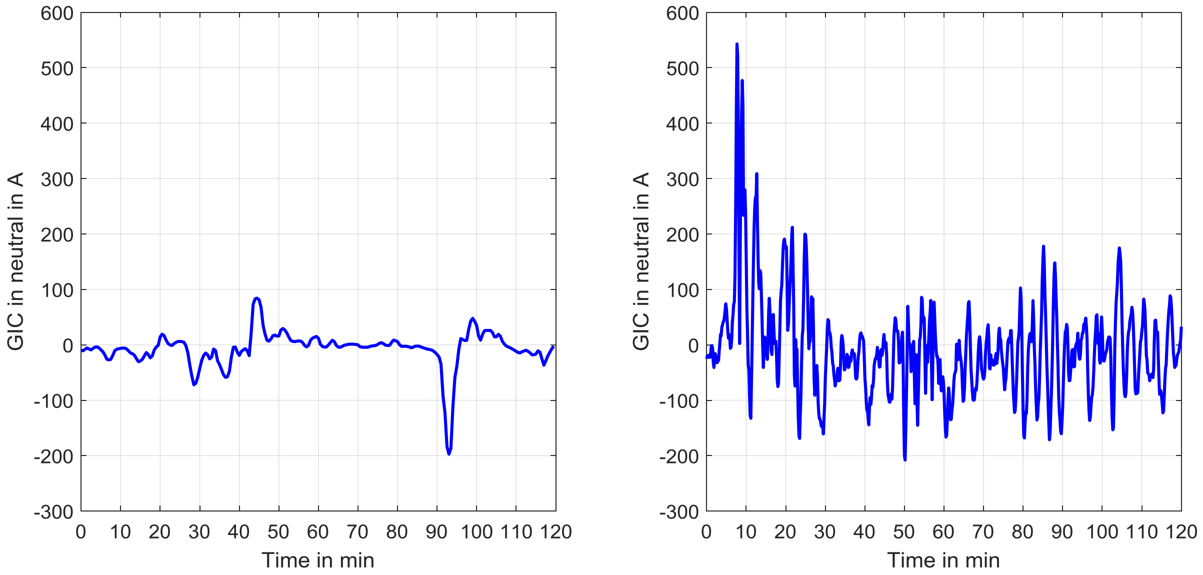

Figure 4: Potential GIC profiles in grounded neutrals [24]

2.3.2 Steady-state behavior of power transformers under DC

In general electrical devices like power transformers or shunt reactors have copper coils wound around an iron core, with the core carrying the required magnetic flux. Under normal conditions a transformer operates under a well-defined AC voltage which results also in an AC flux in the core together with a very low exciting current as demonstrated in Figure 5.

The occurrence of DC pulses in the transformer winding result in DC offsets in the magnetic flux of the core. As a result the saturation level of the core material can be reached ones per cycle and this leads to a high peak in the exciting current and significant additional harmonics. In the power industry this effect is commonly known as part-cycle core saturation and the discussed problems in chapter 2.2 of this thesis have their origin by this kind of core saturation. However, as already discussed not alone the harmonic content is increased with a DC current component in the winding. In parallel to the core saturation magnetic stray flux spills out of the core and causes additional heating in the steel parts. Further effects of DC bias in power transformers are an increased noise level and higher core losses as shown in [25] and [26]. Both of them start already at very low DC levels, but for a safe operation during GIC are these effects not really an issue and also techniques to compensate the consequences of very low DC bias are existing as demonstrated in [27] and [28]. Therefore this thesis focuses on critical consequences due to GIC magnitudes like the harmonic generation and the additional heating.

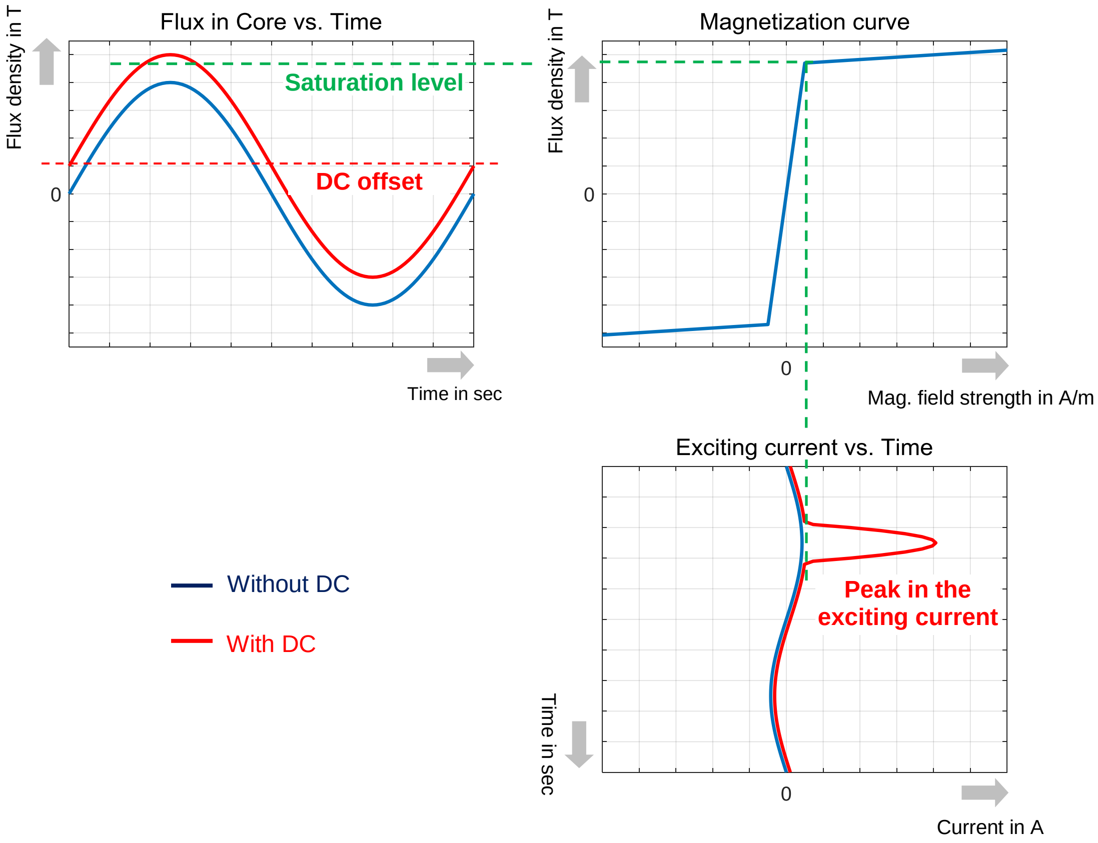

Figure 5: Disorder of nominal transformer operation due to DC [29]

2.3.3 Transient behavior of power transformers under DC

To verify the impact of GIC on power transformers it is also essential to look at the transient characteristics and not only at the steady-state condition as it is demonstrated in Figure 5. The reason is that a GIC event is not a constant DC level over the time, it is more a series of short DC pulses. Therefore the temporal transformer behavior during such DC pulses must be considered. This can be clarified with the analyzation of a transient transformer behavior where in addition to the nominal operation with an AC voltage also an additional DC voltage is applied at the grounded winding. Figure 6 illustrates a potential electrical circuit for such an investigation, which can be done with transient electro-magnetic simulation models as shown in [30] or [31].

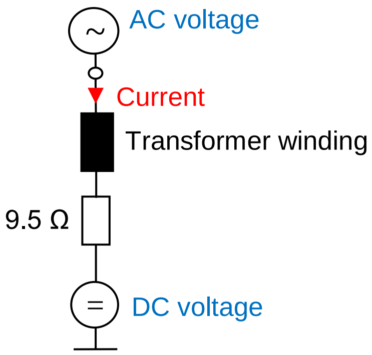

Figure 6: Example of a grounded transformer winding with AC and DC excitation

To demonstrate an example for the transient electro-magnetic response of a power transformer, Figure 7 shows simulation results of a 116 MVA, 60 Hz single-phase unit. The left part of the graphic illustrates the complete simulation period of 12 seconds and the right part one period in the steady-state condition at the end of the simulation time. It can be seen, that after 3 seconds nominal AC operation an additional DC voltage is applied at the grounded neutral. However, nothing happens with the exciting current at this moment, because the DC component of the core flux needs several seconds to reach its steady-state flux condition. Therefore the exciting current of the transformer is still very low when the DC voltage pulse starts. The generation of significant harmonics in the exciting current begins just at this moment when the saturation level of the core material is reached. It is clear, that only after this moment additional losses can occur in transformer components caused by the escaping stray flux from the core.

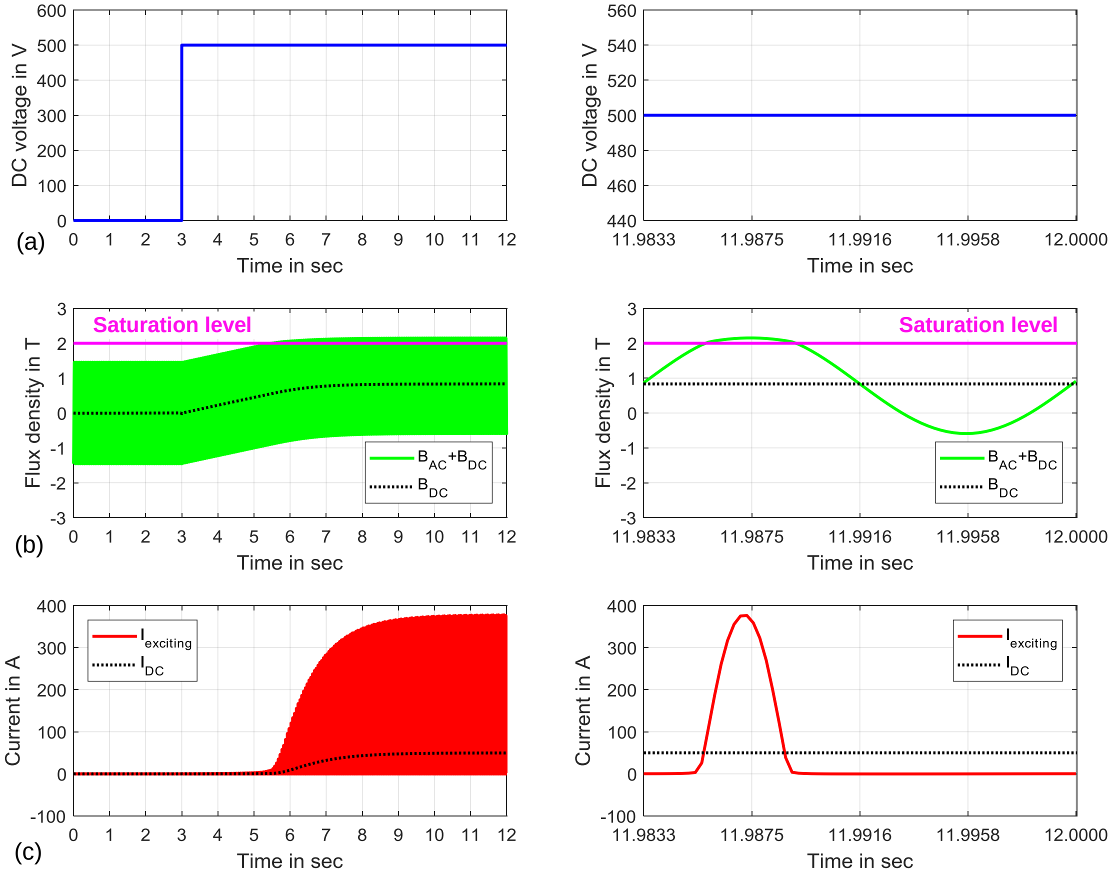

Figure 7: Transient behavior of flux in a transformer core in case of an additional DC excitation – (a) DC voltage at neutral, (b) Flux density in core, (c) Exciting current in winding

Nevertheless, the heating of internal transformer components takes much more time as the needed time to reach the core saturation. Experiments in [32] indicate durations in the range of dozens of minutes in order to reach the thermal steady-state temperature rise in case of an additional DC current in the winding. Figure 8 shows such an observed heating process after the injection of a DC current in the high-voltage winding of a transformer. The DC level in this experiment was applied for more than 30 minutes to reach the thermal steady-state condition of the hotspot temperature. However, such solitary long DC pulses are not expected during solar storms, but Figure 4 in this thesis demonstrated that the whole series of short DC pulses can easily last several hours or even longer. Consequently, for a correct determination of the heating inside of an affected power transformer the effect of the entire GIC profile should be considered.

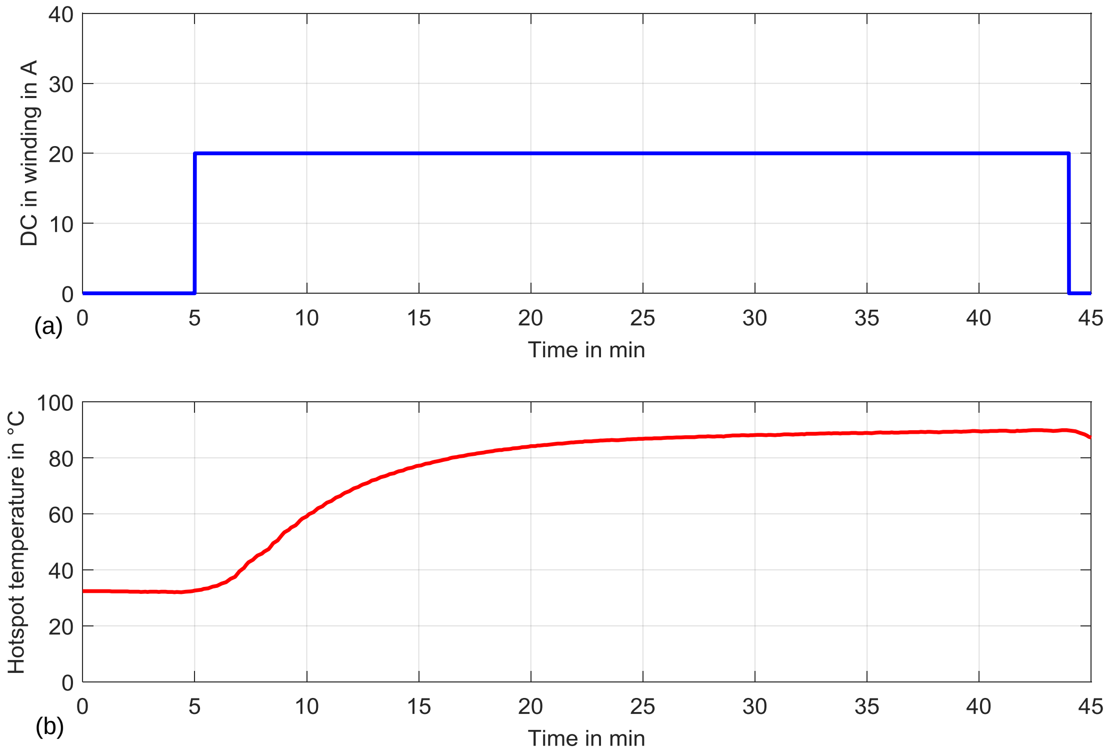

Figure 8: Transient behavior of a hotspot temperature in case of an additional DC current in a transformer winding – (a) Additional DC current in the winding, (b) Observed increase of hotspot temperature in [32]

2.4 Other source for DC occurrence in power grids

The GIC phenomenon is only one possible source for a DC current in a transmission system. Another well-known origin for the occurrence of DC in power grids is the interaction between AC and DC lines which are close together [33]. An example for such a configuration is a hybrid transmission system as demonstrated in Figure 9.

In such hybrid power lines the AC and DC system are sharing the same transmission tower. The consequence are long and parallel conductors where partial discharge can occur around the HVDC line in the air. During this process free charge charrier are generated which are captured by the AC system [34]. This leads to unwanted DC currents in the AC lines which lead to the same DC effects in power transformers as discussed in chapter 2.3.2 and chapter 2.3.3.

Test results in [35] indicate that such DC currents are in the range between 500 mA and 5000 mA per 100 km transmission line. However, the literature illustrates also that the distance between the AC and DC lines, the magnitude of the DC voltage as well as the climate condition (dry/rainy) have an influence on the range of the generated DC current. Nevertheless, the DC levels which are generated by this source are significant smaller than DC pulses which can occur during a GIC event.

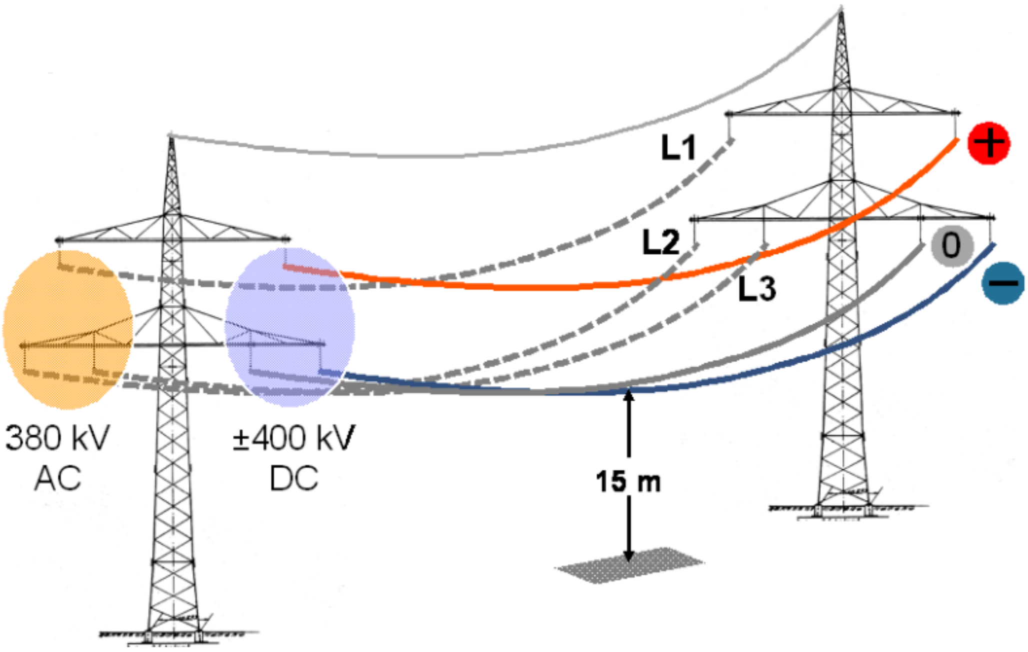

Figure 9: AC/DC hybrid transmission line [36]

2.5 Risk Assessment Methods

2.5.1 General

The illustrated GIC impacts in Figure 7 and Figure 8 indicate the requirements for an adequate assessment method to evaluate the risk of GIC events for power transformers. Based on a certain DC level in a grounded winding, the additional harmonic content in the exciting current and the increased hotspot temperature in the device must be predictable. Furthermore, the method must consider the transient characteristic of GIC profiles, because especially the hotspot heating depends strongly on the duration of the DC pulse. Therefore, the possibility of transient thermal simulations for a given GIC profile should be also included in an advanced risk assessment tool.

2.5.2 State of the Art

The evaluation of potential risks due to GIC in electrical equipment is already a common field in the scientific world. This can be seen by an already existing industrial guide which deals with this topic [1]. In this guide a classification table is present where the total GIC susceptibility for power transformers is separated into four categories and the expected GIC effects for each category are discussed. A summary with results of this literature is given in Table 2 and Table 3.

However, the risk category is only based on some transformer design basics (e.g. the core design) and the GIC magnitude in the winding. Nevertheless, no applicable methods to calculate the GIC effects are provided in [1]. Only a few examples of measured temperatures and calculated harmonics are demonstrated, but a design-based simulation of the behavior for a certain transformer design is not given. Similar is the situation when reference [37] or [38] is studied. Here a risk categorization based on few design information and a method to demonstrate the thermal GIC capability of a power transformer are shown, but models to calculate the hotspot temperatures with DC are missing.

Table 2: Expected GIC effects according to IEEE C57.163

Category I	**Transformers have practically no susceptibility to GIC**
Category II	**Transformers have only a low susceptibility to GIC** Effects: Harmonics are possible under GIC, magnetic modeling is suggested.
Category III	**Transformers have a moderate susceptibility to GIC** Effects: Harmonics and significant heating of structural metallic parts are possible under GIC. Magnetic and thermal modeling of metal parts is suggested.
Category IV	**Transformers have a high susceptibility to GIC** Effects: Harmonics and significant heating of structural metallic parts and windings are possible under GIC. Magnetic and thermal modeling of metal parts and windings is suggested.

Table 3: Transformer susceptibility to the effect of GIC (IEEE C57.163) [1]

	GIC exposure level (amperes per phase)		
Classification of transformer design-based susceptibility	**Low exposure (≤ 15 A)**	**Medium exposure (> 15 A to < 75 A)**	**High exposure (≥ 75 A)**
Not susceptible (A)	I	I	I
Least susceptible (B)	I	II	III
Susceptible (C)	II	III	III
Highly susceptible (D)	II	IV	IV

Another example for a GIC risk evaluation is demonstrated in [22]. This approach considers the transient characteristic of GIC and values for the steady-state hotspot temperature are also indicated for different GIC levels in the transformer winding. An abstract of this literature is shown in Table 4. However, a calculation model for the temperatures is also missing, because the hotspot values in the table are only derived from some measurements and essential design details of the tested transformers are not considered. Furthermore also the thermal condition in the transformer tank is not taken into account.

All in all, important research gaps are still present for an advanced risk assessment of power transformers under the influence of GIC.

Table 4: Abstract of GIC-caused hotspot temperatures according to NERC [22]

Upper Bound of Peak Metallic Hotspot Temperatures Calculated Using the Benchmark GMD Event			
Effective GIC (A/phase)	**Metallic hotspot Temperature (°C)**	**Effective GIC (A/phase)**	**Metallic hotspot Temperature (°C)**
0	80	100	182
10	107	110	186
20	128	120	190
30	139	130	193
40	148	140	204
50	157	150	213
60	169	160	221
70	170	170	230
75	172	180	234
80	175	190	241
90	179	200	247

2.6 Summary

The history shows that solar events can influence the operation of power grids on earth. The reasons are Geomagnetically Induced Currents (GIC) within the transmission system, whereas higher-latitude countries are primarily affected by this phenomenon. The most critical effects due to GIC are additional harmonics in the power system and rising temperatures in the affected machines. These effects must be quantified to evaluate potential risks for the grid and the installed transformers. Literature of existing methods indicate missing design-specific calculation models, which are proved by measurements, for an adequate simulation. The influence of the thermal condition of a transformer is also not suitable covered by existing methods. Consequently an improved risk assessment model should be developed by this thesis. This means design-specific calculation models which can be used to simulate the impacts of GIC on different types of power transformers in the grid should be the outcome of this work.

3 Solution Strategy

3.1 Overview

Figure 10 demonstrates the strategy to develop a risk assessment model for GIC effects in power transformers. This means the figure gives an overview of all work packages which are required to reach the discussed design-specific approach of Figure 1 in this thesis.

The first step are several studies with different transformer designs to compare the differences in the harmonic behavior and to analyze the heating of steel parts in the transformers. By the help of these studies the essential influence parameters to quantify the effects due to GIC are identified and calculation models are developed to simulate the influence of GIC magnitudes. As a result measures to improve the GIC withstand capability of transformers are also discussed. In parallel to the model development, special measurements in a high-voltage test laboratory are carried out to ensure the validity of the simulations and of the developed calculation models.

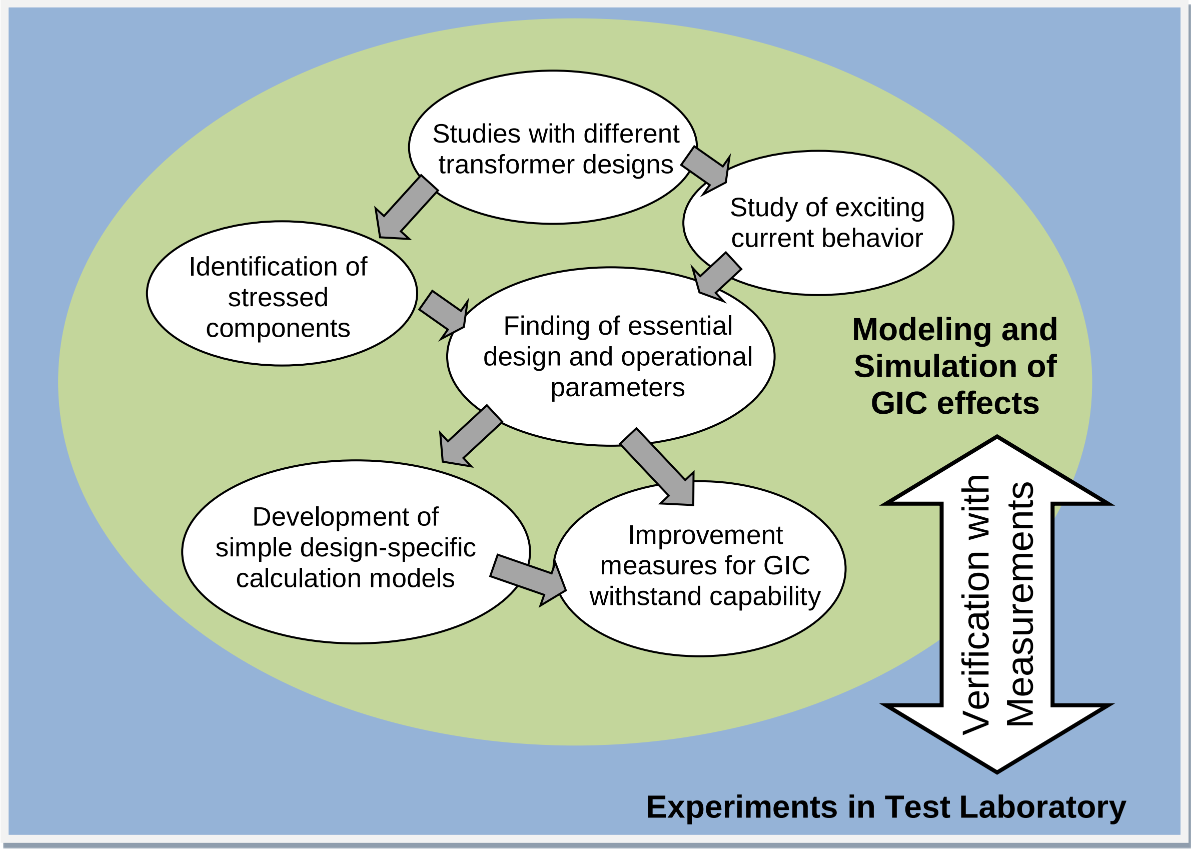
Studies with different transformer designs
Study of exciting current behavior
Identification of stressed components
Finding of essential design and operational parameters
Development of simple design-specific calculation models
Improvement measures for GIC withstand capability
Modeling and Simulation of GIC effects
Verification with Measurements
Experiments in Test Laboratory

Figure 10: Strategy to develop a design-specific risk assessment model for GIC effects

3.2 Classification of power transformers

3.2.1 General

Due to the big variety of installed transformers in power grids, the focus is on Core-Type power transformers. Common are five different core types. Here they are named T1, T2, T3, T4 and T5. Single-phase units are using the core types T1, T2 and T4 whereas three-phase transformers are built with the core types T3 and T5.

As indicated in [1] a GIC sensitivity is only possible with a grounded winding. Consequently only for such devices is a risk assessment useful. However, it is also known that the type of the magnetic core impacts significantly the GIC sensitivity of transformers as discussed in [1] and [10]. Based on these findings the sensitivities of the five different core-type power transformers are classified in Figure 11. Four cores have a high vulnerability to GIC, whereas one core design has only a low GIC vulnerability. The design of each core-type and the reason for the GIC sensitivity classification are explained in the following chapters 3.2.2 to 3.2.6.

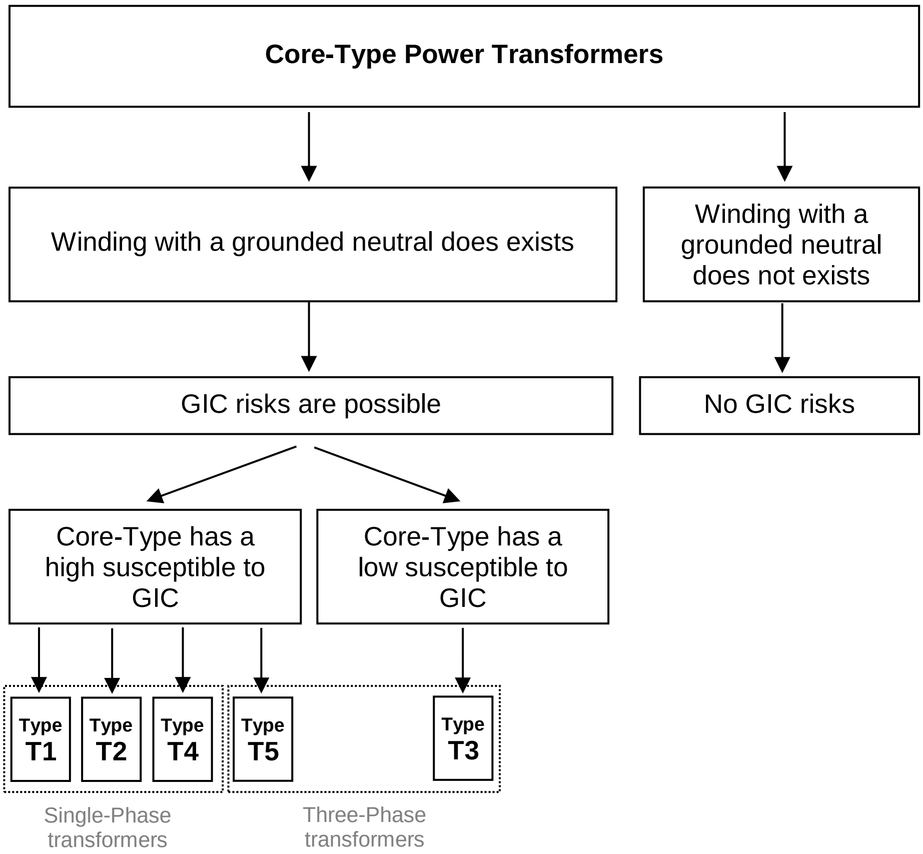
Core-Type Power Transformers
Winding with a grounded neutral does exists
Winding with a grounded neutral does not exists
GIC risks are possible
No GIC risks
Core-Type has a high susceptible to GIC
Core-Type has a low susceptible to GIC
Type T1
Type T2
Type T4
Type T5
Type T3
Single-Phase transformers
Three-Phase transformers

Figure 11: Classification of power transformers in respect to their GIC sensitivity

3.2.2 Core-Type T1

Core-Type T1 represents a widespread used design for single-phase power transformers. The core consists of one main limb to assemble the windings and two return limbs to carry the magnetic flux. The connection between main and return limb is named yoke. Figure 12 illustrates a sketch of this core arrangement. The GIC sensitivity of this core form is high, because a DC flux caused by a DC current in the winding has only a low reluctance return path due the high permeability of the return limbs. The DC flux path is indicated with green arrows in the graphic.

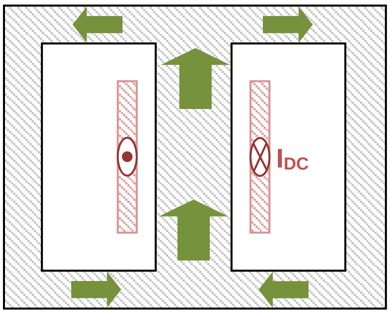

Figure 12: Sketch of Core-Type T1 (longitudinal section view)

3.2.3 Core-Type T2

If two equivalent low-voltage systems are needed in a power transformer, Core-Type T2 is often used for single-phase transformers. The high-voltage winding in such transformers is normally divided into two parallel connected windings wounded on both limbs with opposing directions as shown in Figure 13. Therefore a DC current in the high-voltage winding causes a DC flux which circle within the core. Consequently also this core has a high GIC sensitivity due to the low reluctance path for the DC flux.

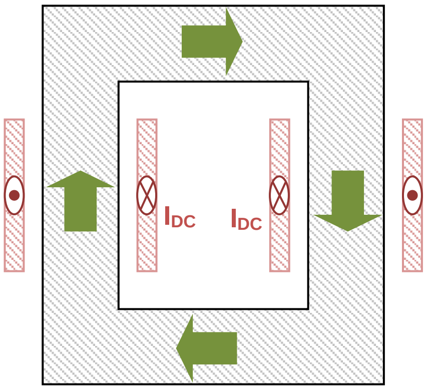

Figure 13: Sketch of Core-Type T2 (longitudinal section view)

3.2.4 Core-Type T3

Figure 14 illustrates a sketch of Core-Type T3 what is used for three-phase power transformers. The GIC sensitivity of such a design is lower than the sensitivities of Core-Type T1 or Core-Type T2. As mentioned above, the DC flux in the single-phase designs has a low reluctance path due the high permeability of the return paths. In a T3 core the generated DC flux must return via the air and the transformer tank, because each limb generates the same DC flux magnitude into the same direction. Therefore the DC flux of a T3 Core-Type has a high reluctance return path.

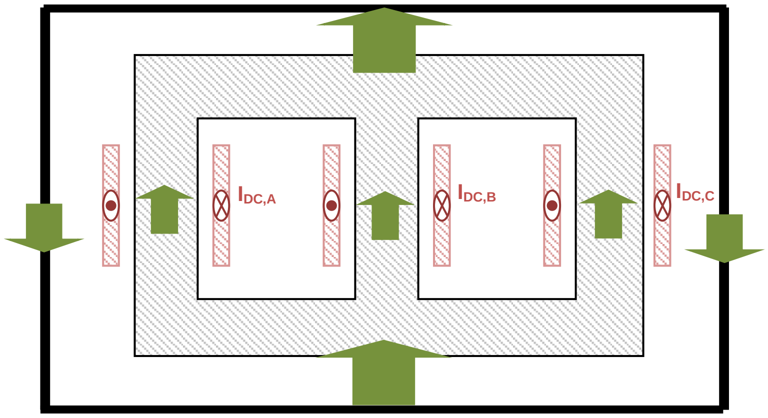

Figure 14: Sketch of Core-Type T3 (longitudinal section view)

3.2.5 Core-Type T4

In many transformer specifications is the maximal permissible tank height specified. As a result, single-phase units cannot be realized with a T2 core when a certain nominal power is exceeded. The reason is that the yoke height of a T2 core has the same dimension as the core diameter itself. This leads to a large total height of the core. In order to reach a lower height, Core-Type T4 can be used, because with this core design the height of yoke can be reduced.

Core-Type T4 is built with two return limbs in combination with the main limbs as shown in Figure 15. The manufacturing of this core design is more complex than of a T2 core, but issues regarding the total transformer height can be solved. In respect of the GIC sensitivity there exists no significant difference compared with a T2 core. A low reluctance return path for the DC flux exists due to the return limbs. Consequently, the GIC sensitivity is high.

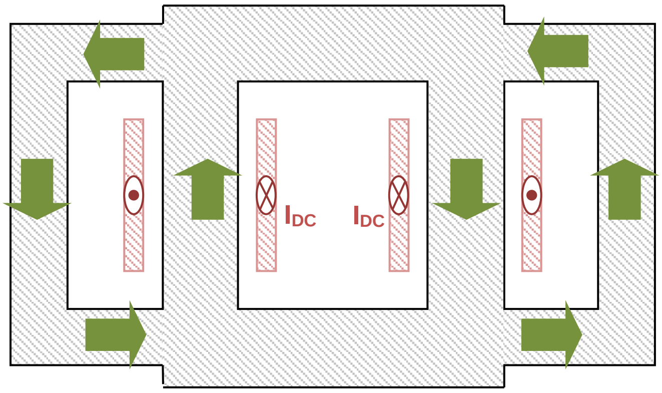

Figure 15: Sketch of Core-Type T4 (longitudinal section view)

3.2.6 Core-Type T5

For three-phase transformers is Core-Type T5 an alternative to a T3 core design. The advantages and disadvantages are similar as discussed with the differences between a T2 and a T4 core for single-phase transformers. Also here is the major criterion for the selection of a T3 or a T5 core the maximal specified tank height. Nevertheless, three-phase transformers with these core designs have a further significant difference. The main zero inductance of three-phase transformers with a T5 core is much higher than at three-phase transformers with a T3 core [39]. This circumstance can be also a selection criterion for the core design.

The difference between a T3 and a T5 core are the two return limbs beside the outer main limbs. This influence significantly the GIC sensitivity, because in a T5 core the DC flux can return via the returns limbs as shown in Figure 16. This is not possible in a T3 core where the DC flux must return via the air and the transformer tank. Therefore, three-phase transformers with such a core design have a much higher GIC sensitivity than three-phase transformers with a T3 core. In addition a coupling between the phases will occur and both return limbs will carry about 1.5 times more DC flux than the three main limbs.

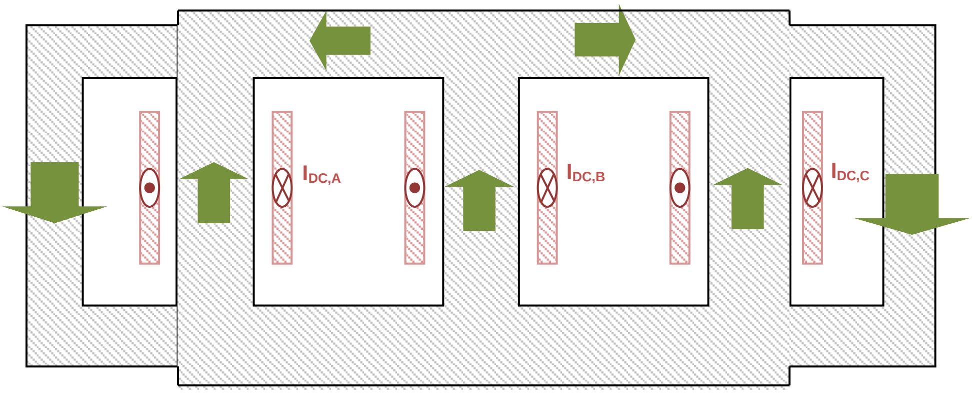

Figure 16: Sketch of Core-Type T5 (longitudinal section view)

3.3 Development of a risk assessment model for transformers

3.3.1 Calculation of the harmonic behavior

As shown before, harmonic and hotspot calculations are needed for a suitable GIC risk assessment. To study the harmonic content of the exciting current, its wave form by a certain DC excitation must be known. As mentioned in chapter 3.2, the core design influences significantly the magnetic reluctance path of the DC flux and in further consequence also the exciting current [10]. In addition the winding arrangement has also an effect on the transformer behavior under DC. Therefore, the essential design parameters of the core, the winding and the tank arrangement must be identified and considered in the simulation. The idea is an easy applicable calculation model to simulate the wave form of the exciting current for a given GIC magnitude in a winding of a power transformer.

Figure 17 below demonstrates the procedure to develop such a simplified harmonic calculation. The left part of the figure illustrates a sketch of a transformer with a T3 core design together with the winding and the tank. The right-hand side shows a corresponding network model of this transformer with lumped elements. In such a lumped model the detailed geometry is concentrated to several magnetic resistances. The work of this thesis is the development of such lumped element models. This includes the establishment of appropriate magnetic network structures for different core types and the parameterization of the magnetic resistances in these networks by the help of essential geometry parameters in order to find a design-based calculation.

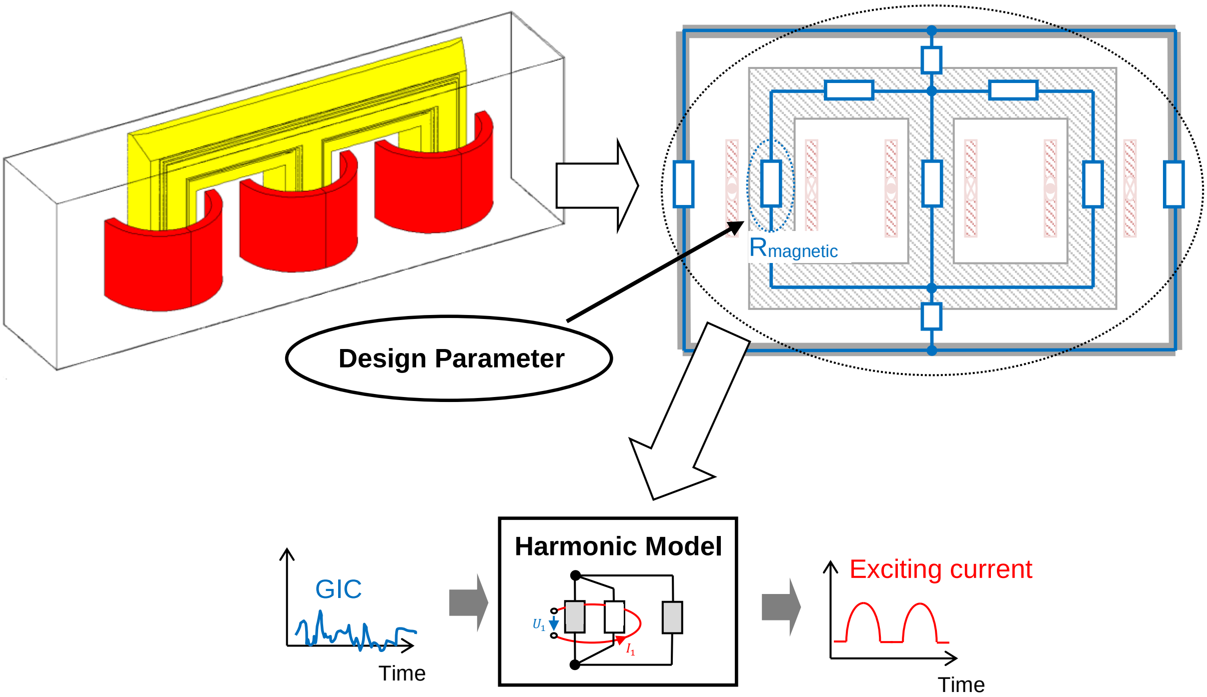

Figure 17: Development procedure of a model to calculate harmonics (illustrated by the help of a T3 core transformer)

3.3.2 Calculation of the hotspot behavior

The second part in the assessment of GIC risks is an adequate simulation of the hotspot temperature rise due to the additional DC current. For that reason the most thermal-stressed components in power transformers must be identified and a simplified hotspot temperature model derived. Figure 18 demonstrates the structure of the planned hotspot calculation.

The first step to find a hotspot model is the loss calculation in those components which are affected by GIC, because the losses are a fundamental input for the thermal calculation. The plan is to find out a loss calculation method which is based on the harmonic model together with some design parameter of the strained components. Afterwards a transient thermal model can be developed to simulate the temperature behavior for GIC profiles. This thermal model should also consider design-specific parameter together with the actual thermal condition in the transformer tank. For this reason meaningful input parameters to consider the thermal condition in the tank must be found.

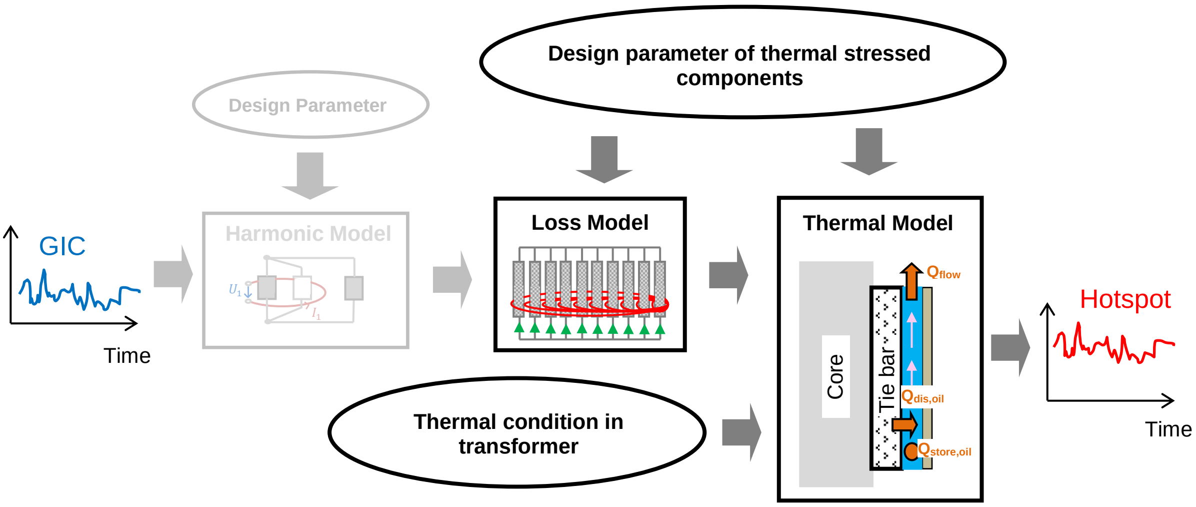
Design parameter of thermal stressed components
Design Parameter
GIC
Time
Harmonic Model
Loss Model
Thermal Model
Thermal condition in transformer
Core
Tie bar
Q_{flow}
$Q_{dis,oil}$
$Q_{store,oil}$
Hotspot
Time

Figure 18: Approach for a simplified hotspot calculation model

3.4 *Model verification*

In order to verify the developed calculation models and the simulations, several measurements in a high-voltage laboratory are carried out. For this reason special test circuits are developed to measure the GIC effects in different power transformers. A DC source is used to inject different DC currents into the windings and AC/DC transducer measure the wave form of the exciting current under DC excitation. To measure also the heating and the behavior of the magnetic flux during the DC experiments, temperature sensors and flux measuring loops are installed during the manufacturing process of the tested transformers. In that way a comparison between the results of the developed calculation models and the corresponding measurements is possible.

4 Harmonic Calculation

4.1 Basics

4.1.1 Example

It is known that electro-magnetic models are suitable to simulate the exciting current of power transformers as discussed in [30] or [40]. Figure 19 shows the basic principle of this modeling technique. The graphic demonstrates an electrical circuit of a single winding which is coupled to a simple magnetic system. This electro-magnetic arrangement can be modeled as a network of flux branches with magnetic resistances where the electrical winding is linked with some of the magnetic fluxes. In that way the flux distribution and the flux linkage of the winding is determined.

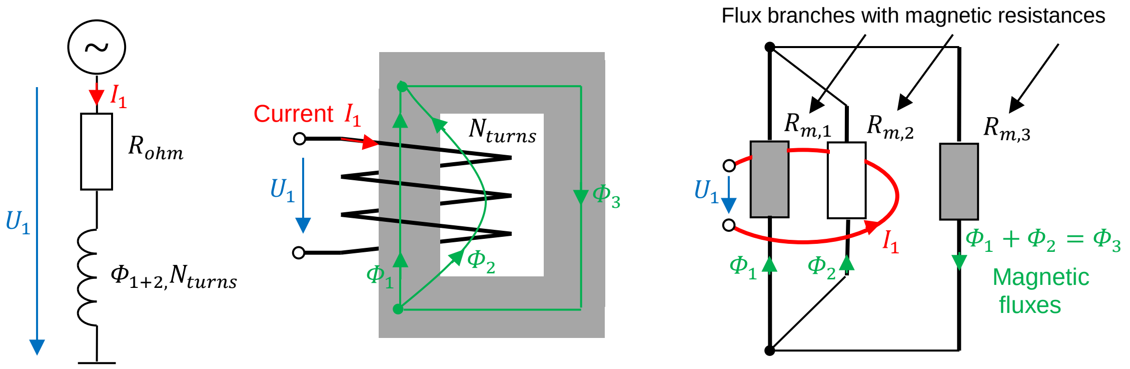

Figure 19: Electro-Magnetic Modeling (Left: Electrical circuit of a winding, Center: Linkage to magnetic system, Right: Electro-magnetic model)

The magneto-motive force Θ_b of each flux branch is given with the product of the magnetic resistance R_m and the magnetic flux Φ_b.

$$\Theta_b = R_m \cdot \Phi_b \tag{1}$$

The connection of branches leads to different magnetic loops which can be described with a structural matrix **T**. This is a [l x p] matrix where l is the number of loops and p the number of branches in the electro-magnetic model. For the basic example of Figure 19 the matrix **T** is given with:

$$\mathbf{T} = \begin{bmatrix} 1 & -1 & 0 \\ 0 & 1 & -1 \end{bmatrix} \tag{2}$$

The magnetic fluxes of the branches can be expressed with the transposed structural matrix and the magnetic fluxes of the loops:

$$\boldsymbol{\Phi_b} = \mathbf{T}^T \cdot \boldsymbol{\Phi_l} \tag{3}$$

$\boldsymbol{\Phi_b}$ is a [p x 1] vector containing the fluxes in each branch and $\boldsymbol{\Phi_l}$ is a [l x 1] vector with the fluxes of each loop. Consequently the magneto-motive forces of the loops $\boldsymbol{\Theta_l}$ can be calculated with the following matrix equation

$$\boldsymbol{\Theta_l} = \mathbf{T} \cdot \mathbf{R_m} \cdot \mathbf{T}^T \cdot \boldsymbol{\Phi_l} \tag{4}$$

where **R**$_\mathbf{m}$ is a diagonal matrix which contains the magnetic resistances. Based on the Ampère's circuital law each loop must fulfill following equation:

$$\boldsymbol{\Theta_l} = \mathbf{D} \cdot \boldsymbol{I} \tag{5}$$

The matrix **D** describes for each winding the linkage with one or several magnetic loops. It is a [l x w] matrix, where w is the number of the windings in the electro-magnetic model. $\boldsymbol{I}$ is a [w x 1] vector with the currents of the windings.

In addition Faraday's law of induction must be fulfilled for each winding and that means that the voltage $\boldsymbol{U}$ of each winding is given:

$$\boldsymbol{U} = \mathbf{D}\cdot\frac{d\boldsymbol{\Phi}_{\boldsymbol{l}}}{dt} + \boldsymbol{I}\cdot\boldsymbol{R}_{\boldsymbol{ohm}} \tag{6}$$

In this formula **R** $\mathbf{R}_{\mathbf{ohm}}$ is a diagonal matrix with the ohmic resistances of the windings, and **U** is a [w x 1] vector with the applied voltages at the winding terminals. If the applied voltage is known, then the electro-magnetic model of the basic example (Figure 19) has three state variables which differ at each time step over a time period as demonstrated in Figure 20. These state variables are the fluxes in the magnetic loops and the currents in the electrical windings. Consequently the basic example has $3\cdot n$ unknown variables in a time period, where n represents the number of time steps over a complete period.

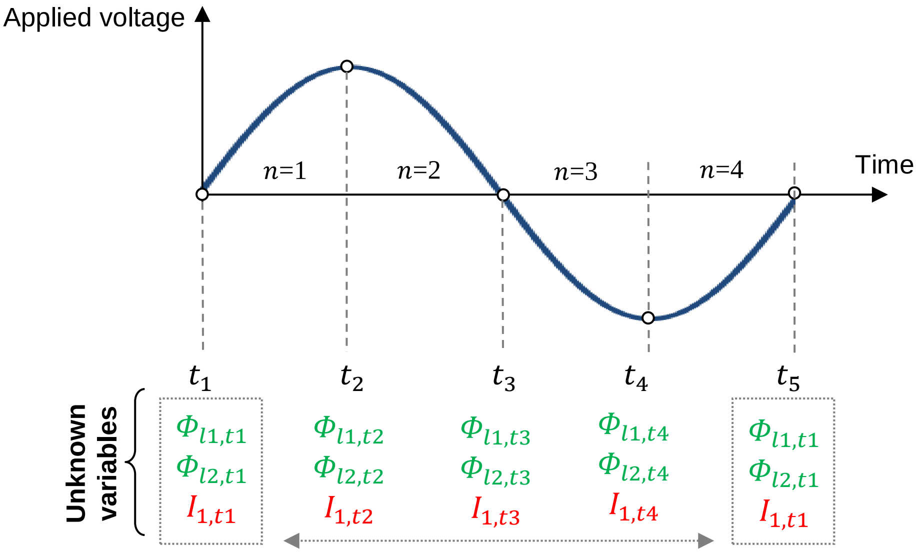

Figure 20: Unknown variables over a total time period

The equations (5) and (6), which characterize the electro-magnetic model of Figure 19, can be summarized with a matrix equation for all time steps of a time period as it is shown in Figure 21.

Matrix $\mathbf{T}\cdot\mathbf{R_m}\cdot\mathbf{T}^{\mathrm{T}}$

Matrix D

$$\begin{bmatrix}
R_{m,1}+R_{m,2} & -R_{m,2} & 0 & \cdot & \cdot & \cdot & \cdot & \cdot & \cdot & \cdot & \cdot & \cdot \\
-R_{m,2} & R_{m,1}+R_{m,2} & N_{turns} & \cdot & \cdot & \cdot & \cdot & \cdot & \cdot & \cdot & \cdot & \cdot \\
\cdot & \cdot & \cdot & R_1+R_2 & -R_2 & 0 & \cdot & \cdot & \cdot & \cdot & \cdot & \cdot \\
\cdot & \cdot & \cdot & -R_2 & R_1+R_2 & N_{turns} & \cdot & \cdot & \cdot & \cdot & \cdot & \cdot \\
\cdot & \cdot & \cdot & \cdot & \cdot & \cdot & R_1+R_2 & -R_2 & 0 & \cdot & \cdot & \cdot \\
\cdot & \cdot & \cdot & \cdot & \cdot & \cdot & -R_2 & R_1+R_2 & N_{turns} & \cdot & \cdot & \cdot \\
\cdot & \cdot & \cdot & \cdot & \cdot & \cdot & \cdot & \cdot & \cdot & R_1+R_2 & -R_2 & 0 \\
\cdot & \cdot & \cdot & \cdot & \cdot & \cdot & \cdot & \cdot & \cdot & -R_2 & R_1+R_2 & N_{turns} \\
0 & -\frac{N_{turns}}{dt} & R_{ohm} & 0 & +\frac{N_{turns}}{dt} & \cdot & \cdot & \cdot & \cdot & \cdot & \cdot & \cdot \\
\cdot & \cdot & \cdot & 0 & -\frac{N_{turns}}{dt} & R_{ohm} & 0 & +\frac{N_{turns}}{dt} & \cdot & \cdot & \cdot & \cdot \\
\cdot & \cdot & \cdot & \cdot & \cdot & \cdot & 0 & -\frac{N_{turns}}{dt} & R_{ohm} & 0 & +\frac{N_{turns}}{dt} & \cdot \\
0 & +\frac{N_{turns}}{dt} & \cdot & \cdot & \cdot & \cdot & \cdot & \cdot & \cdot & 0 & -\frac{N_{turns}}{dt} & R_{ohm}
\end{bmatrix}
\cdot
\begin{bmatrix}
\Phi_{l1,t1} \\ \Phi_{l2,t1} \\ I_{1,t1} \\ \Phi_{l1,t2} \\ \Phi_{l2,t2} \\ I_{1,t2} \\ \Phi_{l1,t3} \\ \Phi_{l2,t3} \\ I_{1,t3} \\ \Phi_{l1,t4} \\ \Phi_{l2,t4} \\ I_{1,t4}
\end{bmatrix}
=
\begin{bmatrix}
0 \\ 0 \\ 0 \\ 0 \\ 0 \\ 0 \\ 0 \\ 0 \\ U_{1,t1} \\ U_{1,t2} \\ U_{1,t3} \\ U_{1,t4}
\end{bmatrix}$$

Figure 21: Matrix equation of an electro-magnetic model

4.1.2 Solving of the equation system

To solve such an equation system the values of the magnetic resistances must be known. In general a magnetic resistance is characterized with

$$R_m = \frac{l_m}{\mu_0 \cdot \mu_r \cdot A_m} \tag{7}$$

where A_m is the cross section of the material, l_m the magnetic length, μ_0 the magnetic field constant and μ_r the relative permeability which is a parameter for the magnetic conductivity of the material. This leads to two types of magnetic resistances. The first group of resistances is constant over the time due to a fixed value of μ_r. For air, μ_r, is equal to one ($\mu_r=1$). Consequently, the constant magnetic resistances are only determined by geometry.

$$R_{m,const} = \frac{l_m}{\mu_0 \cdot A_m} \tag{8}$$

The second group of resistances changes over the time, because the magnetic resistance is a function of the relative permeability. To determine the relative permeability the B-H curve of the material must be used. This curve describes the non-linear relationship between the magnetic flux and the magnetic field strength in the material (Figure 22). It is known that a magnetic hysteresis occurs when a magnetic flied is applied to a magnetic material. However, the width of such a hysteresis is very small for materials which are used for transformer cores. Hence the initial magnetization curve of the material can be used for the calculation. Anyhow, the values for the variable resistances must be calculated at each time step depending on the corresponding flux density at this moment as shown in equation (9).

$$R_m(t) = f(\mu_r(t)) = R_{const} \cdot \frac{1}{\mu_r(t)} \qquad \mu_r(t) = \frac{B(t)}{\mu_0 \cdot H(t)} = \frac{\Phi(t)}{\mu_0 \cdot A_m \cdot H(t)} \tag{9}$$

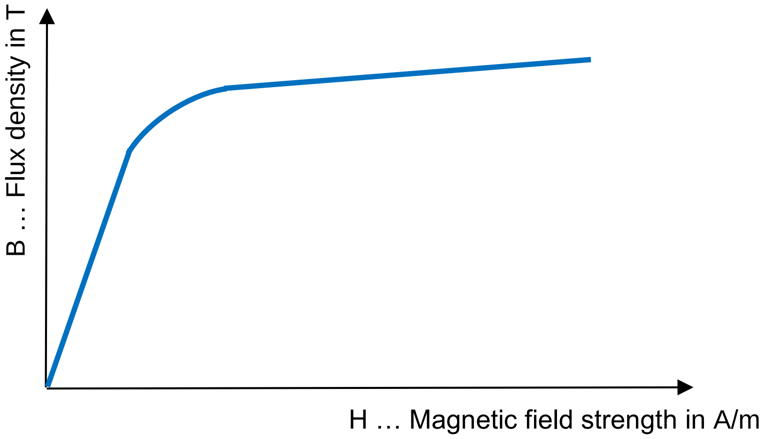

Figure 22: Nonlinear B-H curve of magnetic material

The non-linearity of the B-H curve leads to a non-linear equation system. This means, if the magnetic resistance $R_{m,1}$ in the basic example of Figure 19 is variable, then the value of $R_{m,1}$ is at each time step a function of Φ_{b1} at this moment.

$$R_{m,1,ti} = f\left(\Phi_{b1,ti}\right) \quad Time\ step\ i = 1 \dots 4 \tag{10}$$

Such a non-linear equation system is shown in Figure 23 below. The non-linearity can be seen because some resistances in the matrix are a function of the unknown magnetic flux.

The following chapters show how to build such non-linear equation systems for different transformer designs in order to simulate their exciting current.

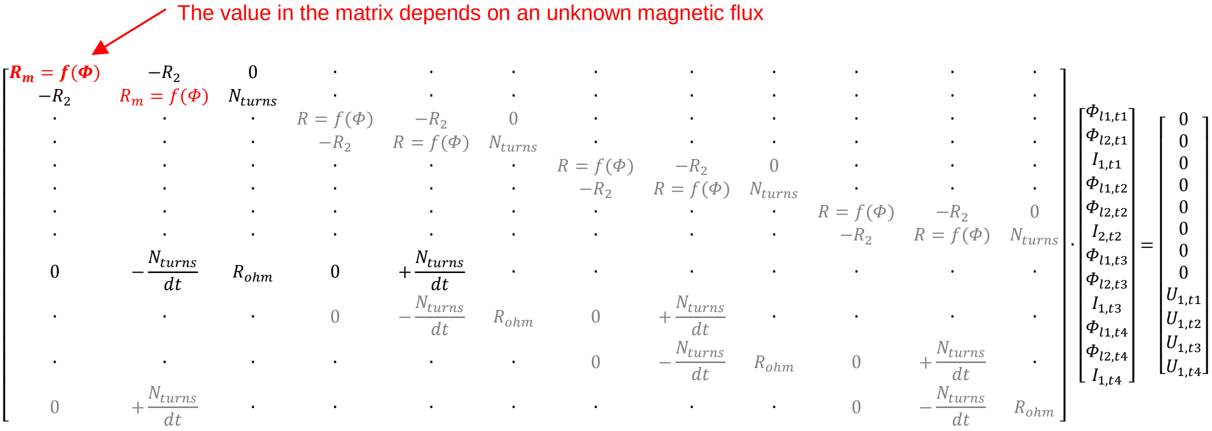

Figure 23: Non-linear matrix equation of an electro-magnetic model

4.2 *Single-Phase Transformers*

4.2.1 Model for core designs with one wounded limb

4.2.1.1 Electro-magnetic network for Core-Type T1

Figure 24 demonstrates the electrical circuit to calculate the exciting current of single-phase transformers which use a core design with one wounded limb (Core-Type T1). It is assumed, that the AC and DC voltage is applied at the same winding of the transformer. Consequently, the voltage at this winding terminal is given with:

$$U_1 + U_{DC} = N_{turns} \cdot \frac{d(\Phi_{L11} + \Phi_1)}{dt} + I_1 \cdot R_{ohm} \tag{11}$$

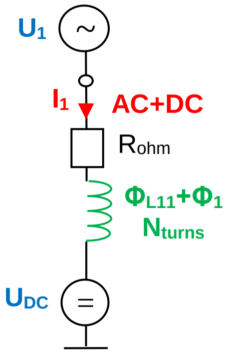

Figure 24: Electric circuit for single-phase transformers (one-wounded limb)

In order to calculate the winding current I_1 and the magnetic flux components Φ_{L11} and Φ_1 in equation (11), the electro-magnetic network of Figure 25 can be used. Each magnetic resistance (e.g. R_{L11}, R_1, etc.) represents a different area in the transformer. In that way the individual design is considered in the calculation. Figure 26 illustrates in a simplified way which magnetic resistances are modeling which parts of a transformer with a T1 Core-Type. In the left part of Figure 26 the magnetic resistances for the core parts are shown (shaded resistances) together with the resistances which represent the gap between core limb and excited winding and the resistance which models the gap outside of the winding within the transformer tank. The segmentation into three axial parts is required to cover a potential inhomogeneous flux distribution over the height in the core limb. The right part of the figure shows the magnetic resistances which model the gap between the upper end of the core up to the tank wall together with the resistances for the tank wall, the adjacent outer air and for a potential axial shielding.

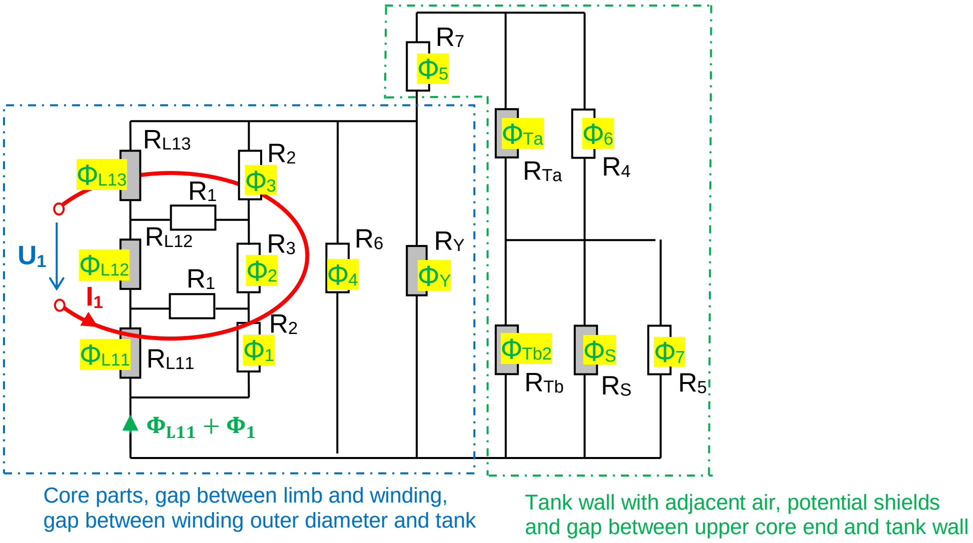
R7
Φ5
RL13
ΦL13
R2
Φ3
R1
RL12
ΦL12
R3
Φ2
R1
U1
I1
R2
ΦL11
RL11
Φ1
R6
Φ4
RY
ΦY
ΦL11 + Φ1
ΦTa
RTa
Φ6
R4
ΦTb2
RTb
ΦS
RS
Φ7
R5
Core parts, gap between limb and winding,
gap between winding outer diameter and tank
Tank wall with adjacent air, potential shields
and gap between upper core end and tank wall

Figure 25: Electro-magnetic network for transformers with a T1 Core-Type

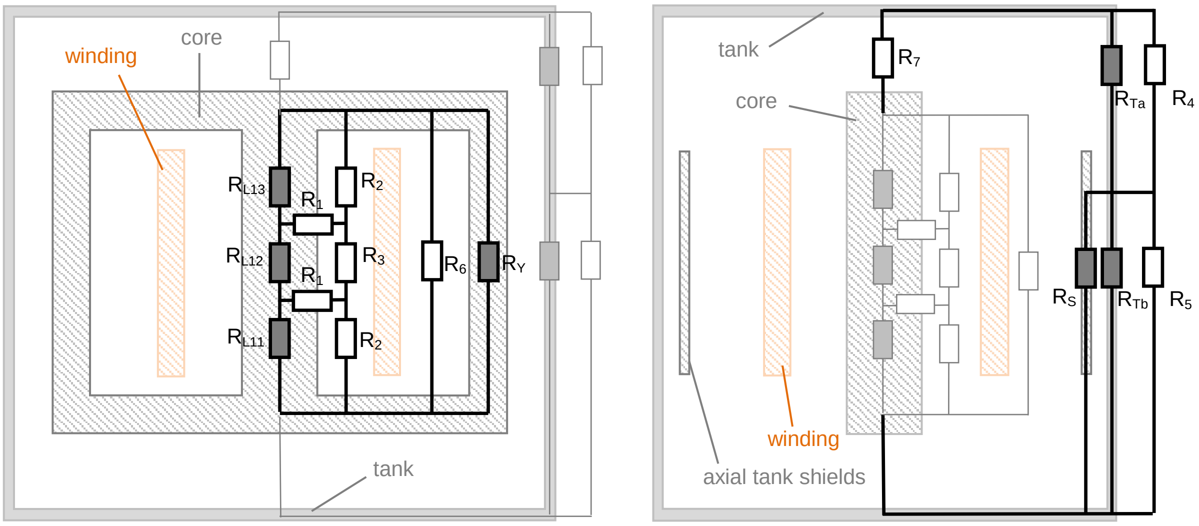
winding
core
RL13
R1
R2
RL12
R1
R3
R6
RY
RL11
R2
tank
tank
R7
core
RTa
R4
RS
RTb
R5
winding
axial tank shields

Figure 26: Simplified modeling of different transformer areas with magnetic resistances

4.2.1.2 Determination of magnetic resistances

As already shown in chapter 4.1.2, magnetic resistances can be constant or variable over the time. It was also discussed that they are determined with the geometry of the corresponding area (magnetic length and cross section) and the magnetic conductivity of the area (relative permeability μ_r). The detailed calculation of the magnetic resistances, which are simplified illustrated in Figure 26 above, is given in Table 5 and Table 6. That means the tables indicate the magnetic lengths as well as the magnetic cross sections, which can be used to parametrize the magnetic resistances of the network for a transformer with a T1 Core-Type. In addition to these geometry parameters the B-H curves of the used materials must be known to calculate the changing relative permeability values of the variable magnetic resistances and to solve the non-linear equation system.

Table 5: Calculation of variable magnetic resistances in the network of a T1 Core-Type

<table>
<tr><th>Formula</th><th>Sketch</th><th>Formula</th><th>Sketch</th></tr>
<tr>
<td>$\boldsymbol{R_{L,ij}} = \frac{\mathbf{0.333} \cdot \boldsymbol{L_1}}{\boldsymbol{\mu_0} \cdot \boldsymbol{A_C}} \cdot \frac{\mathbf{1}}{\mu_r(\boldsymbol{B_{L,ij}}, \boldsymbol{H_{L,ij}})}$</td>
<td>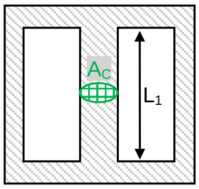
$i = 1, j = 1 \ldots 3$</td>
<td>$\boldsymbol{R_Y} = \frac{\boldsymbol{l_{rl}}}{\mathbf{2} \cdot \boldsymbol{\mu_0} \cdot \boldsymbol{A_Y}} \cdot \frac{\mathbf{1}}{\mu_r(\boldsymbol{B_Y}, \boldsymbol{H_Y})}$</td>
<td>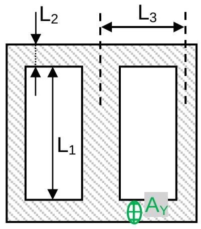
$l_{rl} = 2 \cdot L_3 + 2 \cdot L_2 + L_1$</td>
</tr>
<tr><th colspan="2">Formula</th><th colspan="2">Sketch</th></tr>
<tr>
<td colspan="2">$\mathbf{R_{Ta}} = \frac{\mathbf{L_7 - L_8}}{\boldsymbol{\mu_0} \cdot \mathbf{A_T}} \cdot \frac{\mathbf{1}}{\mu_r(\mathbf{B_{Ta}}, \mathbf{H_{Ta}})}$
$\mathbf{R_{Tb}} = \frac{\mathbf{L_7}}{\boldsymbol{\mu_0} \cdot \mathbf{A_T}} \cdot \frac{\mathbf{1}}{\mu_r(\mathbf{B_{Tb}}, \mathbf{H_{Tb}})}$
$\mathrm{A_T} = 2 \cdot \mathrm{L_5} \cdot \mathrm{d_w} + 2 \cdot \mathrm{d_w} \cdot (\mathrm{L_6} - 2 \cdot \mathrm{d_w})$</td>
<td colspan="2">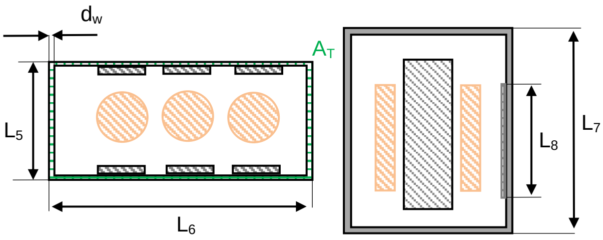 </td>
</tr>
<tr>
<td colspan="2">$\boldsymbol{R_S} = \frac{\boldsymbol{L_8}}{\boldsymbol{\mu_0} \cdot \boldsymbol{A_S}} \cdot \frac{\mathbf{1}}{\mu_r(\boldsymbol{B_S}, \boldsymbol{H_S})}$</td>
<td colspan="2">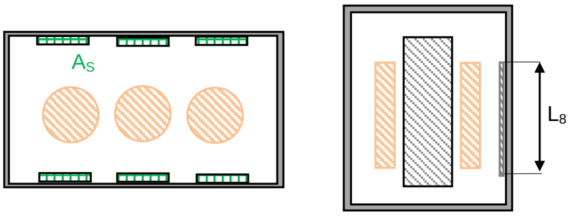 </td>
</tr>
</table>

Table 6: Calculation of constant magnetic resistances in the network of a T1 Core-Type

<table>
<tr><th>Formula</th><th>Sketch</th><th>Formula</th><th>Sketch</th></tr>
<tr>
<td>$\boldsymbol{R_1} = \frac{\mathbf{0.5} \cdot (\boldsymbol{D_I} - \boldsymbol{D_C})}{\boldsymbol{\mu_0} \cdot \boldsymbol{A_2}}$
$A_1 = \frac{\left(\frac{D_I + D_O}{2} + D_C\right)}{2} \cdot \pi \cdot \frac{L_1}{2}$</td>
<td>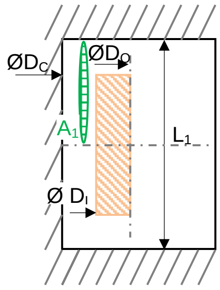 </td>
<td>$\boldsymbol{R_2} = \frac{\mathbf{0.333} \cdot \boldsymbol{L_1}}{\boldsymbol{\mu_0} \cdot \boldsymbol{A_2}}$
$A_2 = \frac{(f_1{}^2 - D_C{}^2) \cdot \pi}{4}$
$f_1 = f(D_I, D_O)$</td>
<td>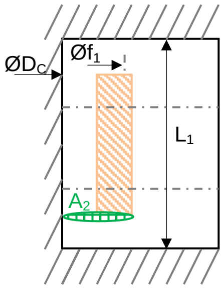 </td>
</tr>
<tr>
<td>$\boldsymbol{R_3} = \frac{\mathbf{0.333} \cdot \boldsymbol{L_1}}{\boldsymbol{\mu_0} \cdot \boldsymbol{A_3}}$
$A_3 = \frac{(f_2{}^2 - D_C{}^2) \cdot \pi}{4}$
$f_2 = f(D_I, D_O)$</td>
<td>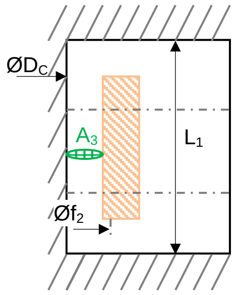 </td>
<td>$\boldsymbol{R_6} = \frac{\boldsymbol{L_1}}{\boldsymbol{\mu_0} \cdot \boldsymbol{A_6}}$
$A_6 = L_5 \cdot L_6 - \frac{D_O{}^2 \cdot \pi}{4}$</td>
<td>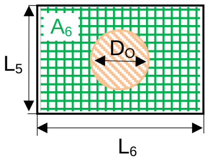 </td>
</tr>
</table>

Formula	Sketch
$\boldsymbol{R_4} = \frac{\boldsymbol{L_7 - L_8}}{\boldsymbol{\mu_0 \cdot A_{\mathrm{out}}}}$ $\boldsymbol{R_5} = \frac{\boldsymbol{L_8}}{\boldsymbol{\mu_0 \cdot A_{\mathrm{out}}}}$ $A_{out} = 2 \cdot (L_5 + 2 \cdot f_3) \cdot f_3 + 2 \cdot L_6 \cdot f_3$	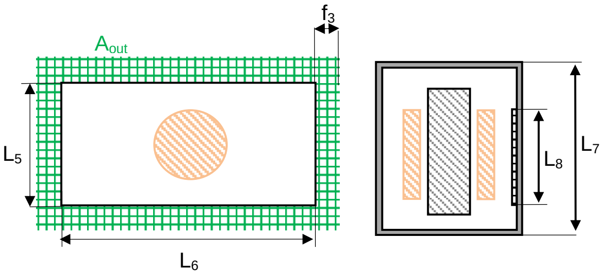 A_{out} f_3 L_5 L_6 L_8 L_7
$\boldsymbol{R_7} = \frac{\boldsymbol{1}}{\sum_{i=1}^{n+2} \frac{\boldsymbol{1}}{\boldsymbol{R_{a,i}}}}$ $d_1 = 0.5 \cdot (L_5 - L_{10})$ $d_2 = 0.5 \cdot \sqrt{\left(\frac{L_{10}}{2} - L_9\right)^2 + \left(L_2 - \frac{L_{11}}{2}\right)^2}$ $\alpha = acos\left(\frac{0.5 \cdot L_{10} - L_9}{2 \cdot d_2}\right)$ $d_3 = d_1 + 2 \cdot d_2 \cdot cos(\alpha)$ $d_4 = 0.5 \cdot (L_7 - L_1 - 2 \cdot L_2)$ $d_5 = d_4 + 2 \cdot d_2 \cdot sin(\alpha)$ $d_6 = L_2 + d_4 - d_5$ $l_y = 2 \cdot L_3 + L_2$ $R_{a,1} = \frac{d_4}{\mu_0 \cdot L_9 \cdot \frac{l_y}{m}}$ $R_{a,i} = \frac{l_i}{\mu_0 \cdot \left(\frac{2 \cdot d_2 + d_5 + d_3}{2 \cdot n}\right) \cdot \frac{l_y}{m}}$ $R_{a,n+2} = \frac{d_1}{\mu_0 \cdot d_6 \cdot \frac{l_y}{m}}$	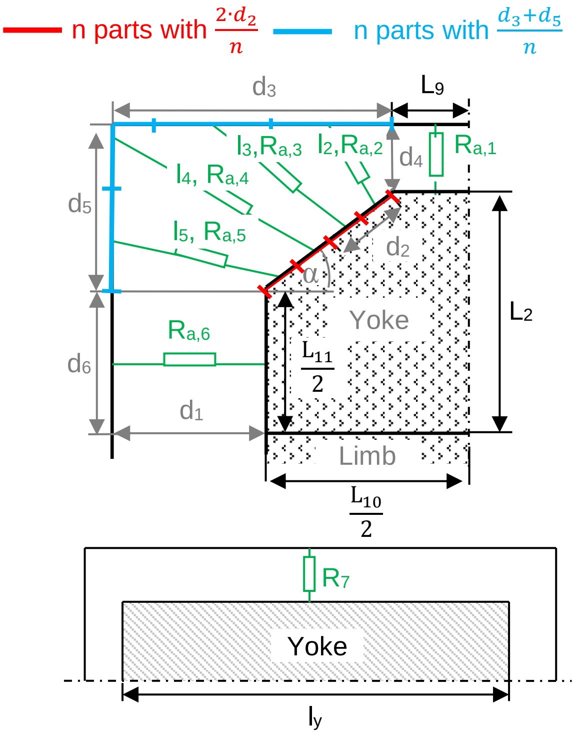 n parts with $\frac{2 \cdot d_2}{n}$ n parts with $\frac{d_3 + d_5}{n}$ d_3 L_9 $l_3, R_{a,3}$ $l_2, R_{a,2}$ d_4 $R_{a,1}$ l_4, $R_{a,4}$ d_5 l_5, $R_{a,5}$ d_2 α Yoke L_2 $R_{a,6}$ $\frac{L_{11}}{2}$ d_6 d_1 Limb $\frac{L_{10}}{2}$ R_7 Yoke l_y

4.2.2 Model for core designs with two wounded limbs

4.2.2.1 Electro-magnetic network for Core-Type T2

Figure 27 demonstrates the electrical circuit to calculate the exciting current of single-phase transformers which have a core design with two wounded limbs (Core-Type T2). It is assumed that the windings around the core limbs are in a parallel connection. Therefore, the voltage at both winding terminals is equal and given with the following equation (12).

$$U_1 + U_{DC} = N_{turns} \cdot \frac{d(\Phi_{L11} + \Phi_1)}{dt} + I_1 \cdot R_{ohm} = N_{turns} \cdot \frac{d(\Phi_{L12} + \Phi_8)}{dt} + I_2 \cdot R_{ohm} \qquad (12)$$

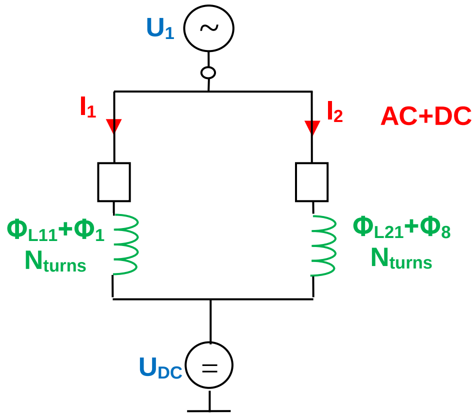
U₁
I₁
I₂
AC+DC
ΦL11+Φ1
Nturns
ΦL21+Φ8
Nturns
UDC

Figure 27: Electrical circuit for single-phase transformers (two-wounded limbs)

Similar as explained with a core with one-wounded limb, an electro-magnetic network model is required to determine the currents and the magnetic fluxes in equation (12). Figure 28 shows a suitable electro-magnetic network for transformers with a T2 Core-Type. The determination of the magnetic resistances in this network follows the same principle as discussed in chapter 4.2.1.1 before. The main difference is here the presence of two wounded limbs instead of only one winding around the main limb what lead to another electro-magnetic network. The calculation of the magnetic resistances for this network is shown in Appendix B.

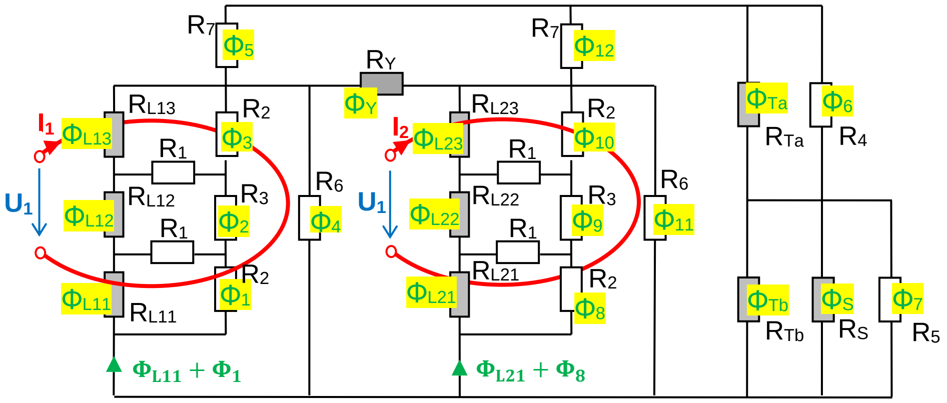
R7
Φ5
RY
ΦY
R7
Φ12
RL13
R2
I1
ΦL13
Φ3
R1
U1
RL12
ΦL12
R3
R1
Φ2
R6
Φ4
R2
ΦL11
RL11
Φ1
ΦL11 + Φ1
RL23
R2
I2
ΦL23
Φ10
R1
U1
RL22
ΦL22
R3
R1
Φ9
R6
Φ11
RL21
ΦL21
R2
Φ8
ΦL21 + Φ8
ΦTa
RTa
Φ6
R4
ΦTb
RTb
ΦS
RS
Φ7
R5

Figure 28: Electro-magnetic network for transformers with a T2 Core-Type

4.2.2.2 Electro-magnetic network for Core-Type T4

As mentioned in chapter 3.2.1 before, Core-Type T4 is a further possible core design to realize a single-phase transformer with two wounded limbs. The differences in the core form are two return limbs. This lead to a lower total transformer height compared with a T2 Core-Type (Figure 15, chapter 3.2.5).

Figure 29 shows a suitable electro-magnetic network for a transformer with a T4 Core-Type where the two return limbs are considered with the magnetic resistances R_{RL1} and R_{RL2}. The remaining connections in the network are identical with the setup for a T2 core.

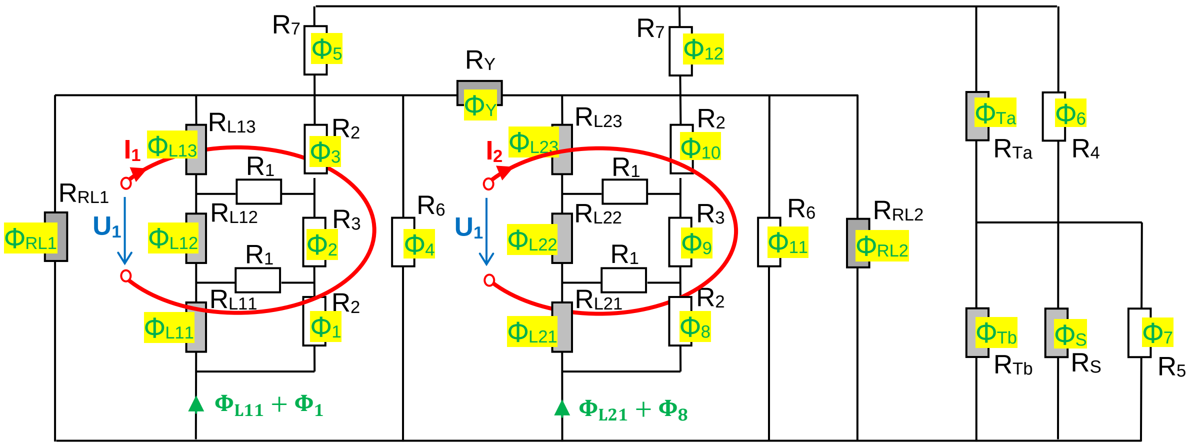
R_7
Φ_5
R_Y
Φ_Y
R_7
Φ_{12}
R_{L13}
R_2
I_1
Φ_{L13}
Φ_3
R_1
R_{RL1}
U_1
R_{L12}
R_3
Φ_{RL1}
Φ_{L12}
Φ_2
R_1
R_{L11}
R_2
Φ_{L11}
Φ_1
R_6
Φ_4
$\Phi_{L11} + \Phi_1$
I_2
Φ_{L23}
R_{L23}
R_2
Φ_{10}
R_1
U_1
R_{L22}
R_3
Φ_{L22}
Φ_9
R_1
R_{L21}
R_2
Φ_{L21}
Φ_8
$\Phi_{L21} + \Phi_8$
R_6
Φ_{11}
R_{RL2}
Φ_{RL2}
Φ_{Ta}
R_{Ta}
Φ_6
R_4
Φ_{Tb}
R_{Tb}
Φ_S
R_S
Φ_7
R_5

Figure 29: Electro-magnetic network for transformers with a T4 Core-Type

4.2.3 Analysis

In this chapter the behavior of the exciting current for three different single-phase transformers is studied with different DC levels in their high-voltage windings. Table 7 illustrates the main technical data of the transformers under investigation and Table 8 their design-specific parameters.

Table 7: Technical data of single-phase transformers under investigation

Transformer	Core-Type	Frequency	Rated voltage with nominal core flux density	Power
Unit 1	T1	60 Hz	230 /√3 kV (1.73 Tesla)	133.3 MVA
Unit 2	T2	60 Hz	433 /√3 kV (1.71 Tesla)	121.3 MVA
Unit 3	T4	60 Hz	765 /√3 kV (1.72 Tesla)	750.0 MVA

Table 8: Design-specific parameter of single-phase transformers under investigation (lengths in the table are in [m], cross sections are in [m²])

Parameter	Unit 1	Unit 2	Unit 3	Parameter	Unit 1	Unit 2	Unit 3
L_1	2.496	1.990	2.900	L_{11}	0.189	0.267	0.283
L_2	0.370	1.050	0.670	D_C	0.754	1.066	1.130
L_3	1.055	2.812	2.168	D_I	0.890	1.486	1.360
L_4	-1)	-1)	1.277	D_O	1.656	1.544	2.114
L_5	2.406	2.215	2.858	A_C	0.3965	0.811	0.808
L_6	3.067	3.955	6.014	A_Y	0.1991	0.811	0.575
L_7	3.532	4.600	4.580	A_{RL}	0.1991	-1)	0.233
L_8	-1)	-1)	-1)	A_S	-1)	-1)	-1)
L_9	0.100	0.100	0.100	d_w	0.010	0.010	0.010
L_{10}	0.716	1.013	1.074	N_{turns}	764	674	1189

---

1) This parameter not required for the selected transformer design.

As a first step the DC flux distribution in each transformer core is analyzed. For that purpose the DC fluxes which flow through the different magnetic resistances in the demonstrated electro-magnetic networks of chapter 4.2 are summarized in Table 9, Table 10 and Table 11.

Table 9: DC flux distribution [in Vs] of Unit 1 (Core-Type T1)

Branch	**5 A DC**	**10 A DC**	**20 A DC**	**30 A DC**	**50 A DC**	**100 A DC**
$\Phi_{L11}+\Phi_1$	0,112	0,131	0,158	0,180	0,217	0,290
Φ_Y	-0,108	-0,124	-0,147	-0,166	-0,196	-0,254
Φ_4	-0,002	-0,002	-0,004	-0,005	-0,007	-0,013
Φ_5	0,003	0,005	0,007	0,009	0,013	0,024

Table 10: DC flux distribution [in Vs] of Unit 2 (Core-Type T2)

Branch	**5 A DC**	**10 A DC**	**20 A DC**	**30 A DC**	**50 A DC**	**100 A DC**
$\Phi_{L11} + \Phi_1 = -(\Phi_{L21} + \Phi_8)$	0,210	0,240	0,278	0,306	0,356	0,453
Φ_Y	0,205	0,233	0,267	0,292	0,335	0,416
$\Phi_4= -\Phi_{11}$	-0,001	-0,001	-0,002	-0,002	-0,003	-0,006
$\Phi_5= -\Phi_{12}$	0,004	0,006	0,009	0,012	0,017	0,031

Table 11: DC flux distribution [in Vs] of Unit 3 (Core-Type T4)

Branch	**5 A**	**10 A**	**20 A**	**30 A**	**50 A**	**100 A**
$\Phi_{L11} + \Phi_1 = -(\Phi_{L21} + \Phi_8)$	0,214	0,245	0,286	0,324	0,377	0,489
Φ_Y	0,132	0,151	0,177	0,199	0,234	0,305
$\Phi_4= -\Phi_{11}$	-0,001	-0,002	-0,003	-0,004	-0,007	-0,012
$\Phi_5= -\Phi_{12}$	0,004	0,006	0,009	0,012	0,018	0,032
$\Phi_{RL1}= -\Phi_{RL2}$	-0,076	-0,086	-0,097	-0,106	-0,119	-0,140

The analysis confirms the assumption of chapter 3.2 in this thesis that the major part of the DC flux occurs in the transformer core. It can be also seen that identical DC levels in the transformer windings lead to different DC flux values. Obviously, this is not surprising due to the differences in the design data like the geometry and the number of turns.

The behavior of these transformers is discussed in the following. For that purpose the exciting currents and the winding flux linkages (DC+AC) of the investigated transformers are shown in Figure 30. The left side of the figure represents the condition with 30 A DC per phase in the winding and the right part shows results for 100 A DC per phase. The thicker lines in the figure represent the saturation periods of the transformer cores and the x-axes captures the normalized time of one period. It can be seen, that in parallel to the saturation periods significant peaks in the exciting currents take place. However, the wave forms of the currents are similar despite the fact, that the technical data of the single-phase transformers differs significantly. The deviation between the current peaks is only in the range of 20 %. To analyze the exciting current behavior over a wide DC range, the increase of the current fundamental and of the first five harmonics with the DC level are demonstrated in Figure 31. The figure shows, that the increase of the fundamental and of the first harmonic is similar between the transformers and that only the higher harmonics increase differently.

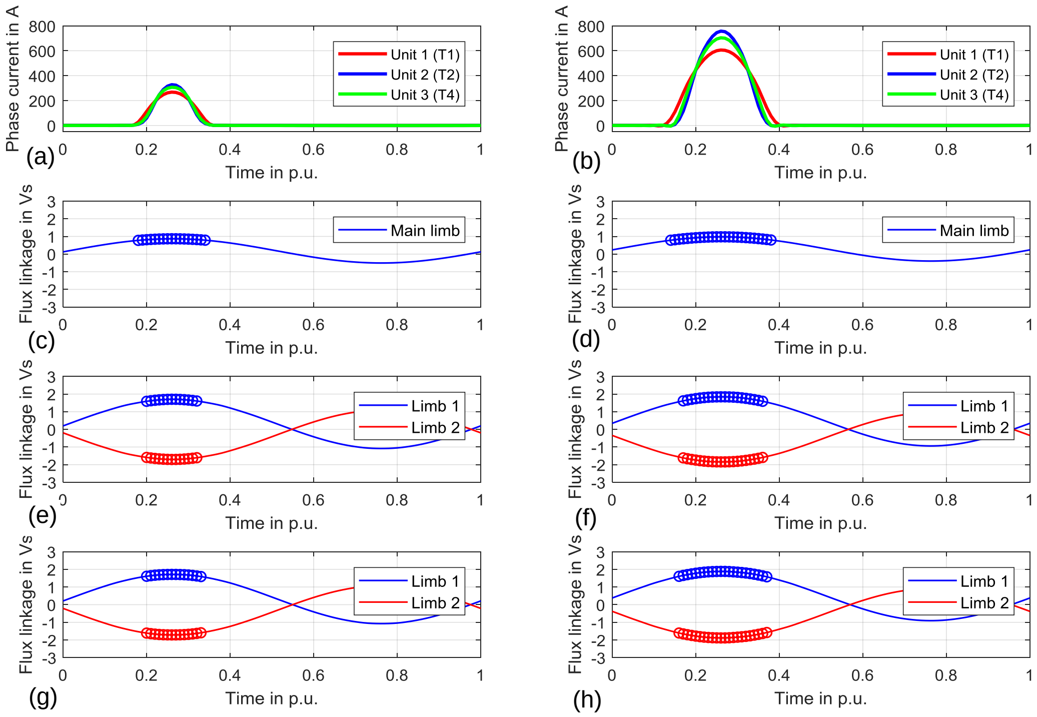

Figure 30: Core saturation of different single-phase transformers due to additional DC – Exciting current with (a) 30 A DC and (b) 100 A DC per phase, Flux linkage of a T1 Core-Type with (c) 30 A DC and (d) 100 A DC per phase, Flux linkage of a T2 Core-Type with (e) 30 A DC and (f) 100 A DC per phase, Flux linkage of a T4 Core-Type with (g) 30 A DC and (h) 100 A DC per phase

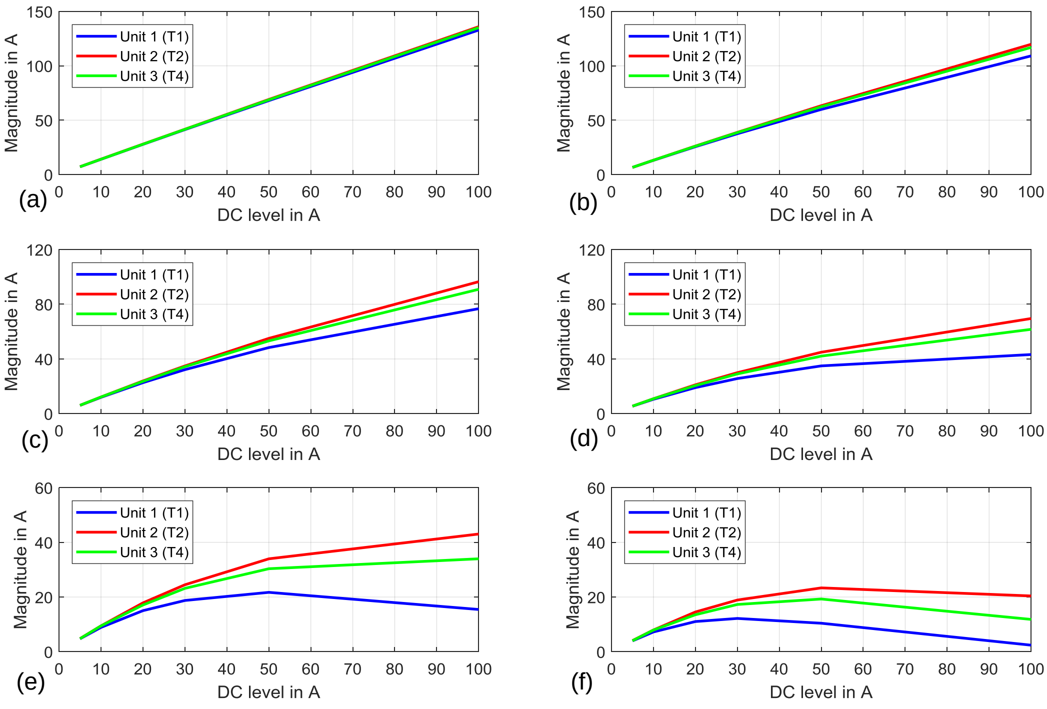

Figure 31: Harmonics of exciting current due to additional DC in single-phase transformers – RMS value of (a) Fundamental, (b) 1st harmonic, (c) 2nd harmonic, (d) 3rd harmonic, (e) 4th harmonic, (f) 5th harmonic

Figure 30 shows that the exciting currents of the transformers are linked with the saturation characteristic and that the core limbs of single-phase transformers are saturated in a section of a period when an additional DC current is present in the winding. This leads in the saturated moments to a significant reduction of the permeability of the core material. As a consequence the current value is then more or less determined by the air-core inductance of the excited winding. Consequently the behavior of the exiting current under DC can be described with a simple Ψ-I curve as shown in Figure 32. Such a curve illustrates the relationship between the exciting current $I_{ex}(t)$ and the flux linkage Ψ(t) of the current-carrying winding over the time. Below the saturation level Ψ_{sat} the exciting current is very low. For simplification purposes the current value can be assumed with zero as long as the flux linkage is lower than the saturation level. However, if the saturation limit is exceeded, then the current becomes significantly higher and the relation between the flux linkage and the exciting current is almost linear. This linear relationship can be approximated with the air-core inductance in a well manner as demonstrated in Table 12.

The table compares the increase of the exciting current above the saturation for each investigated transformer. The pure air-core inductance of the transformer windings (calculated with a 2D-FEM method) and the results of the electro-magnetic model are demonstrated in the table. In order to determine the linear increase from the network model, the difference in the flux linkage ($\Delta\Psi_{max}$) value and the peak of the exciting current are listed for two different DC levels in Table 12. It can be seen, that the ratios between $\Delta\Psi_{max}$ and I_{peak} are only slighly higher than the pure air-core inductances of the windings. Consequently the approximation of the linear increase after the saturation level with the pure air-core inductance of the excited winding is a feasible approach. That means that the current wave form of single-phase transformers can be also calculated with the knowledge of the winding's air-core inductance. A method which uses this basic relationship is discussed in chapter 4.5. The advantage of such a basic method is that no non-linear equation systems must be solved.

However, the basic knowledge about the Ψ-I curve decribes also the similarity of the current wave forms between the investigated transformers, because the DC level of each current is given with the time integral over the wave form. As demonstrated in Figure 30 the saturation time periods of the investigated transformers are very similar and as a consequence also the widths and the peaks of the currents are comparable, because otherwise the integral values would not lead to the same DC level. Therefore the maximal value of the flux linkage (Ψ_{max}) and as a consequence also the DC component of the flux (Ψ_{DC}) and the peak of exiting current (I_{peak}) depend on the air-core inductance of the excitied winding.

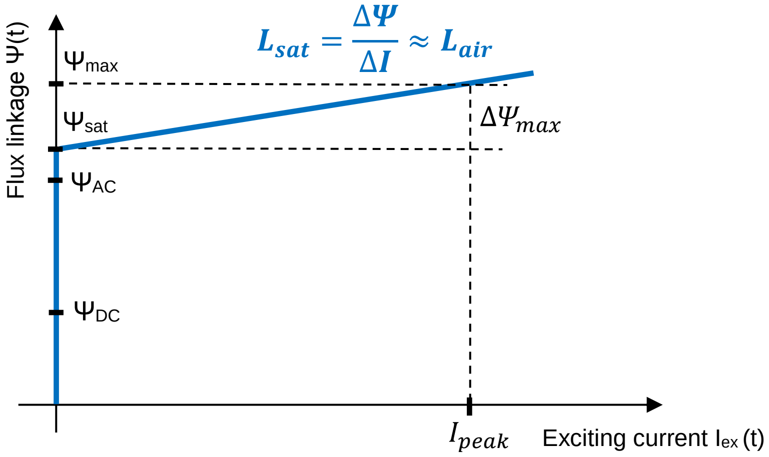

Figure 32: Simplified saturation characteristic of single-phase units (Ψ-I curve)

Table 12: Relationship between air-core inductance and the exciting current

Transformer	L_{air}	**30 A DC**			**100 A DC**		
		$\Delta\Psi_{max}$	I_{peak}	$\frac{\Delta\Psi_{max}}{I_{peak}}$	$\Delta\Psi_{max}$	I_{peak}	$\frac{\Delta\Psi_{max}}{I_{peak}}$
-	H	Vs	A	H	Vs	A	H
Unit 1	0.247	71.5	267.1	0.268	156.3	602.3	0.260
Unit 2	0.444	79.8	327.5	0.487	178.8	757.1	0.472
Unit 3	1.025	171.0	303.8	1.126	375.5	696.2	1.079

4.3 Three-Phase Transformers

4.3.1 Model for core designs with three wounded limbs

4.3.1.1 Electro-magnetic network for Core-Type T3

Figure 33 demonstrates the electrical circuit to calculate the exciting current of three-phase transformers with an additional DC current in the excited winding. The voltages at the winding terminals are given with:

$$U_1 + U_{DC} = N_{turns} \cdot \frac{d(\Phi_{L11} + \Phi_1)}{dt} + I_1 \cdot R_{ohm} \tag{13}$$

$$U_2 + U_{DC} = N_{turns} \cdot \frac{d(\Phi_{L21} + \Phi_8)}{dt} + I_2 \cdot R_{ohm} \tag{14}$$

$$U_3 + U_{DC} = N_{turns} \cdot \frac{d(\Phi_{L31} + \Phi_{13})}{dt} + I_3 \cdot R_{ohm} \tag{15}$$

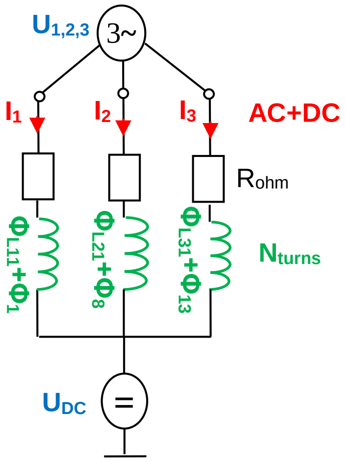

Figure 33: Electrical circuit for three-phase transformers

The currents and the flux components of this electrical circuit must be determined with an electro-magnetic model which considers the used core design of a three-phase transformer. As shown in chapter 3.2, two different core types are possible, Core-Type T3 and Core-Type T5. Figure 34 illustrates a suitable electro-magnetic network structure for a T3 Core-Type transformer. The three main limbs of this core form, their windings and the yokes are modeled with the same principle as discussed in chapter 4.2.1.1. However, as mentioned before in such a three-phase core a potential DC flux must flow via the tank to close the flux path. Therefore the magnetic resistances which represent the gaps between core and tank (R_7) are an important parameter for this core type.

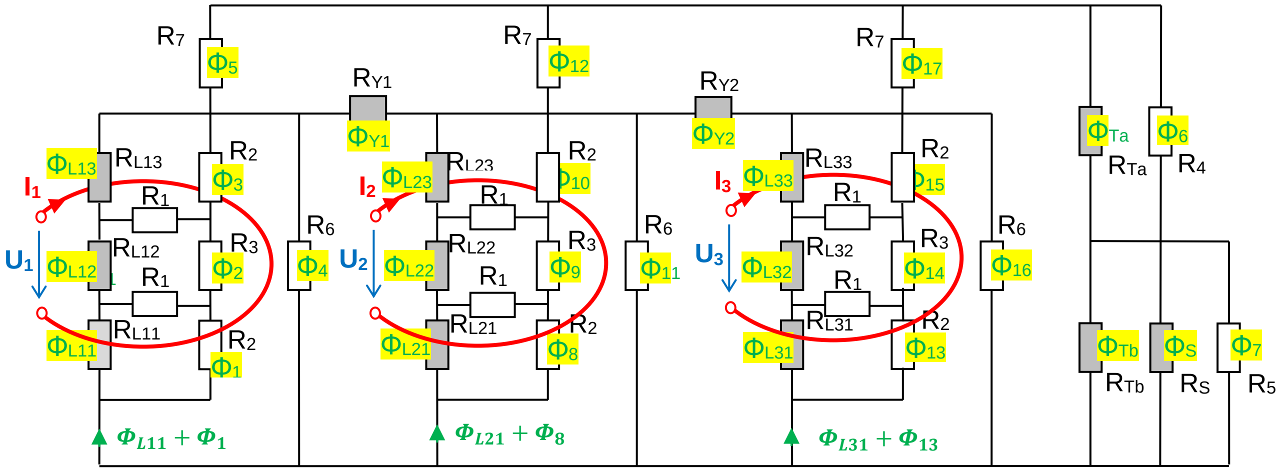
R7
Φ5
RY1
ΦY1
R7
Φ12
RY2
ΦY2
R7
Φ17
ΦTa
Φ6
RTa
R4
ΦL13
RL13
R2
Φ3
I1
R1
U1
ΦL12
RL12
R3
Φ2
R1
ΦL11
RL11
R2
Φ1
R6
Φ4
ΦL23
RL23
R2
Φ10
I2
R1
U2
ΦL22
RL22
R3
Φ9
R1
ΦL21
RL21
R2
Φ8
R6
Φ11
ΦL33
RL33
R2
Φ15
I3
R1
U3
ΦL32
RL32
R3
Φ14
R1
ΦL31
RL31
R2
Φ13
R6
Φ16
ΦTb
RTb
ΦS
RS
Φ7
R5
$\Phi_{L11} + \Phi_1$
$\Phi_{L21} + \Phi_8$
$\Phi_{L31} + \Phi_{13}$

Figure 34: Electro-magnetic network for transformers with a T3 Core-Type

4.3.1.2 Electro-magnetic network for Core-Type T5

Figure 35 represents a suitable network if a T5 core is used for a three-phase transformer. The basis of this structure is the network of a T3 Core-Type. The difference of the T5 core design are the return limbs which are modeled with the magnetic resistances R_{RL1} and R_{RL2}. However, the individual phases of a T5 core transformer are coupled via the yokes under DC excitation. In order to model this coupling in an accurate manner, also the tank cover is covered in the network structure of a T5 core with suitable magnetic resistances.

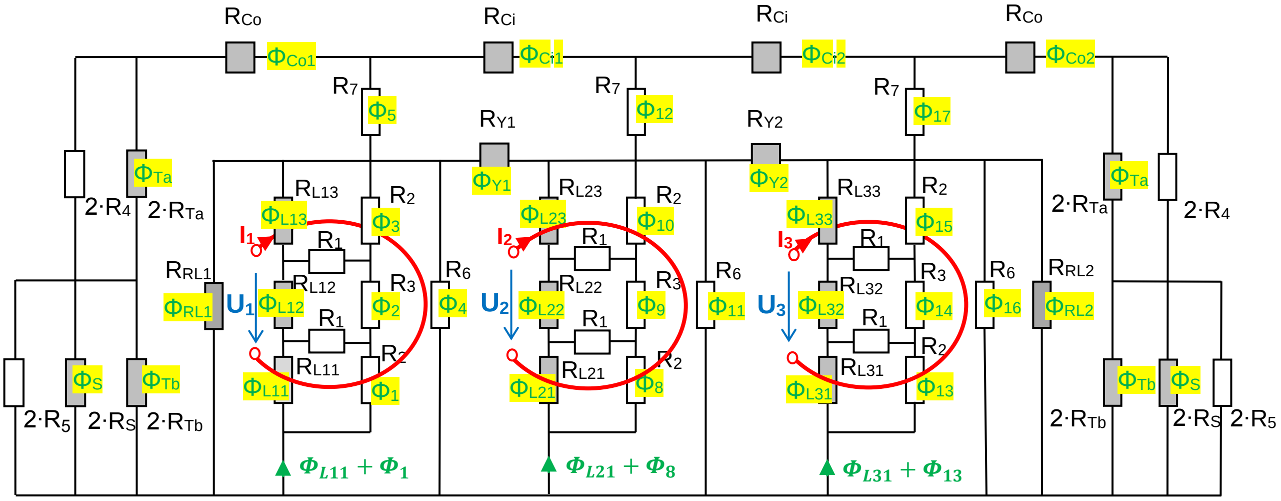
RCo
ΦCo1
RCi
ΦCi1
RCi
ΦCi2
RCo
ΦCo2
R7
Φ5
RY1
ΦY1
R7
Φ12
RY2
ΦY2
R7
Φ17
ΦTa
2·R4
2·RTa
ΦTa
2·RTa
2·R4
RRL1
ΦRL1
RL13
ΦL13
R2
Φ3
I1
R1
U1
ΦL12
RL12
R3
Φ2
R1
R2
ΦL11
RL11
Φ1
R6
Φ4
RL23
ΦL23
R2
Φ10
I2
R1
U2
ΦL22
RL22
R3
Φ9
R1
R2
ΦL21
RL21
Φ8
R6
Φ11
RL33
ΦL33
R2
Φ15
I3
R1
U3
ΦL32
RL32
R3
Φ14
R1
R2
ΦL31
RL31
Φ13
R6
Φ16
RRL2
ΦRL2
ΦS
ΦTb
2·R5
2·RS
2·RTb
ΦTb
ΦS
2·RTb
2·RS
2·R5
$\Phi_{L11} + \Phi_1$
$\Phi_{L21} + \Phi_8$
$\Phi_{L31} + \Phi_{13}$

Figure 35: Electro-magnetic network for transformers with a T5 Core-Type

4.3.2 Analysis

By the help of the above mentioned electro-magnetic networks the behavior of two different three-phase transformers is studied with different DC levels in their high-voltage windings. Table 13 illustrates the main technical data of the transformers under investigation and Table 14 their design-specific parameter.

Table 13: Three-phase transformers under investigation

Transformer	Core-Type	Frequency	Rated voltage and core flux density	Power
Unit 4	T3	50 Hz	434 kV (1.7 Tesla)	320 MVA
Unit 5	T5	60 Hz	345 kV (1.7 Tesla)	600 MVA

Table 14: Design-specific parameter of three-phase transformers under investigation (lengths in the table are in [m], cross sections are in [m²])

Parameter	Unit 4	Unit 5	Parameter	Unit 4	Unit 5
L_1	2.400	2.900	L_{11}	0.310	0.259
L_2	0.850	0.580	D_C	0.866	1.034
L_3	2.280	2.060	D_I	0.912	1.180
L_4	-[2]	0.820	D_O	1.094	1.802
L_5	2.895	2.700	A_C	0.539	0.754
L_6	8.500	8.295	A_Y	0.539	0.429
L_7	4.280	4.200	A_{RL}	-[2]	0.378
L_8	2.820	-[2]	A_S	0.068	-[2]
L_9	0.082	0.100	d_w	0.010	0.010
L_{10}	0.803	0.982	N_{turns}	1232	632

In analogous to the analysis at single-phase transformers in chapter 4.2.3, the behavior of the DC flux is analyzed first. Table 15 and Table 16 demonstrate the distribution of the DC flux in the corresponding network structures for different DC currents in the windings of the investigated three-phase transformers.

Table 15: DC flux distribution [in Vs] of Unit 4 (Core-Type T3)

Branch	5 A DC	10 A DC	20 A DC	30 A DC	50 A DC	100 A DC
$\Phi_{L11} + \Phi_1$	0,071	0,131	0,184	0,216	0,266	0,362
$\Phi_{L21} + \Phi_8$	0,071	0,131	0,184	0,216	0,266	0,362
$\Phi_{L31} + \Phi_{13}$	0,071	0,131	0,184	0,216	0,266	0,362
$\Phi_{Y1} = -\Phi_{Y2}$	0,000	0,000	0,000	0,000	0,000	0,000
$\Phi_5 = \Phi_{12} = \Phi_{17}$	0,047	0,087	0,121	0,142	0,173	0,233
$\Phi_4 = \Phi_{11} = \Phi_{16}$	-0,023	-0,044	-0,063	-0,074	-0,093	-0,130

---

[2] This parameter not required for the selected transformer design.

Table 16: DC flux distribution [in Vs] of Unit 5 (Core-Type T5)

Branch	5 A DC	10 A DC	20 A DC	30 A DC	50 A DC	100 A DC
$\Phi_{L11} + \Phi_1$	0,205	0,230	0,260	0,288	0,332	0,416
$\Phi_{L21} + \Phi_8$	0,177	0,209	0,241	0,263	0,300	0,370
$\Phi_{L31}+\Phi_{13}$	0,203	0,230	0,263	0,289	0,332	0,416
$\Phi_{Y1} = -\Phi_{Y2}$	0,083	0,096	0,107	0,115	0,126	0,146
Avg(Φ_5,Φ_{12},Φ_{17})	0,007	0,009	0,012	0,014	0,018	0,023
Avg(Φ_4,Φ_{11},Φ_{16})	-0,004	-0,006	-0,011	-0,015	-0,024	-0,046
$\Phi_{RL1} = \Phi_{RL2}$	-0,277	-0,311	-0,349	-0,376	-0,420	-0,498

It can be seen from these tables that the DC flux distribution in a T3 Core-Type and a T5 Core-Type transformer is significant different. In a T3 core transformer the generated DC flux returns mainly via the tank elements whereas the yokes are almost DC free. In a T5 core transformer the major part of the DC flux is split between the yokes and the returns limbs. Consequently, also the saturation behavior between these cores is different as demonstrated in Figure 36.

The left part of the figure shows the behavior for the T3 core and the right part the performance for the T5 core. In the T3 unit only the three limbs exceed the saturation level during a section of the time period whereas in the T5 type also the yokes and return limbs are partly saturated (time periods marked with thicker lines). This has also an influence on the wave form of the exciting current. The currents of both transformers have major peaks during the saturation periods of the main limbs, but the current in the T5 unit has additional peaks during the saturation periods of the yokes and the return limbs. A further difference between both currents is that the current of the T3 unit has an offset in the wave form. The reason of this offset is that transformers with such a T3 core need a certain amount of a DC current in their windings to reach the saturation level. This contrasts with T5 core transformers, because here saturation starts already at very low DC levels.

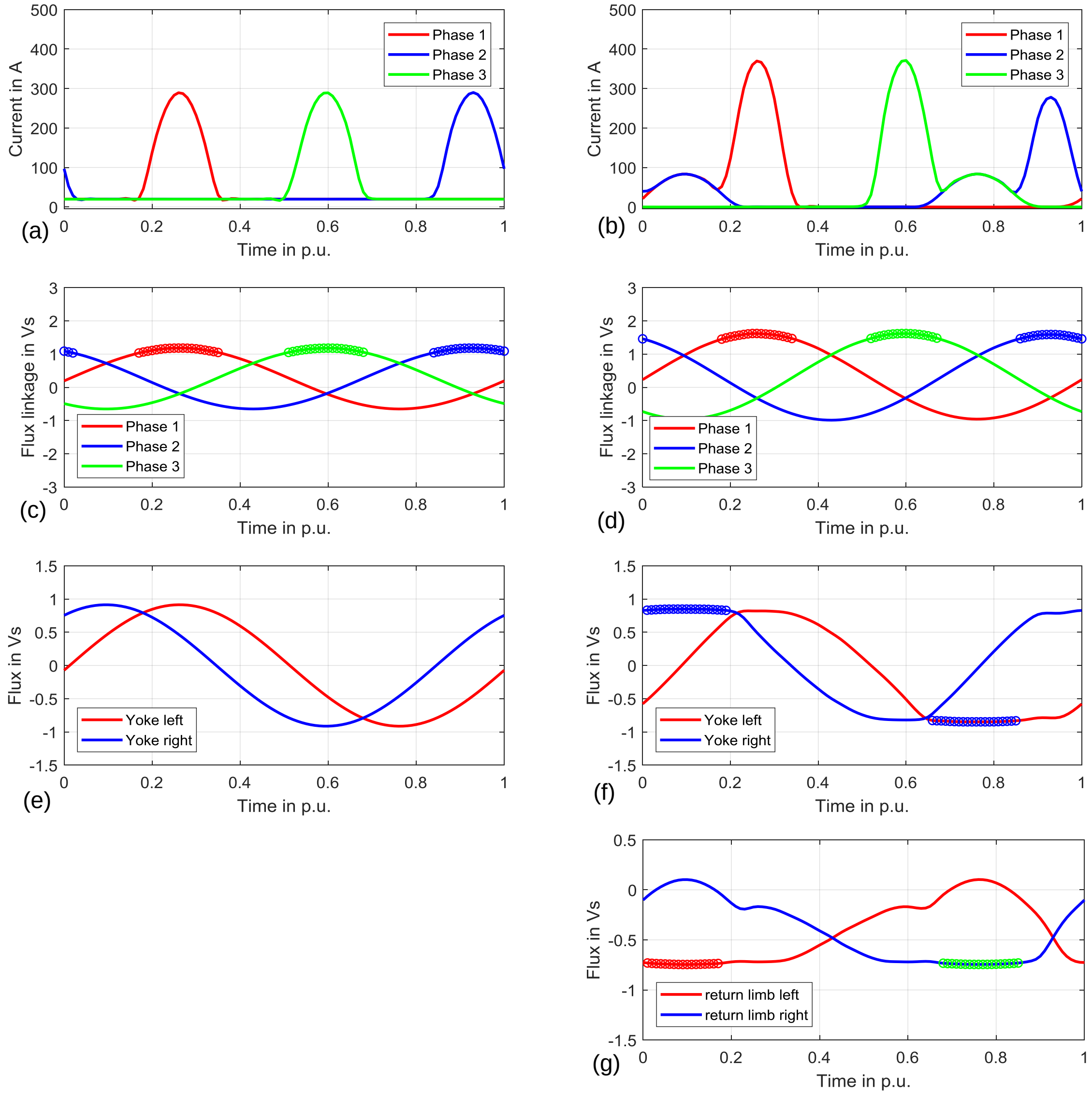

Figure 36: Core saturation in T3 and T5 Core-Type transformers due to DC – (a) Exciting current of a (a) T3 Core-Type and (b) T5 Core-Type, Saturation of main limbs at a (c) T3 Core-Type and (d) T5 Core-Type, Saturation of yokes in a (e) T3 Core-Type and a (f) T5 Core-Type, (g) Saturation of return limbs of a T5 Core-Type

To compare the harmonic behavior of these core designs, Figure 37 shows the increase of the fundamental of the exciting current and of the first five harmonics with the DC level. The DC current where the rise of the harmonics starts is significant different between the transformers. The increase of the harmonics starts with a T5 Core-Type with about zero, whereas the harmonic occurrence by a T3 Core-Type transformer begins always at a higher DC level. Furthermore, in the T3 Core-Type transformer the starting point of the saturation depends strongly on the AC flux density. With 1.7 Tesla, the fundamental of the T3 Core-Type transformer starts to increase with a DC level of about 10 A DC per phase. If the AC flux density in the same transformer is only 1.2 Tesla, then the saturation effects start not before 30 A DC per phase. However, if the saturation level is reached, then the behavior of the harmonics is comparable. All in all T3 Core-Type transformers have an increased DC capability compared with T5 Core-Types, but saturation is also at T3 cores relatively easily possible.

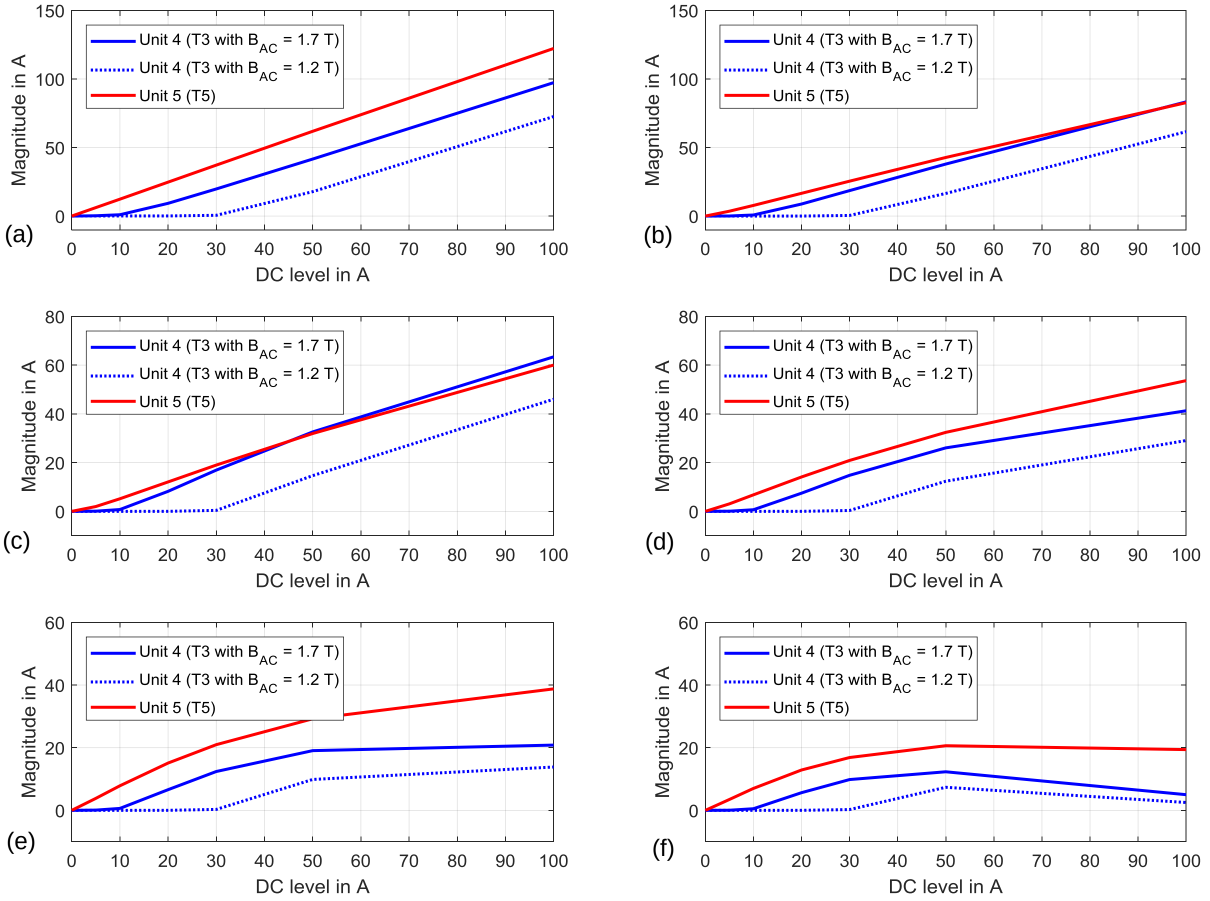

Figure 37: Harmonics of exciting current due to DC at three-phase transformers – RMS value of (a) Fundamental, (b) 1st harmonic, (c) 2nd harmonic, (d) 3rd harmonic, (e) 4th harmonic, (f) 5th harmonic

4.4 Verification

4.4.1 DC experiments with single-phase transformers

4.4.1.1 Measurement setup

DC experiments with different transformers were carried out in a high-voltage laboratory in order to verify the developed electro-magnetic modeling technique. Different setups of such test circuits are discussed in [32].

Figure 38 demonstrates a test circuit which was used for tests with single-phase transformers. The rated voltage of two identical transformers is applied to the low-voltage terminals, the high-voltage terminals are connected, and in the common neutral of the high-voltage windings is a DC source installed to inject different DC currents into the windings. To ensure that the DC current flows into the windings an ohmic resistance is needed between the ground and the neutral in one of the transformers.

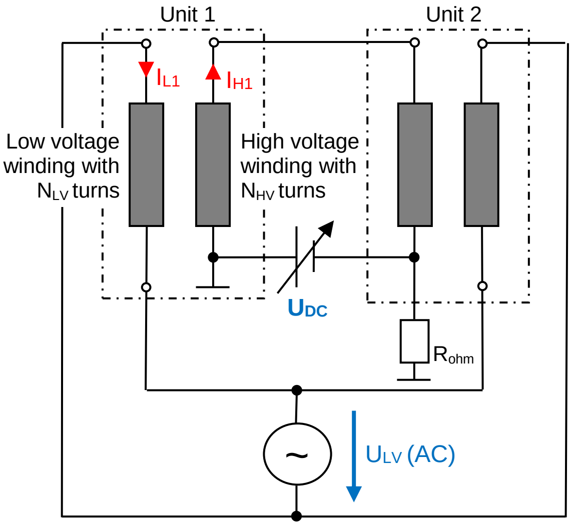
Unit 1
Unit 2
I_{L1}
I_{H1}
Low voltage winding with N_{LV} turns
High voltage winding with N_{HV} turns
U_{DC}
R_{ohm}
~
U_{LV} (AC)

Figure 38: Sketch of a DC test circuit

To identify the exciting current of an individual transformer in such a test circuit both winding currents I_{L1} and I_{H1} must be measured. Figure 39 demonstrates an example of such measured currents during a DC test. It can be seen, that the high-voltage winding and the low-voltage winding contribute to the transformer excitation. A simplified equivalent circuit diagram of a transformer is shown in Figure 40 and explains the determination of the exciting current. It can be calculated with

$$I_{ex,H} = \frac{N_{LV}}{N_{HV}} \cdot I_{L1} + I_{H1} \tag{16}$$

where N_{HV} is the number of high-voltage turns and N_{LV} and number of the low-voltage turns.

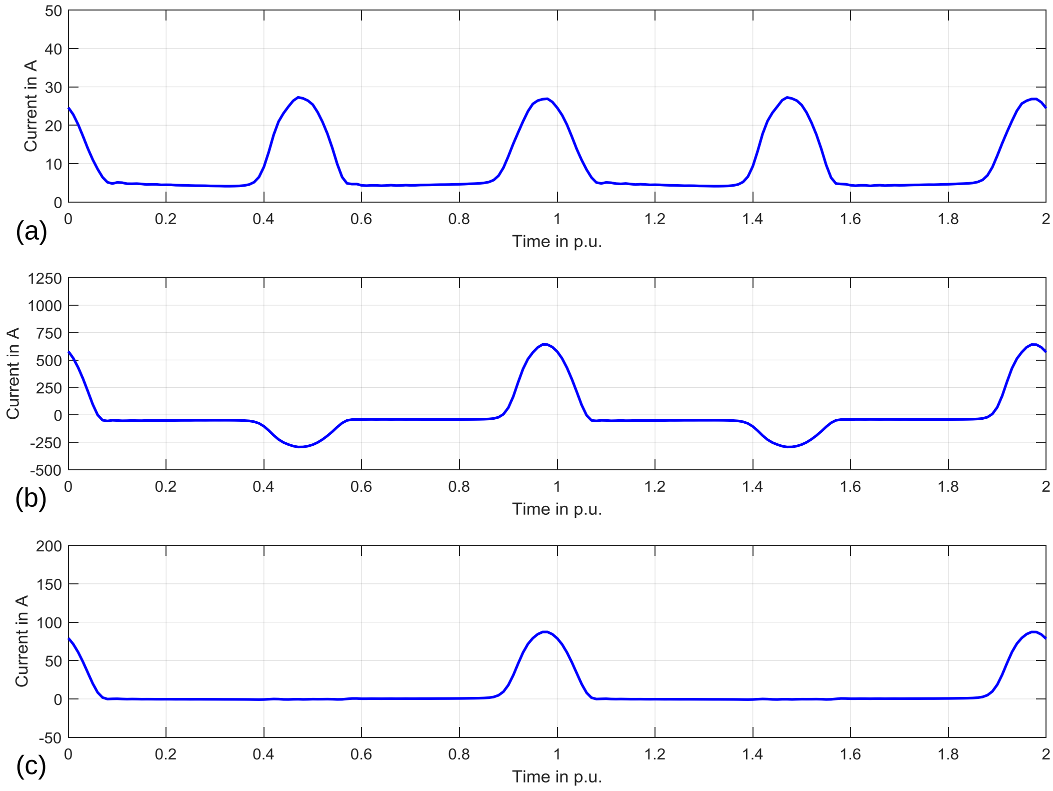

Figure 39: Measured currents: (a) I_{H1} – of high-voltage winding, (b) I_{L1} – of low-voltage winding, (c) $I_{ex,H}$ – Exciting current

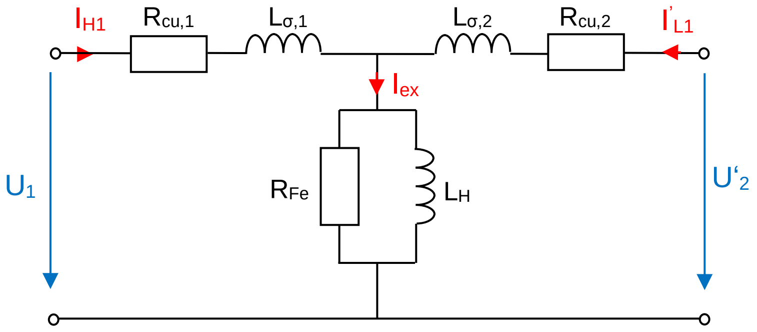

Figure 40: Equivalent circuit diagram of a transformer[3]

4.4.1.2 Comparison of test results with simulations

Two single-phase transformers with different core designs have been tested with the test circuit of Figure 38. Table 17 shows the main technical data of the tested transformers.

Table 17: Technical data of tested single-phase transformers

Meas. No.	Transformer	Core-Type	Frequency	Rated voltage and core flux density	Power
1	Unit 1	T1	60 Hz	230/√3 kV (1.72 Tesla)	133 MVA
2	Unit 2	T4	50 Hz	405/√3 kV (1.69 Tesla)	570 MVA

Figure 41 compares the measured exciting currents with the simulated ones using the electromagnetic calculation models of chapter 4.2 in this thesis. The graphic shows, that the simulations at both units show significant higher and thinner peaks than the measurements. The FFT analysis of these currents is given in Table 18 and Figure 42. It can be seen, that the magnitudes of the individual frequency components are in the simulation higher than in the measurement and especially the higher harmonics differ significantly.

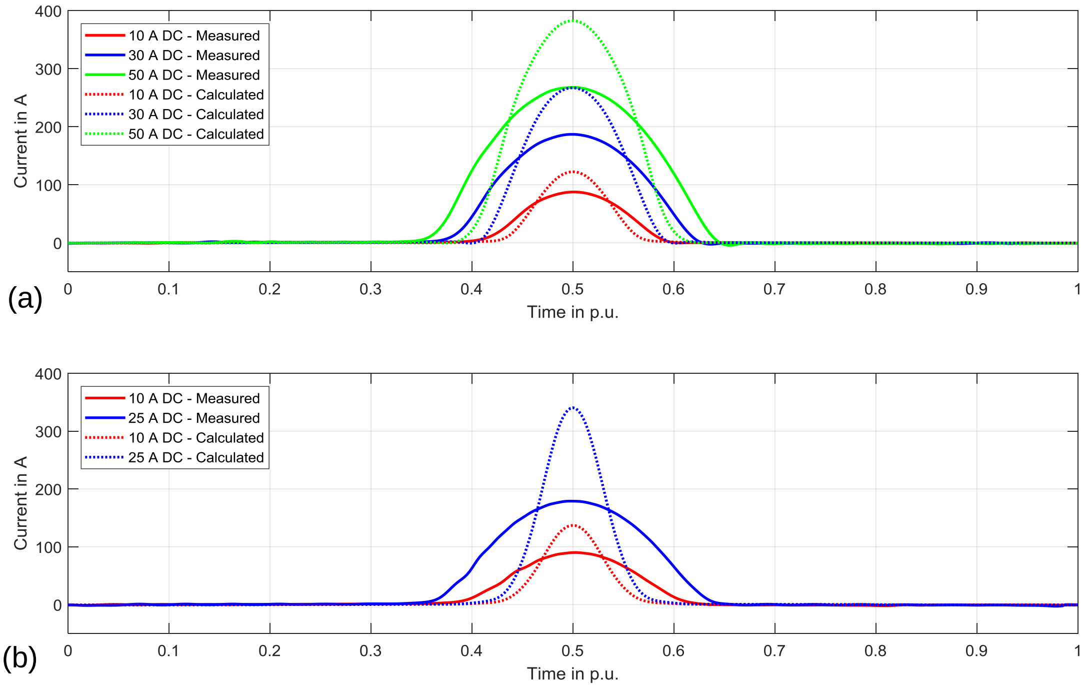

Figure 41: Measured vs. simulated exciting currents at (a) Unit 1 and (b) Unit 2

---

[3] Capacitances are neglected in this circuit diagram.

Table 18: Harmonic analysis – Measurement vs. Simulation

	DC	fundamental		1st harmonic		2nd harmonic		3rd harmonic		4th harmonic		5th harmonic	
	A	Meas.	Calc.	Meas.	Calc.	Meas.	Calc.	Meas.	Calc.	Meas.	Calc.	Meas.	Calc.
Unit 1	10	13,8	14,0	12,2	13,1	10,2	11,9	7,8	10,5	5,4	8,9	3,3	7,2
	20	27,1	27,7	23,2	25,6	17,9	22,6	12,1	19,0	6,6	15,0	2,3	11,0
	30	40,1	41,3	33,1	37,5	23,7	32,1	13,9	25,6	5,5	18,7	0,3	12,1
	40	52,8	54,7	42,1	49,0	28,0	40,8	14,1	31,0	3,3	21,0	2,8	12,0
	50	65,3	68,0	50,5	59,9	31,5	48,2	13,5	34,8	0,9	21,6	5,0	10,3
Unit 2	5	7,4	7,3	6,4	6,4	5,6	5,9	4,5	5,3	3,4	4,5	2,5	3,8
	10	14,3	14,2	12,5	13,0	10,6	12,0	8,3	10,7	5,8	9,3	3,9	7,8
	20	27,6	28,1	23,7	26,3	18,8	24,3	13,5	21,7	8,0	18,9	3,9	15,9
	25	34,7	35,1	29,5	32,9	22,7	30,2	15,5	27,0	8,4	23,3	3,1	19,5

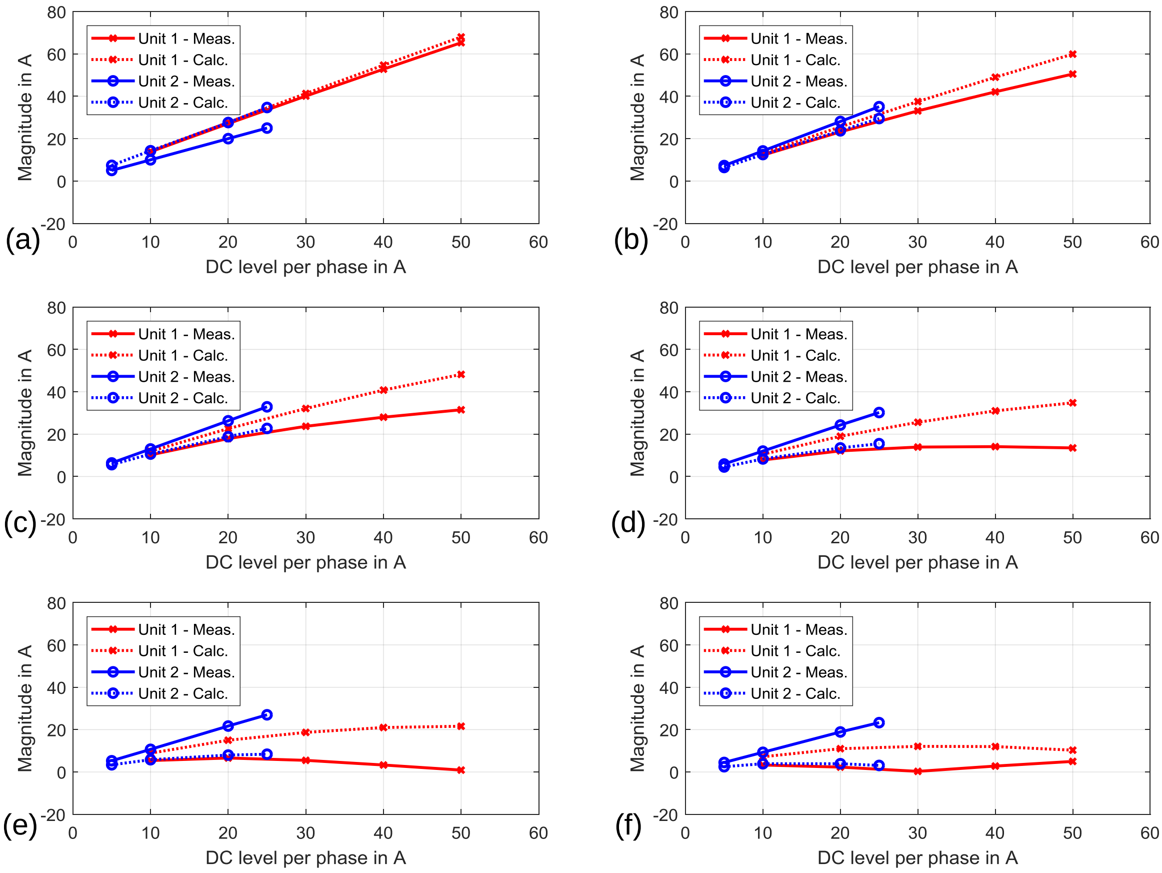

Figure 42: Increase of harmonics with DC (Measurement vs. Simulation) – RMS value of (a) Fundamental, (b) 1st harmonic, (c) 2nd harmonic, (d) 3rd harmonic, (e) 4th harmonic, (f) 5th harmonic

The reason for the deviations between the measurements and the simulations is given by the experimental setup. An analysis of the test circuit pointed out that the supply voltage was not sinusoidal during the test. This is in contrast to the simulation results which are shown in Figure 41 and Figure 42, because these simulations assumed pure sinusoidal voltages on the winding terminals. Figure 43 demonstrates the difference between the assumed voltages and the measured voltages during the DC experiments. A significant down-turn in the wave form can be observed compared with a pure sinusoidal shape. This phenomenon is caused by a voltage drop in the synchronous generator due to the high peaks in the exciting current.

Accordingly it was not possible to deliver pure sinusoidal voltages during the DC experiments. Therefore, these voltage fluctuations must be taken into account by the verification of the simulation models. The results of this verification are demonstrated with Figure 44. The figure compares the measurement data with a second simulation where the measured voltage wave forms are used as input for the calculations. The consideration of the correct voltage leads to a much better correlation between the measurement and the simulation. Consequently, the simulation models calculate the exciting currents under DC in an accurate manner. However, this shows that the consideration of potential voltage fluctuations is essential and may be also important if GIC scenarios in power systems are studied, because during real GIC events the voltage may be also influenced and not fully sinusoidal. Simulations which neglect such variations in the voltage will lead to different frequency components in the currents and especially the magnitudes of the higher harmonics will be calculated differently.

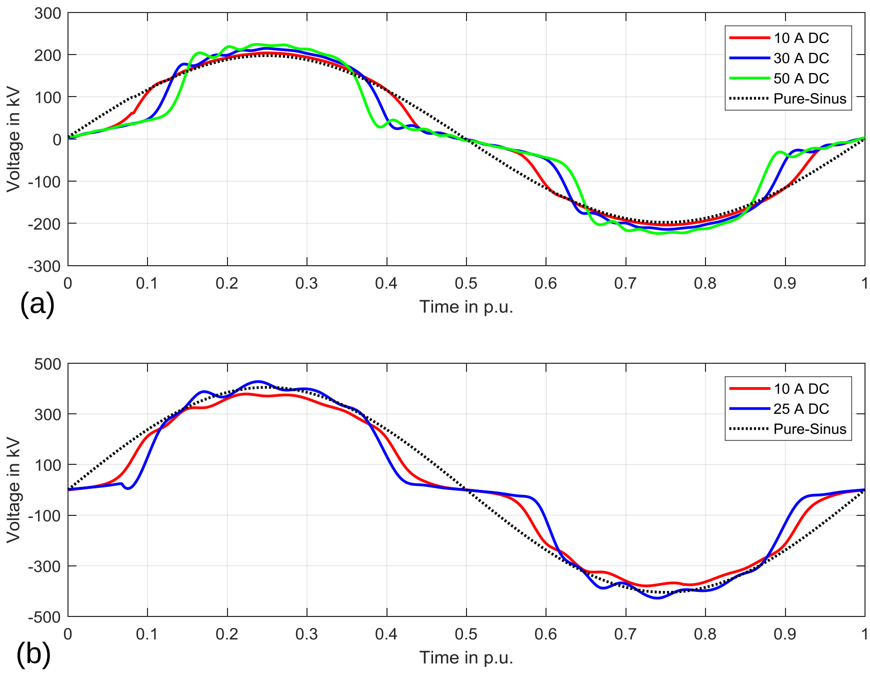

Figure 43: Measured voltages during DC experiment at (a) Unit 1 and (b) Unit 2

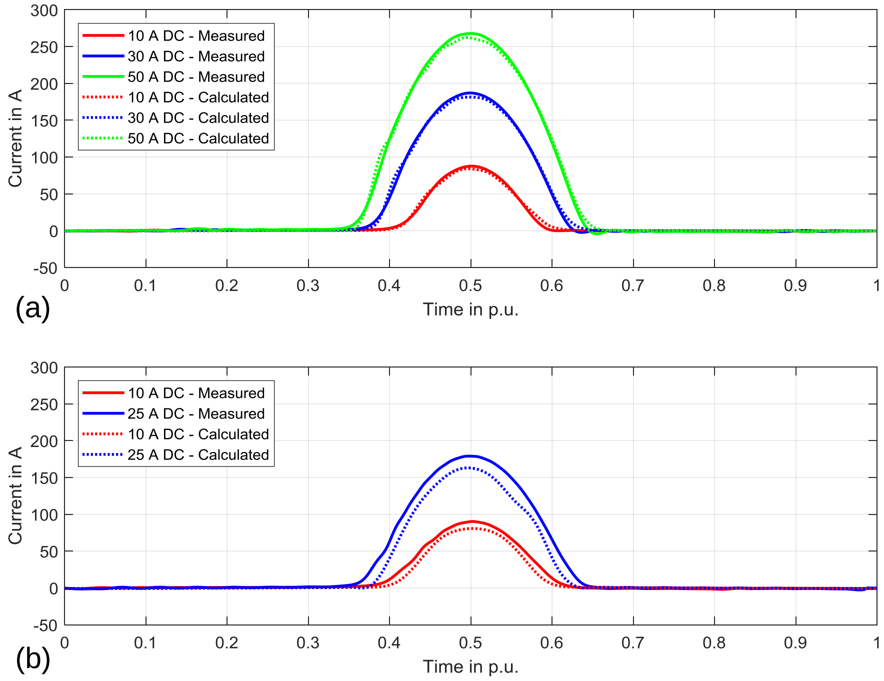

Figure 44: Measured vs. simulated exciting currents using measured voltage at (a) Unit 1 and (b) Unit 2

4.4.2 DC experiments with 3-phase transformers (T3 Core-Types)

4.4.2.1 Measurement setup

In addition to the DC experiments with single-phase transformers DC tests with 3-phase transformers were also carried out in the high-voltage laboratory. Figure 45 demonstrates the used electrical circuit to test two transformers with a T3 Core-Type. It can be seen, that two units are needed, and that the DC source is located between both high-voltage neutrals. Consequently, each transformer is exposed to the DC current during the test.

However, the main idea of such a DC experiment is that only one transformer reaches core saturation (test object) and that the saturation effects of the second unit (auxiliary transformer) are negligible in order to measure only the DC effects of the test object. To achieve this ambition the auxiliary transformer must has a T3 core design, because transformers with T5 cores reach the saturation level at much lower DC levels than units with T3 cores. However, if both transformers in the test circuit have a T3 core, then it must be additionally ensured that the nominal AC flux density in the auxiliary unit is significantly lower than the AC flux density in the test object. In this way it can be achieved that only the test object gets into saturation.

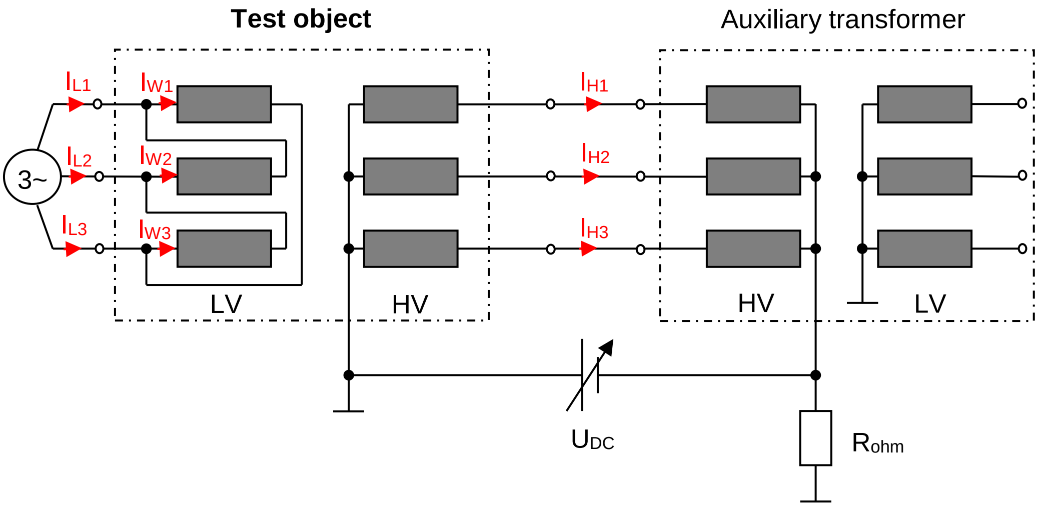

Figure 45: Test circuit for DC experiments with T3 Core-Type transformers

Chapter 4.4.1.1 demonstrated that the exciting current of an individual transformer in a DC test circuit is determined with components from both systems (Equation (16)). This effect must be also considered for the test object in Figure 45. The circuit shows that the voltage is applied on the low-voltage system of the test object and consequently the AC components of the exciting current are flowing in the low-voltage winding. The high-voltage winding carries only the DC component together with the exciting current of the auxiliary transformer. Examples for occurring current wave forms during such a DC test are demonstrated in Figure 46.

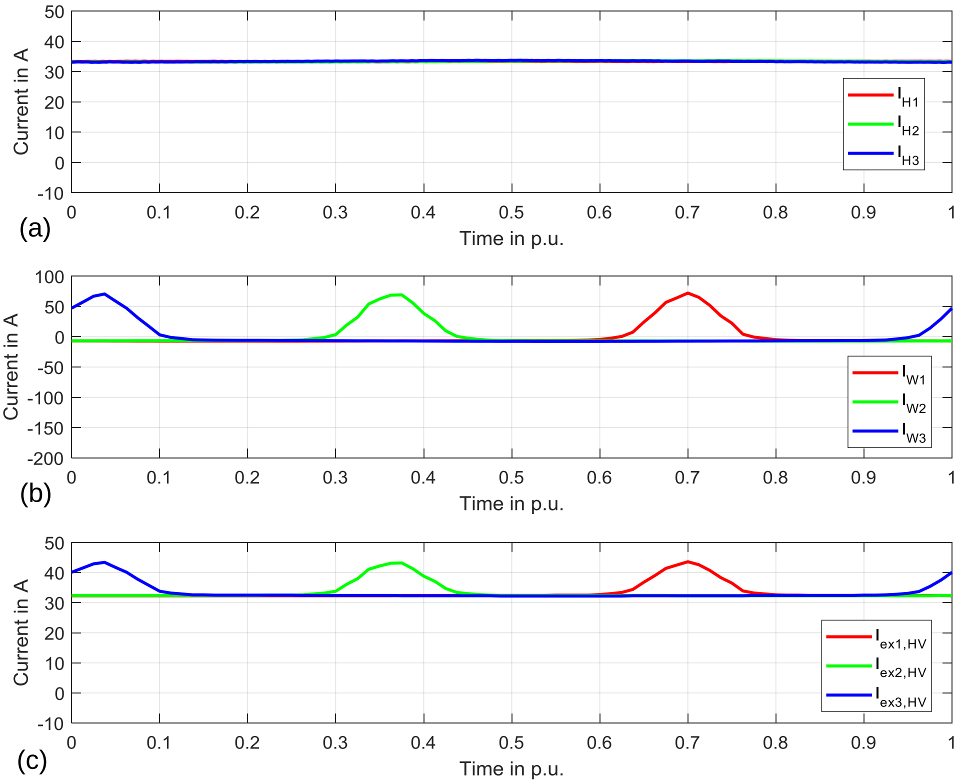

Figure 46: Currents in test circuit for the T3 Core-Type transformer: (a) $I_{H1,2,3}$ – high-voltage winding, (b) $I_{W1,2,3}$ – low-voltage winding, (c) $I_{ex1,2,3,HV}$ – Exciting current

4.4.2.2 Comparison of test results with simulations

In order to verify the electro-magnetic network model for T3 Core-Types which is shown in chapter 4.3.1.1 of this document, two different 3-phase transformers with this core design have been tested by the help of the discussed test circuit of Figure 45. Table 19 shows the main technical data of these tested transformers. It can be seen from the table, that Unit 2 was tested twice at two different voltage levels. The reason was to study the transformer behavior with two different AC flux densities in the core (1.7 Tesla and 1.2 Tesla).

Table 19: Technical data of tested three-phase transformers with a T3 Core-Type

Meas. No.	Transformer	Core-Type	Frequency	Rated voltage and core flux density	Power
1	Unit 1	T3	50 Hz	440 kV (1.70 Tesla)	330 MVA
2	Unit 2	T3	50 Hz	434 kV (1.70 Tesla)	320 MVA
3	Unit 2	T3	50 Hz	306 kV (1.20 Tesla)	320 MVA

Figure 47 and Figure 48 compare for both units the measured supply currents with the calculated ones for two DC levels which caused core saturation during the experiments. The simulations correlate well with the measurement data.[4] This indicates that the demonstrated electro-magnetic calculation model is suitable to simulate the wave form of the exciting current under core saturation.

---

[4] It must be noted that the demonstrated calculation model in chapter 4.3.1.1 calculates the exciting current based on the high-voltage winding of the transformer. In order to compare the measured supply current of the low-voltage side, the calculated exciting current must be recalculated to the low-voltage system. However, this can be easily done by the help of the turn ratio between both windings.

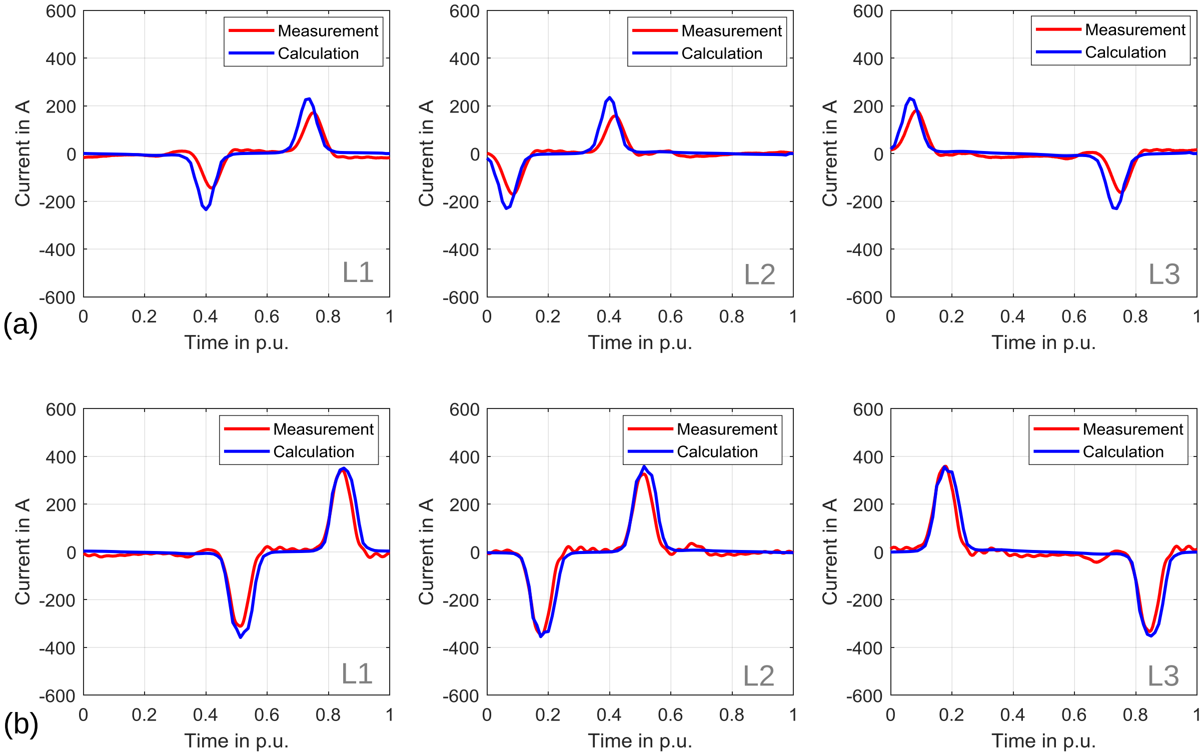

Figure 47: Supply current of each phase in Unit 1 with (a) 75 A DC in neutral and (b) 90 A DC in neutral

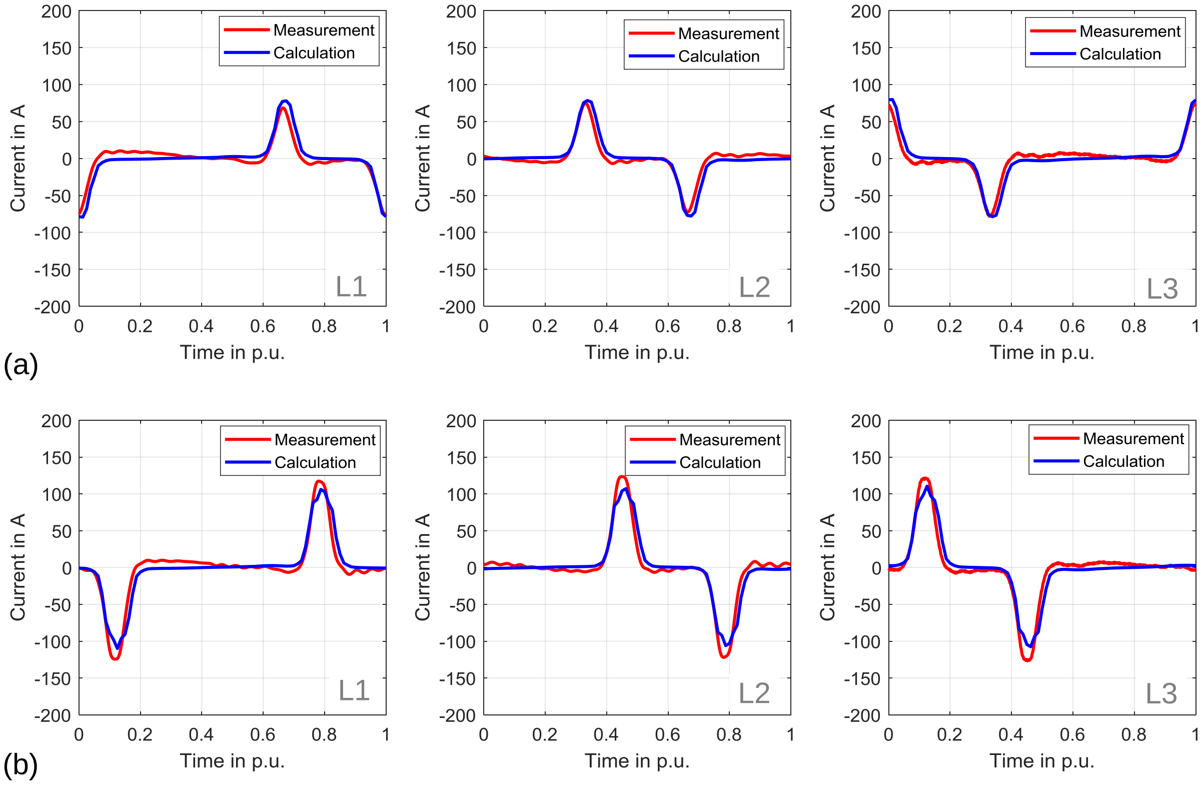

Figure 48: Supply current of each phase in Unit 2 with (a) 35 A DC in neutral and (b) 40 A DC in neutral

4.4.2.3 Behavior of fundamental reactive power

Several DC levels were injected in the high-voltage windings of these transformers in order to measure the minimal required DC level to reach the saturation point where the reactive power and the harmonics start to increase. The results are demonstrated in Figure 49. The figure shows the measured reactive power consumption with the corresponding calculation. The total fundamental reactive power of the transformer is calculated with the sum over all phases and is given with

$$Q = U_{HV,1-60Hz} \cdot I_{ex,1-60Hz} + U_{HV,2-60Hz} \cdot I_{ex,2-60Hz} + U_{HV,3-60Hz} \cdot I_{ex,3-60Hz} \tag{17}$$

where $I_{ex,1,2,3-60Hz}$ are the RMS values of the exciting current fundamental in each phase and $U_{HV,1,2,3-60Hz}$ the RMS value of the voltage fundamental at the high-voltage terminals. Also Figure 49 shows a good correlation between measurement and simulation.

The analysis of this data shows that the DC level where the harmonic increase starts, differs significantly between Unit 1 and Unit 2, even though both units have the same AC flux density of 1.7 Tesla in the core. The increase of the reactive power of Unit 1 starts not before about 50 A DC in the neutral whereas the starting point of Unit 2 is already at 20 A DC in the neutral. Furthermore it can be seen from the measurements, that the AC flux density influences significantly the starting point of the harmonic generation. With an AC flux density of 1.7 Tesla, the minimal DC level to achieve the core saturation is only about 20 A DC per phase in Unit 2. With a lower AC flux density (1.2 Tesla) the saturation starts in the same Unit 2 not before a DC level of about 85 A DC in the neutral.

The figure shows that such a DC test can be used to identify the DC withstand capability of transformers with a T3 Core-Type. At the one hand the test points out the DC level when the saturation effects are starting in the transformer (e.g. reactive power increase, additional heating, etc.) and on the other hand the validity of the calculation model and their major parameters (e.g. saturation inductance) can be verified.

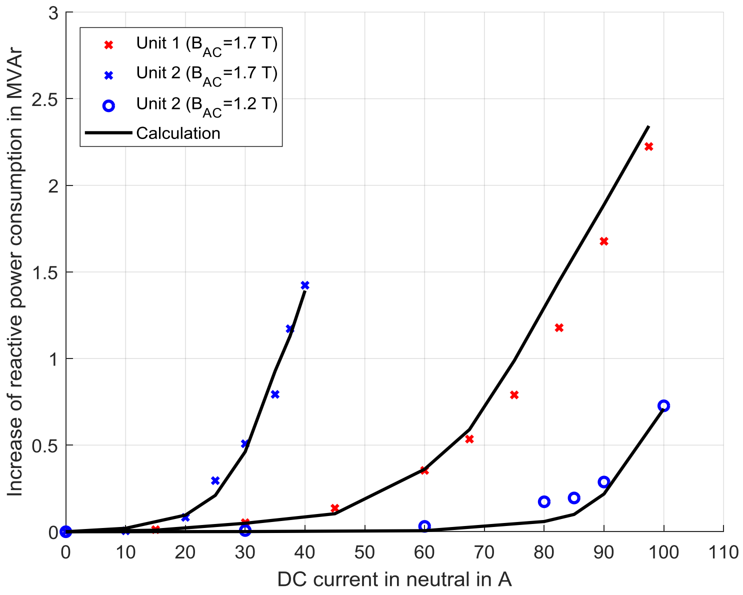

Figure 49: Increase of fundamental reactive power of T3 Core-Type transformers (Measurement vs. Calculation)

4.4.3 DC experiments with 3-phase transformers (T5 Core-Type)

4.4.3.1 Measurement setup

In analogous to the DC experiments with T3 Core-Type transformers a DC test with a T5 Core-Type unit was also done. Figure 50 demonstrates the used test circuit. The connection is similar to the used circuit for the T3 Core-Types (Figure 45), but here the AC voltage is applied on the high-voltage winding of the test object via an auxiliary transformer. The main technical data of the tested T5 Core-Type transformer is given in Table 20.

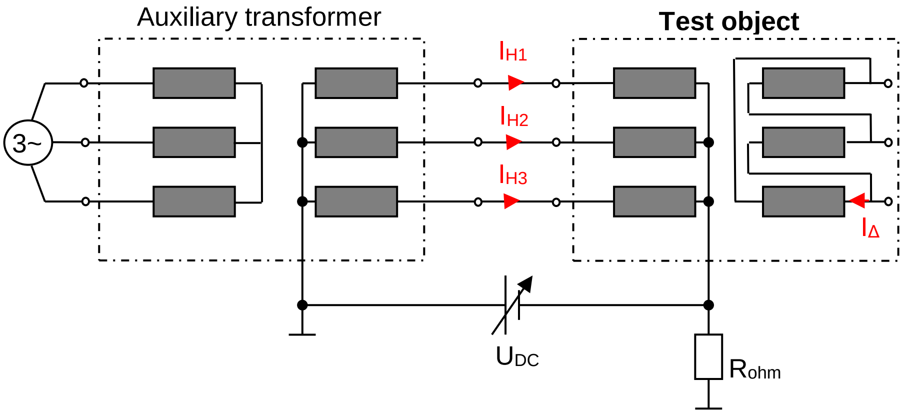

Figure 50: Test circuit for a DC experiment with a T5 Core-Type transformer

Table 20: Technical data of tested three-phase transformer with a T5 Core-Type

Meas. No.	**Transformer**	**Core-Type**	**Frequency**	**Rated voltage and core flux density**	**Power**
1	Unit 1	T5	60 Hz	345 kV (1.70 Tesla)	600 MVA

Figure 51 demonstrates an example for currents in the test circuit of Figure 50 with a DC level of 20 A DC in the neutral. The measured exciting current shows the same shape as the discussed behavior in Figure 36 in chapter 4.3.2. Moderate enhancements in the current in addition to main peaks can be seen. Furthermore a compensating current in the delta winding of the low-voltage system occurs caused by the saturation of the core limbs.

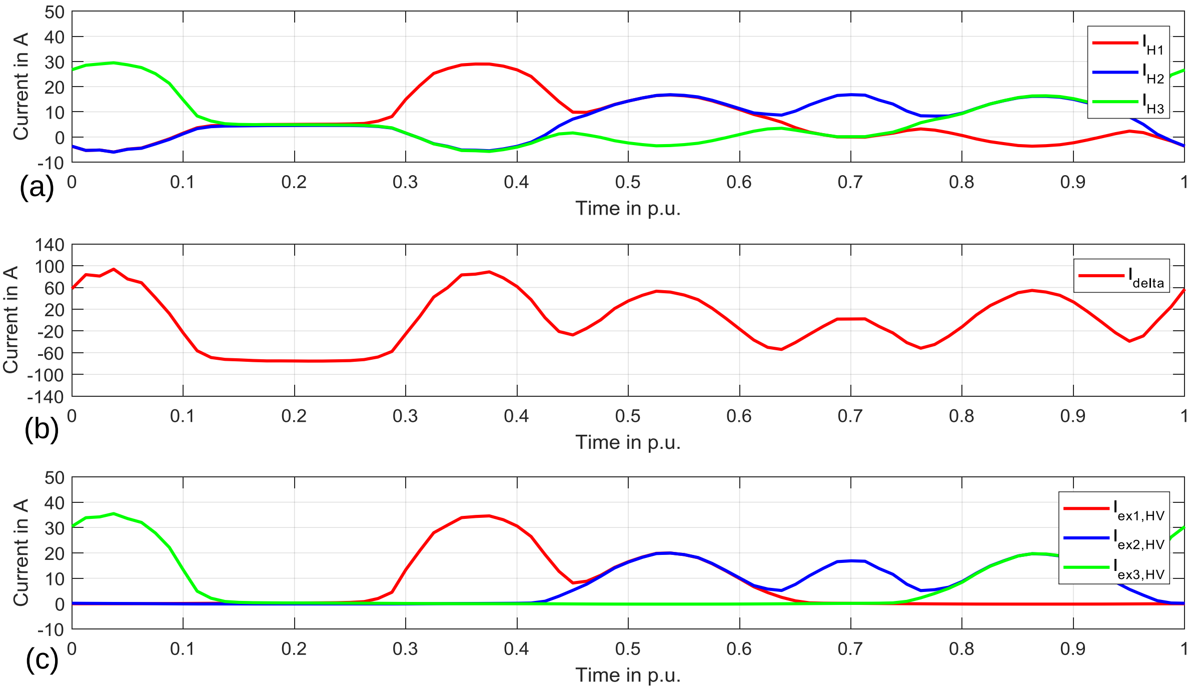

Figure 51: Currents in test circuit for the T5 Core-Type transformer – (a) Current in HV winding, (b) Current in delta winding of LV system, (c) Exciting current with enhancements in addition to the major peaks

4.4.3.2 Comparison of test results with simulations

The purpose of this test was to verify the developed electro-magnetic network for T5 Core-Type transformers. Consequently, the measured exciting currents were compared with the calculated ones. Figure 52 demonstrates the result of this comparison for some tested DC levels in the high-voltage winding of the test object. Also here a good correlation between measurement and calculation results can be seen what indicates a suitable modeling approach.

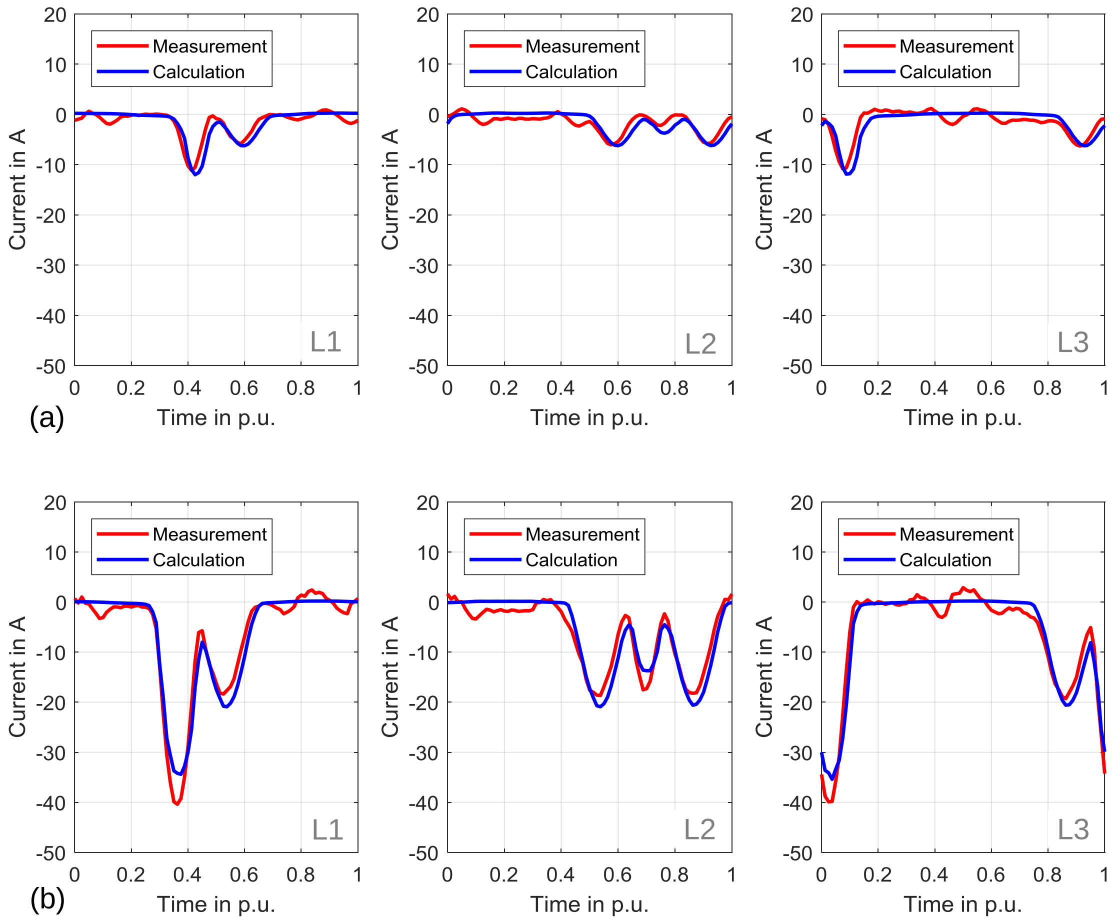

Figure 52: Exciting current of each phase in the tested T5 Core-Type transformer with (a) 5 A DC in neutral and (b) 20 A DC in neutral

4.5 Alternative calculation method based on Ψ-I curve

4.5.1 Calculation procedure for single-phase cores

The chapters 4.1 to 4.4 demonstrated detailed electro-magnetic simulation models for different types of power transformers in order to calculate the exciting current with an additional DC current in the winding. These electro-magnetic models are based on non-linear equation systems which depend on the transformer designs. Based on studies with this modeling technique an easier calculation method could be identified which uses only some basic parameters of the transformers. In that way no non-linear equation systems must be solved and the exciting current can be calculated with a simple calculation tool like MS Excel.

As discussed before in this thesis the exciting current peak of single-phase transformers under DC can be approximated with a Ψ-I curve and the saturation inductance of the excited winding (Figure 32). Consequently this Ψ-I curve can be also used to calculate the wave form of the exciting current for a certain DC level. This simplified approach is demonstrated in Figure 53.

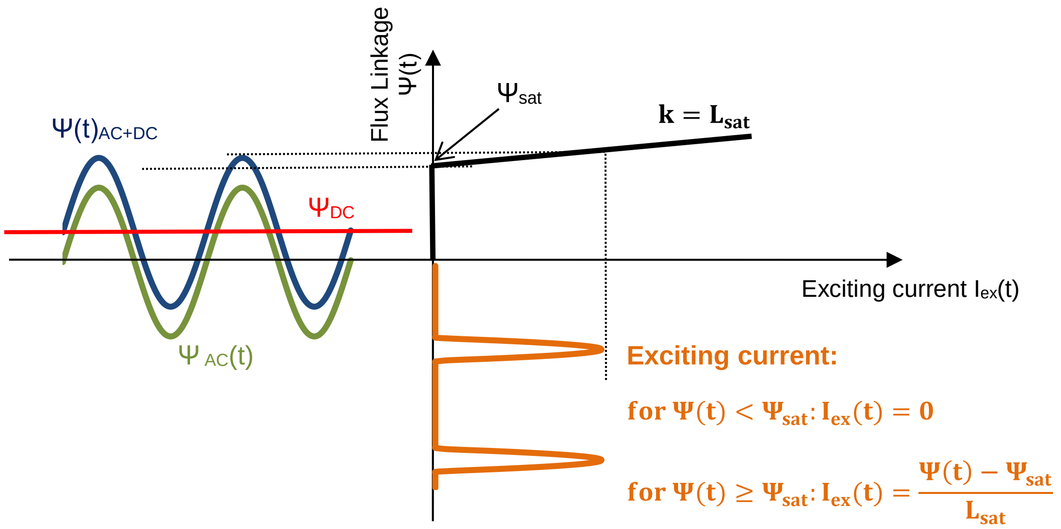

Figure 53: Simplified calculation method for single-phase units

If a DC current flows in the winding, then the flux linkage $\Psi(t)$ of the winding consists of an AC and DC component. This can be expressed as follows:

$$\Psi(t) = \Psi_{AC}(t) + \Psi_{DC} \tag{18}$$

The AC component of the flux linkage Ψ_{AC} is given by the applied sinusoidal voltage[5]:

$$\Psi_{AC}(t) = \frac{\sqrt{2} \cdot U_{RMS}}{2 \cdot \pi \cdot f} \cdot \sin(2 \cdot \pi \cdot f \cdot t) \tag{19}$$

Starting from a certain DC flux linkage Ψ_{DC}, the exciting current $I_{ex}(t)$ can be determined with the equations (20) and (21). If $\Psi(t)$ is lower than the saturation level Ψ_{sat}, then the exciting current $I_{ex}(t)$ is simplified with zero at this moment. Only for time steps where $\Psi(t)$ is higher than Ψ_{sat} the exciting current is determined with the saturation inductance.

$$for\ \Psi(t) < \Psi_{sat}\colon\ I_{ex}(t) = 0 \tag{20}$$

$$for\ \Psi(t) \geq \Psi_{sat}\colon\ I_{ex}(t) = \frac{\Psi(t) - \Psi_{sat}}{L_{sat}} \tag{21}$$

The needed saturation level Ψ_{sat} of the flux linkage can be calculated with

$$\Psi_{sat} = B_{sat} \cdot A_{core} \cdot N_{turns} \tag{22}$$

where B_{sat} represents the flux density where the saturation starts, A_{core} the cross section of the core limb and N_{turns} the number of turns of the excited winding.

From the determined exciting current wave form $I_{ex}(t)$ the DC level can be obtained with:

$$I_{DC} = \frac{1}{T} \cdot \int_0^T I_{ex}(t)\, dt \tag{23}$$

To get now a certain DC level I_{DC}, the DC flux linkage Ψ_{DC} can be adapted until the above-mentioned procedure yields to the desired value of I_{DC}.

---

[5] A pure sinusoidal voltage is assumed.

4.5.2 Calculation procedure for T3 Core-Types

For three-phase transformers with T3 Core-Types an additional parameter is needed for a simplified calculation. It could be shown that for such core designs a certain amount of DC must be applied in the winding the reach core saturation. This causes a more or less constant offset in the wave form of the exciting current (Figure 54). The relationship between this offset in the exciting current and the DC flux linkage can be described with a special inductance named here DC zero-sequence inductance $L_{DC,0}$. That means that before the saturation level is reached the exciting current is given with:

$$for\ \Psi(t) < \Psi_{sat}\colon I_{ex}(t) = \frac{\Psi(t)}{L_{DC,0}} \tag{24}$$

If the saturation level is reached, then the exciting current is given with the saturation inductance as already demonstrated in chapter 4.5.1 for single-phase units. This means with the knowledge of the saturation inductance of the winding and the DC zero-sequence inductance the exciting current of T3 cores can be also easily determined with the same procedure as demonstrated in chapter 4.5.1. The DC flux linkage will be iterative adapted until the desired value of I_{DC} is reached.

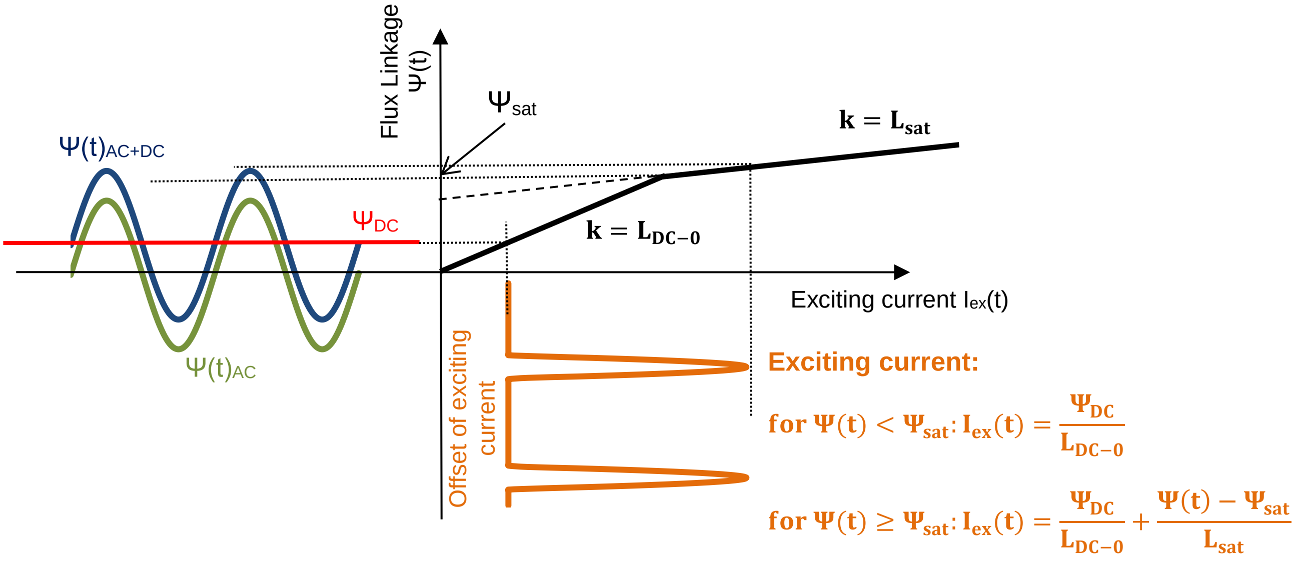
Flux Linkage
$\Psi(t)$
Ψ_{sat}
$\mathbf{k = L_{sat}}$
$\Psi(t)_{AC+DC}$
Ψ_{DC}
$\mathbf{k = L_{DC-0}}$
Exciting current $I_{ex}(t)$
$\Psi(t)_{AC}$
Offset of exciting current
Exciting current:
$\mathbf{for\ \Psi(t) < \Psi_{sat}\colon I_{ex}(t) = \frac{\Psi_{DC}}{L_{DC-0}}}$
$\mathbf{for\ \Psi(t) \geq \Psi_{sat}\colon I_{ex}(t) = \frac{\Psi_{DC}}{L_{DC-0}} + \frac{\Psi(t) - \Psi_{sat}}{L_{sat}}}$

Figure 54: Simplified calculation for three-phase units with a T3 Core-Type

4.5.3 Basic transformer parameter to determine DC behavior

The required transformer parameters for the simplified calculation method are summarized in Table 21. By the help of these basic transformer parameters an easy calculation of the exciting current under DC is possible. It must be noted that the DC zero-sequence inductance of a transformer is not equal with the commonly known zero-sequence inductance. The difference is explained in Figure 55. The zero-sequence inductance describes the condition when the generated flux in the main air leakage path returns via the yokes and the tank. This is in contrast with the DC zero-sequence inductance, which describes the condition when the generated DC flux in the core returns via the tank.

Table 21: Required transformer parameters for a simplified calculation

Symbol	Unit	Description
U_{rms}	V	Applied voltage on winding
f	Hz	Frequency
N_{turns}	-	Number of DC carrying turns
A_{core}	m²	Cross section of main core limb
L_{sat}	H	Saturation inductance of excited winding (≈ Air-core inductance)
$L_{DC,0}$	H	DC zero-sequence inductance
B_{sat}	T	Saturation level of core material (~ 1.95 Tesla)

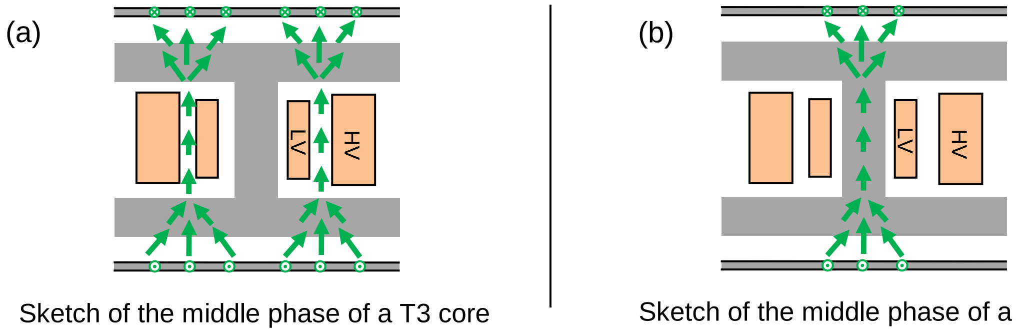

Sketch of the middle phase of a T3 core

Sketch of the middle phase of a T3 core

Figure 55: Zero-sequence impedances: (a) Common phenomenon vs. (b) DC phenomenon

4.6 Comparison of calculation methods and measurements

4.6.1 Single-Phase transformers

The chapters 4.2 and 4.5.1 discussed two possible methods to calculate the wave form of the exciting current with an additional DC current in high-voltage winding for different types of single-phase transformers. Figure 56 compares the results of these two calculation methods together with corresponding measurement results. The demonstrated results in the figure are valid for the tested Unit 1 of Table 17. It can be seen, that for both DC levels in the high-voltage winding, the calculation methods correlate well with the measurement.

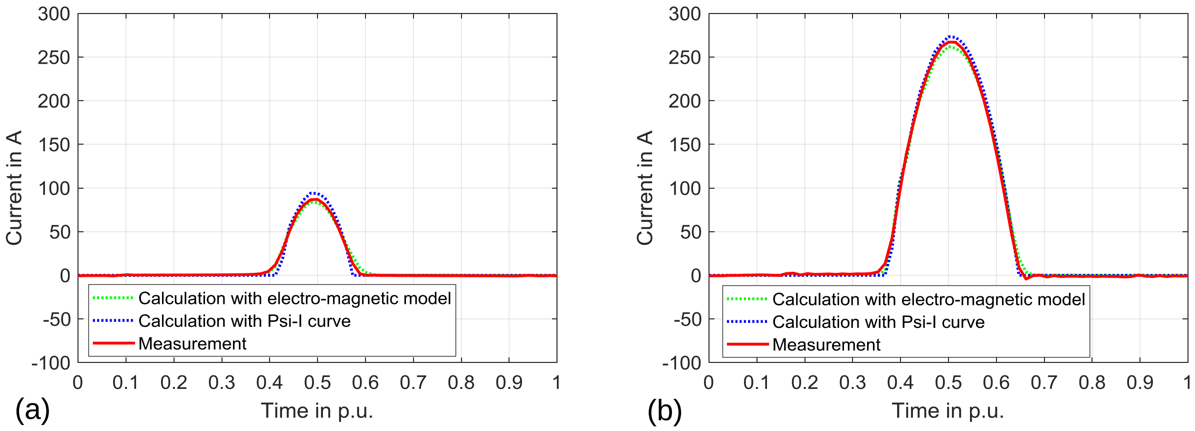

Figure 56: Exciting current of a single-phase transformer determined by different methods with (a) 10 A DC per phase and (b) 50 A DC per phase

4.6.2 Three-Phase transformers with T3 cores

As discussed in chapter 4.5.2 is for three-phase transformers with a T3 core also a simplified alternative calculation method via a Ψ-I curve possible. With this method the exciting current of one individual phase can be determined. However, GIC causes a symmetrical DC distribution within the three phases and the wave form of the exiting current will be almost the same in each phase with a 120-degree phase difference as shown in Figure 46 in chapter 4.4.2.1.

Figure 57 compares the calculated wave forms of the exciting current for one individual phase in a T3 core transformer based on the electro-magnetic model and the Ψ-I curve. In addition also the measured form of the exciting current is demonstrated in the figure. With 3.33 A DC per phase only the DC offset occurs (core saturation is not reached) whereas with 13.33 A DC the saturation level is reached, and all methods show a peak in wave form of the current. However, the Ψ-I approach results in a slightly higher and thinner peak than the measurement and the electro-magnetic model. The reason is that the Ψ-I method considers only two constant inductance values while the electro-magnetic model considers the non-linear behavior of the exciting current very accurately. Therefore the electro-magnetic model correlates well with the measurement. Especially at lower DC levels the electro-magnetic network model is more accurate, whereas at higher DC levels both calculation methods will show similar results. This means that also the Ψ-I method gives a suitable estimation for the wave form of the exciting current, especially for higher DC currents where the core is significant in saturation.

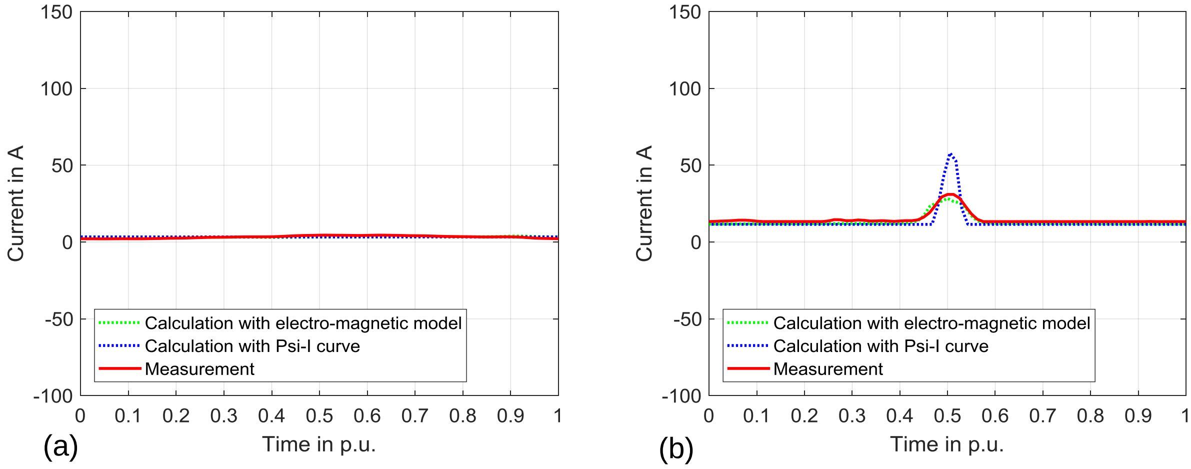

Figure 57: Exciting current in one phase of a three-phase transformer with a T3 core determined by different methods with (a) 3.33 A DC per phase and (b) 13.33 A DC per phase

Figure 56 and Figure 57 show that also the easy methods based on the Ψ-I curve are adequate to determine the wave form of the exciting current if the required transformer parameters of Table 21 are known. However, such easy methods are only possible for single-phase transformers and three-phase units with a T3 core design.

For transformers with a T5 core is an electro-magnetic network required. Furthermore must be noted, that the demonstrated electro-magnetic models for the different transformer types are the basis for more complex simulations like the loss distribution in structural components of a transformer as shown in chapter 5.1.2. Therefore the electro-magnetic modeling approach is fundamental in order to study GIC effects in power transformers.

4.7 Summary

This chapter demonstrated a detailed design-specific modeling technique to calculate the transformer exciting current when additional DC currents are present in the high-voltage winding. For that reason different electro-magnetic network structures and the calculation of the needed magnetic resistances were demonstrated for a set of transformer designs. These electro-magnetic networks models are fundamental, because they are the basis for more complex simulations. In order to verify these modeling techniques several DC experiments with different core designs were done in a high-voltage laboratory. The comparison between the simulations and the measurements showed a good correlation and confirms the discussed modeling techniques.

By the help of the developed calculation models, the behavior of different power transformers with additional DC excitations has been investigated. The outcomes of these studies were used to derive an alternative calculation method for the exciting current under DC. In that way only some basic transformer parameters are needed, and the calculation can be done with a simple calculation tool like MS Excel. The saturation inductance of the excited winding and the DC zero-sequence inductance have been identified as major parameters. The discussed DC test circuits can be used to verify the transformer behavior with an additional DC current in a winding.

It must be noted that DC experiments lead to high peaks in the winding currents and in further consequence this may cause fluctuations in the applied voltage. Such down-turns in the applied voltage must be considered in the simulation of the transformer behavior under DC. This may be also important when the influence of GIC storms on power grids is studied. This means, a transformer model which should simulate DC effects must be able to consider different voltage wave forms. Only with this property is an accurate simulation of the transformer behavior under DC possible.

5 Hotspot calculation

5.1 Thermal model for tie bars

Literature [41], [42] and [43] demonstrate that tie bars near the core are significant stressed components in power transformers in case of additional DC currents in the high-voltage winding. For that purpose a model to calculate the hotspot temperature of such parts is demonstrated in this chapter. It must be noted that the denotation “tie bar” is not used in each literature. Flitch plates or tie rods are other potential names for these elements. However, these denotations describe always the structural steel components in a power transformer which are required for the mechanical clamping of the active part (core and winding block). Figure 58 shows a sketch of a transformer with a T1 Core-Type, together with the clamping structure and a tie bar on the main limb.

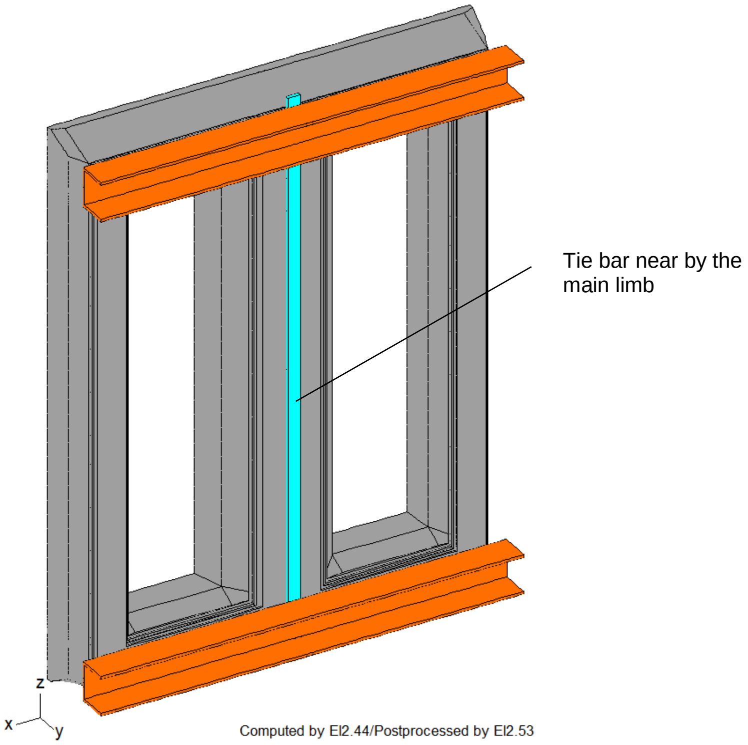
Tie bar near by the main limb
z
x
y
Computed by El2.44/Postprocessed by El2.53

Figure 58: Sketch of a T1 Core-Type with a tie bar on the main limb (half model)

5.1.1 Model approach

The model approach assumes that the tie bars are a heat source with a well-defined axial oil duct in the transformer tank. Figure 59 shows a sketch of the thermal model with the resulting temperature distribution at the tie bar. Four different temperatures are demonstrated in the figure. The bottom and top oil temperature in the transformer tank ($T_{top,oil}$, $T_{bot,oil}$), the local oil temperature in the oil duct of the tie bar (T_{om}) and the local temperature of the tie bar surface itself (T_{src}). The surface temperature of the tie bar is given by the sum of the local oil temperature in the duct plus the local temperature gradient between surface and oil at this position ($g_{src-oil}$). To calculate the local oil temperature in the oil duct the longitudinal oil temperature gradient up the position of interest (D_{oil}) has to be added to the bottom oil temperature of the transformer tank.

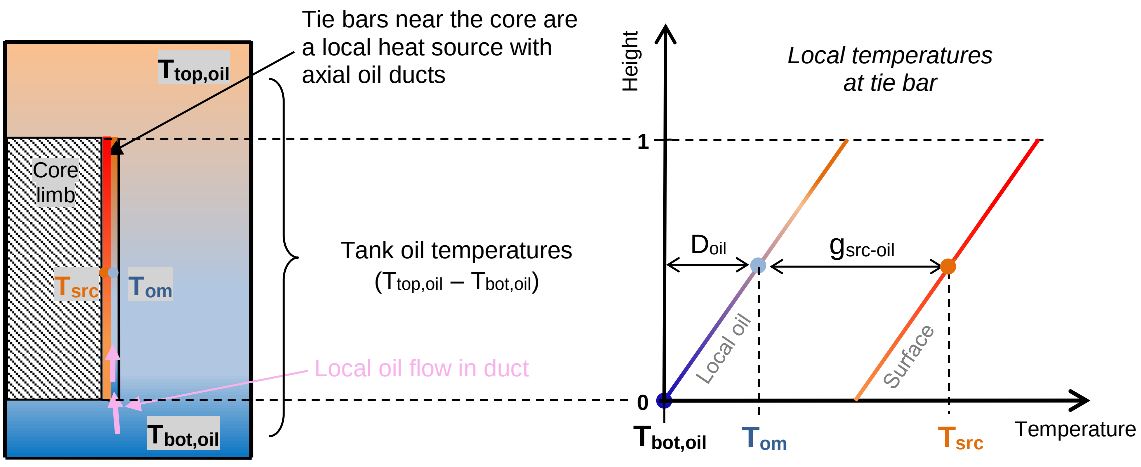
$T_{top,oil}$
Core limb
T_{src}
T_{om}
$T_{bot,oil}$
Tie bars near the core are a local heat source with axial oil ducts
Tank oil temperatures
($T_{top,oil}$ – $T_{bot,oil}$)
Local oil flow in duct
Height
Local temperatures at tie bar
1
D_{oil}
$g_{src\text{-}oil}$
Local oil
Surface
0
$T_{bot,oil}$
T_{om}
T_{src}
Temperature

Figure 59: Simplified temperature model for tie bars near by the core [29]

$$T_{src} = T_{om} + g_{src-oil} \tag{25}$$

$$T_{om} = T_{bot,oil} + D_{oil} \tag{26}$$

To determine the temperatures T_{om} and T_{src} the energy equations (27) and (28) must be solved. The first equation represents the energy balance between the generated, the stored and the dissipated energy of the tie bar. The second energy equation describes the balance between the dissipated energy, the stored energy and the transported energy by the mass flow in the oil duct. Figure 60 demonstrates a sketch of this mechanism. A general discussion of such a modeling technique is shown in [44].

$$Q_{gen,src} = Q_{store,src} + Q_{dis,oil} + Q_{dis,ins} \tag{27}$$

$$Q_{dis,oil} = Q_{store,oil} + Q_{flow} \tag{28}$$

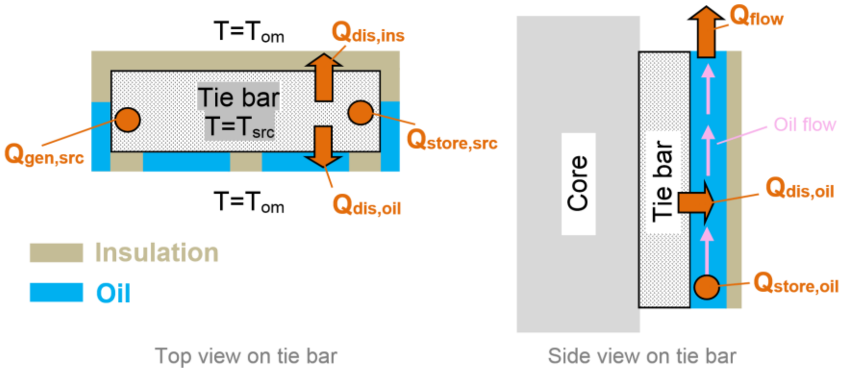
$T=T_{om}$
$Q_{dis,ins}$
Tie bar
$T=T_{src}$
$Q_{gen,src}$
$Q_{store,src}$
$T=T_{om}$
$Q_{dis,oil}$
▨ Insulation
▨ Oil
Top view on tie bar
Q_{flow}
Core
Tie bar
Oil flow
$Q_{dis,oil}$
$Q_{store,oil}$
Side view on tie bar

Figure 60: Energy equations of thermal model

The above-mentioned energy equations can be also expressed by the help of the unknown temperatures T_{om} and T_{src}. This approach leads to a simple differential equation system as shown in (29) and (30).

$$\dot{T}_{src} = -\left(\frac{\alpha \cdot A_{\alpha} + \frac{\lambda \cdot A_{\lambda}}{d_{ins}}}{mc_{src}}\right) \cdot T_{src} + \left(\frac{\alpha \cdot A_{\alpha} + \frac{\lambda \cdot A_{\lambda}}{d_{ins}}}{mc_{src}}\right) \cdot T_{om} + \frac{P_{tot,src}}{mc_{src}} \tag{29}$$

$$\dot{T}_{om} = +\left(\frac{\alpha \cdot A_{\alpha}}{mc_{oil}}\right) \cdot T_{src} - \left(\frac{2 \cdot \dot{m} \cdot c_{p,om} + \alpha \cdot A_{\alpha}}{mc_{oil}}\right) \cdot T_{om} + \frac{2 \cdot \dot{m} \cdot c_{p,om} \cdot T_{bot,oil}}{mc_{oil}} \tag{30}$$

In addition to a few design-specific parameters like the surface in contact with oil (A_α) or the insulation thickness (d_{ins}), some thermal properties must be known in order to solve the equation system. These properties are the heat transfer coefficient (α) and the thermal conductivity of the insulation material (λ). The thermal conductivity is a material property and depends on the used insulation substance. For the heat transfer coefficient, formula (31) can be used, because this parameter depends on the actual heat flux and the actual oil temperature as shown in [45]. The leading coefficient K_α and the exponent x_α in this function are manufacturer-specific values.

$$\alpha = K_\alpha \cdot \left(\frac{P_\alpha}{A_\alpha}\right)^{x_\alpha} \cdot f(T_{om}) \tag{31}$$

The needed mass flow in the model can be determined with formula (32) which is derived from the pressure drop equation of the model. Such pressure drop methods are shown in [46].

$$\dot{m} = \frac{g \cdot \rho_{om} \cdot \beta_{om} \cdot H_{src} \cdot \left(T_{top,oil} + T_{bot,oil} - 2 \cdot T_{om}\right)}{2 \cdot R_{hyd}} \tag{32}$$

The formulas for the thermal model show that three operational values are needed to calculate the transient temperature behavior of the tie bar. Operational values mean input data which change during the transformer operation. These input values are:

- Top oil temperature in the transformer tank
- Bottom oil temperature in the transformer tank
- Losses in the tie bar

As indicated in Figure 18, it becomes clear here, that the top and bottom oil temperature in the transformer tank can be used to consider the operational thermal condition, because these values can be measured easily for an existing transformer. The third input variable is the loss value in the tie bar. However, the losses depend on the actual DC level in the transformer winding and cannot be measured separately. Consequently chapter 5.1.2 discusses a calculation model to determine the losses in the tie bars based on the actual DC level in the transformer winding.

5.1.2 Calculation of tie bar losses

To calculate the losses in the tie bars when additional DC currents are present in the windings of a transformer the electro-magnetic modeling technique of chapter 4.1 is extended. As a first step a simulation with a three-dimensional FEM model was carried out, using methods discussed in [47], [48], [49], [50] and [51]. This was done in order to find a suitable, but a more simplified modeling technique. The design-specific transformer parameter for this investigation are given in Table 22. It is a 230 kV, 60 Hz single-phase transformer with a T1 core design.

Table 22: Design-specific transformer parameters for loss investigation (lengths in the table are in [m], cross sections are in [m²])

Parameter	Value	Parameter	Value	Parameter	Value	Parameter	Value
L_1	2.190	L_6	2.817	L_{11}	0.238	A_Y	0.182
L_2	0.350	L_7	3.240	D_C	0.700	A_{RL}	0.182
L_3	1.055	L_8	-[6]	D_I	1.242	A_S	-[6]
L_4	-[6]	L_9	0.01	D_O	1.484	d_w	0.010
L_5	2.000	L_{10}	0.665	A_C	0.365	N_{turns}	800

---

[6] This parameter is not required for the selected transformer design.

The geometry of the tie bar is illustrated in Figure 61.

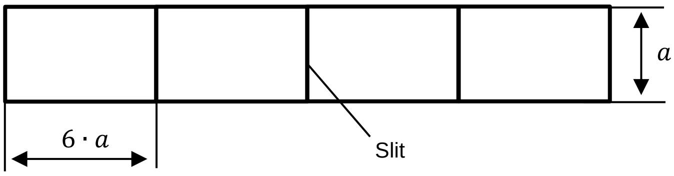

Figure 61: Sketch of tie bar geometry (top view on cross section)

The calculated eddy current distribution with the three-dimensional simulation model is shown in Figure 62 for a single tie bar. It can be seen, that significant eddy currents are flowing in the material which are generated by an axial stray flux which penetrates the material. These eddy currents are the reason for the additional losses in the tie bars during the core saturation. In addition can be seen, that the highest currents flow along the borders of the tie bars and that they are decreasing inside of the material.

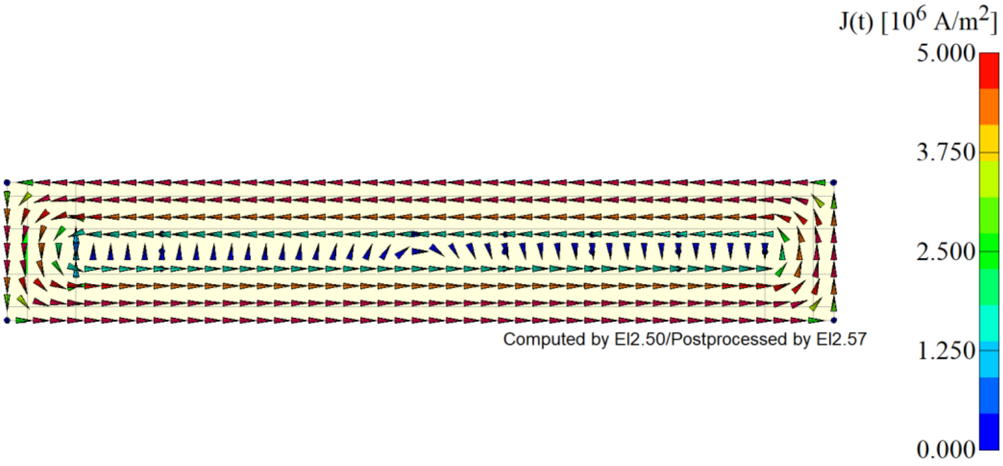

Figure 62: Eddy current distribution in a single tie bar due to core saturation (top view on cross section)

Such eddy currents can be also simulated by the help of a simple electro-magnetic network. For that purpose the tie bars must be modeled as several layers (flux paths) where an eddy current can flow along the circumference. Figure 63 demonstrates the extension of an electro-magnetic model with such tie bar elements, together with the geometry parameters which are needed to calculate the ohmic resistances of the eddy current loops and the magnetic resistances of the flux paths. The equations to calculate these quantities (ohmic and magnetic resistances) are given with the formulas (33) and (34) below.

In principle in each layer is an eddy current possible which is linked with the corresponding magnetic flux in the layer. However, along the height of the core limb are in the tie bar different magnitudes for the eddy current possible. To cover such a potential non-uniform loss distribution over the axial height, several tie bar elements can be placed in parallel to the axial magnetic resistances which represent the core limbs in the electro-magnetic network of the transformer (chapter 4).

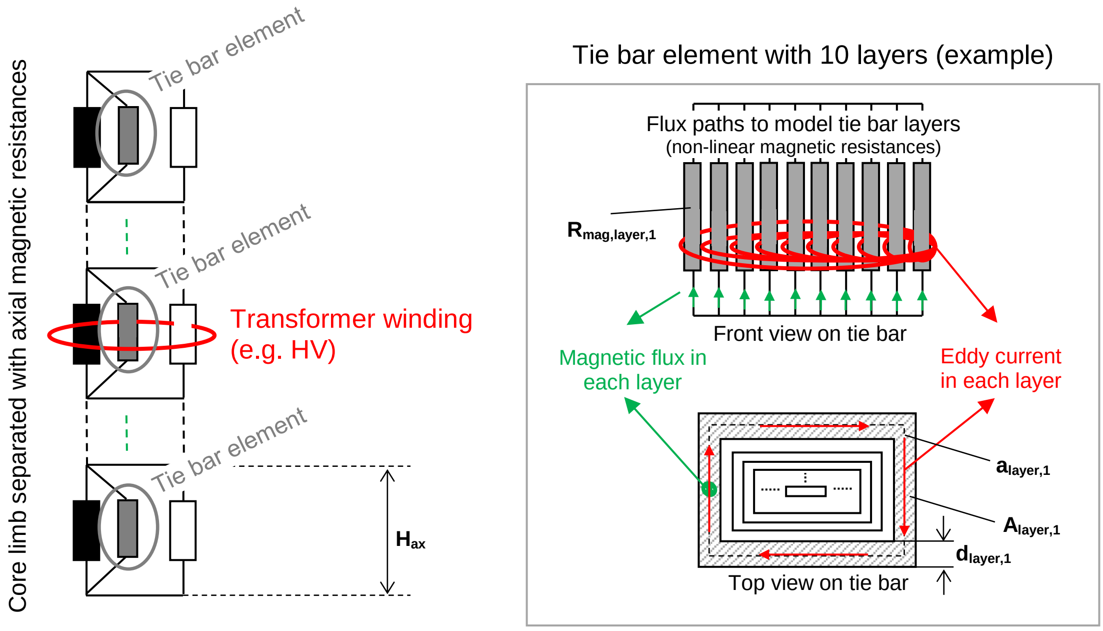
Core limb separated with axial magnetic resistances
Tie bar element
Tie bar element
Tie bar element
Transformer winding
(e.g. HV)
H_ax
Tie bar element with 10 layers (example)
Flux paths to model tie bar layers
(non-linear magnetic resistances)
R_mag,layer,1
Front view on tie bar
Magnetic flux in each layer
Eddy current in each layer
a_layer,1
A_layer,1
d_layer,1
Top view on tie bar

Figure 63: Extension of an electro-magnetic network with tie bar elements

5.1.2.1 Parameter for an electro-magnetic tie bar model

To build an electro-magnetic model of a tie bar the ohmic resistance of each eddy current turn i and the magnetic resistance of each layer i (flux paths) must be known. These parameters can be calculated with the geometry of the tie bar and the electrical conductivity κ of the used material. They are given with:

$$R_{\mathrm{ohm,eddy,i}} = \frac{a_{\mathrm{layer,i}}}{\kappa \cdot H_{ax} \cdot d_{\mathrm{layer,i}}} \tag{33}$$

$$R_{\mathrm{mag,layer,i}} = \frac{H_{ax}}{\mu_0 \cdot A_{\mathrm{layer,i}}} \cdot \frac{1}{\mu_r\left(B_{\mathrm{layer,i}}, H_{\mathrm{layer,i}}\right)} \tag{34}$$

It must be noted, that the magnetic resistances of the tie bar layers (flux paths) are variable. Consequently, the B-H curve of the material must be known to complete the equation system.

5.1.2.2 Behavior of an electro-magnetic tie bar model

Figure 64 demonstrates calculation results of the discussed tie bar model when the saturation level in the core limb of the transformer is exceeded. A DC current of 5 A was applied in addition to the nominal AC voltage. The tie bar which is demonstrated in Figure 61 is divided into 10 layers and the required parameters are calculated according to formula (33) and (34). In addition to the DC fluxes significant AC flux components in the tie bar layers can be seen during the saturation period. These flux changes over the time generate the eddy currents in the material. The highest eddy current flows in the outmost layer and for deeper layers the magnitudes are decreasing. This means that the calculation result of the simple electro-magnetic tie bar model shows the same trend as the FEM results in Figure 62. In order to calculate the losses generated by these eddy currents, the RMS values of the currents must be squared and multiplied with the ohmic resistances of the corresponding layers.

$$P_{\mathrm{eddy,i}} = {I_{\mathrm{eddy,RMS,i}}}^2 \cdot R_{\mathrm{eddy,i}} \tag{35}$$

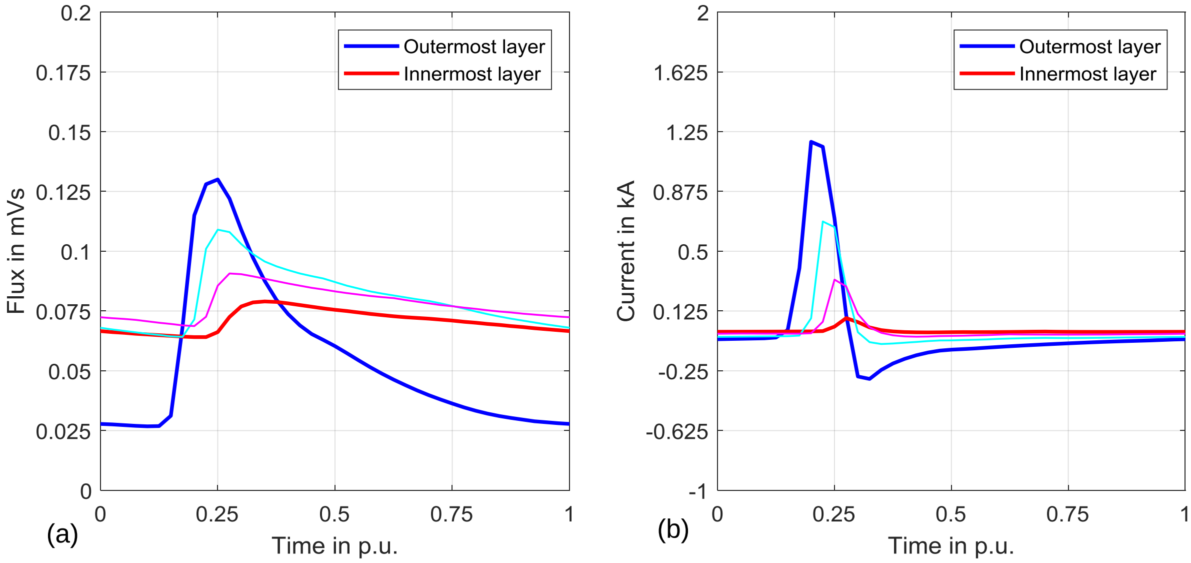

Figure 64: (a) Calculated magnetic flux and (b) Eddy currents in different tie bar layers

5.1.3 Consideration of inhomogeneous loss distribution

Figure 63 in this thesis has demonstrated that the losses over the axial height can differ in a tie bar, because several axial elements can be modeled. Such a potential inhomogeneous loss distribution has to be also taken into account in the temperature calculation, because the temperature sketch of Figure 59 is valid for a constant loss density along the axial height of the tie bar. However, a loss distribution can be easily taken into account by the help of loss density factors ($K_{loss,center}$, $K_{loss,top}$). Such factors represent the ratios between the local loss densities at a certain position to the average loss density. Figure 65 explains the calculation of these factors.

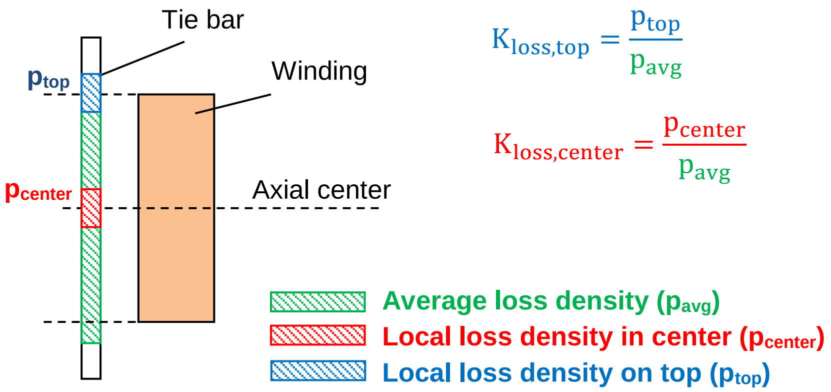
Tie bar
Winding
p_{top}
p_{center}
Axial center
$K_{loss,top} = \frac{p_{top}}{p_{avg}}$
$K_{loss,center} = \frac{p_{center}}{p_{avg}}$
Average loss density (p_{avg})
Local loss density in center (p_{center})
Local loss density on top (p_{top})

Figure 65: Non-uniform loss distribution in tie bar along the height

In order to calculate the surface temperature at a certain position of the tie bar, the local temperature gradient between surface and oil must be multiplied by this loss density factor as shown in equation (36) and (37).

$$T_{center} = T_{om} + g_{src-oil} \cdot K_{center} \tag{36}$$

$$T_{top} = T_{om} + (T_{om} - T_{bot}) + \; g_{src-oil} \cdot K_{top} \tag{37}$$

5.1.4 Analysis

By the help of the discussed loss calculation and the demonstrated thermal model, the behavior of two different tie bar designs over a wide range of DC is studied for a power transformer. Table 23 shows the geometry of these tie bar arrangements.

Table 23: Different tie bar designs under investigation

Tie bar parameter	**Width**	**Thickness**	**Slits**	**Cooled Surface**
-	**mm**	**mm**	**-**	**-**
Design 1	$4{,}9 \cdot a$	$4{,}9 \cdot a$	0	15 %
Design 2	$24 \cdot a$	a	3	40 %

The effect of variations in the tie bar design on the hotspot temperature under DC is demonstrated in Figure 66. On the top of the figure the total losses per kilogram for both designs are compared. Both configurations show a non-linear behavior, but the loss increase of Design 1 is higher than the increase of Design 2. This loss behavior in combination with the cooling arrangement of the tie bar affects also the behavior of the hotspot temperature as demonstrated in the bottom part of the figure. Design 1 shows an extremely high temperature rise of about 200 K above the bottom oil temperature with 100 A DC per phase, whereas Design 2 reaches only a moderate temperature rise in the range of 80 K at the same DC level. The bottom oil temperature is for all calculations 40 °C.

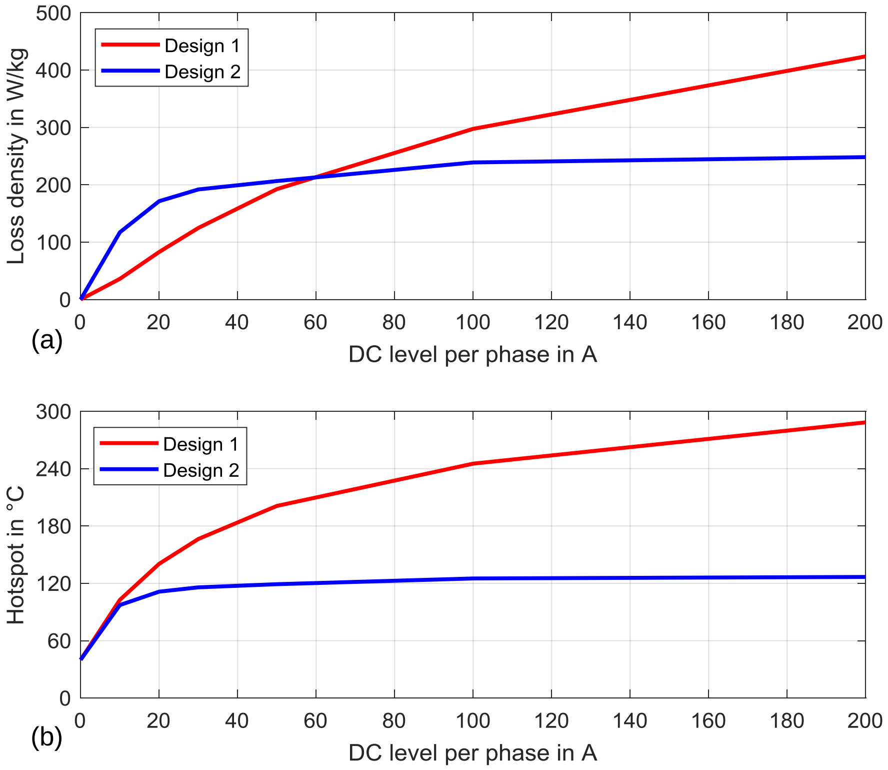

Figure 66: Influence of tie bar design on (a) Loss density and (b) Hotspot temperature under DC

Furthermore must be noted that not only the DC level alone determines the temperature rise of the tie bar above the bottom oil. Also the oil temperature level in the tank itself has an influence on the hotspot rise of the tie bar. Figure 67 shows the hotspot temperature rise above the bottom oil for different bottom oil temperatures. The DC level is for each calculation 50 A DC per phase in this figure. It can be seen, that the tie bar hotspot temperature rise decreases with higher oil temperatures in the tank. The reason is the viscosity of the oil which influences thermal parameters like the heat transfer coefficient and the hydraulic resistance.

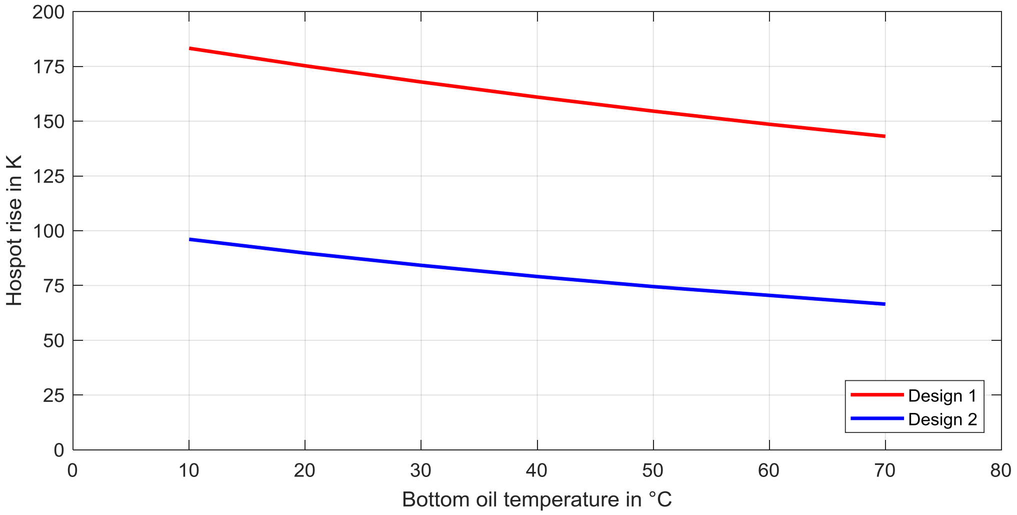

Figure 67: Influence of tank oil temperature on hotspot rise of tie bar above tank bottom oil (DC per phase = 50 A)

5.2 *Verification*

5.2.1 Experimental setup

Temperature and flux measurements during a DC experiment with a single-phase transformer were done in order to verify the demonstrated modeling techniques for the loss and temperature behavior of tie bars. At the one hand flux measuring loops were implemented during the manufacturing to confirm the loss calculation, because as discussed before the losses under DC are caused by eddy currents due to the additional magnetic flux in the tie bar. At the other hand temperature sensors were installed to compare the calculated temperatures with the measured once. In that way the validity of the thermal model can be demonstrated. Figure 68 demonstrates the positions of the installed temperature sensors and of the flux measuring loops in a tested transformer. It can be seen, that measurements in the axial center of the tie bar as well as in the height of the axial winding end were done. The used test circuit for this experiment is discussed in chapter 4.4.1 (Figure 38).

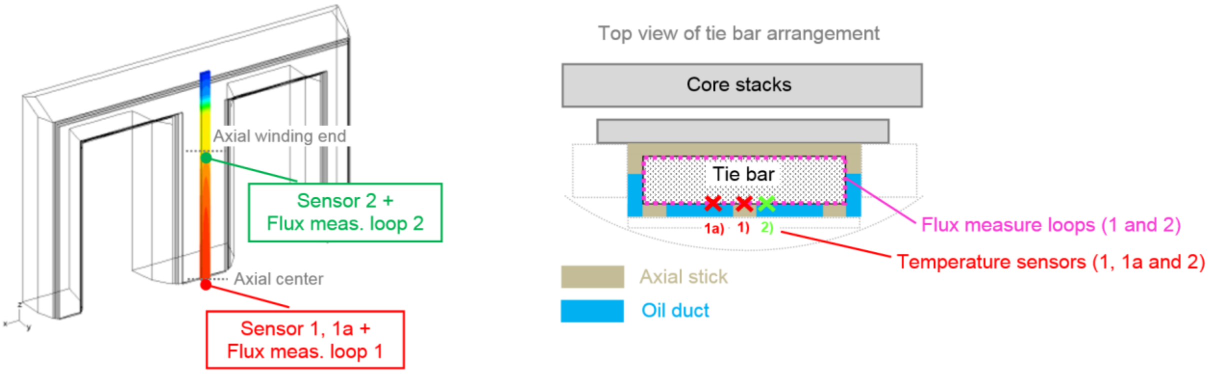
Axial winding end
Sensor 2 +
Flux meas. loop 2
Axial center
Sensor 1, 1a +
Flux meas. loop 1
Top view of tie bar arrangement
Core stacks
Tie bar
1a)
1)
2)
Flux measure loops (1 and 2)
Temperature sensors (1, 1a and 2)
Axial stick
Oil duct

Figure 68: Location of temperature sensors and flux measure loops (Hotspot test no. 1)

5.2.2 Test results vs. simulation (Hotspot Test no. 1)

5.2.2.1 Comparison of magnetic flux in tie bar

Figure 69 compares selected measured AC fluxes in the tie bar with the calculated ones using the simulation technique of chapter 5.1.2. The left side of the figure shows the magnetic fluxes in the axial center and the right part the fluxes on the top of the tie bar in the height of the axial winding end. It can be seen, that the measured wave forms of the magnetic fluxes correlate well with the calculated ones.[7] In order to investigate the behavior over all injected DC currents the RMS values of the fluxes over the DC range are illustrated in Figure 70. This figure shows also the good correlation between measurement and simulation and that the deviations of the RMS values are in an acceptable range. This indicates a correct modeling of the tie bar arrangement and a reliable loss calculation according to chapter 5.1.2.

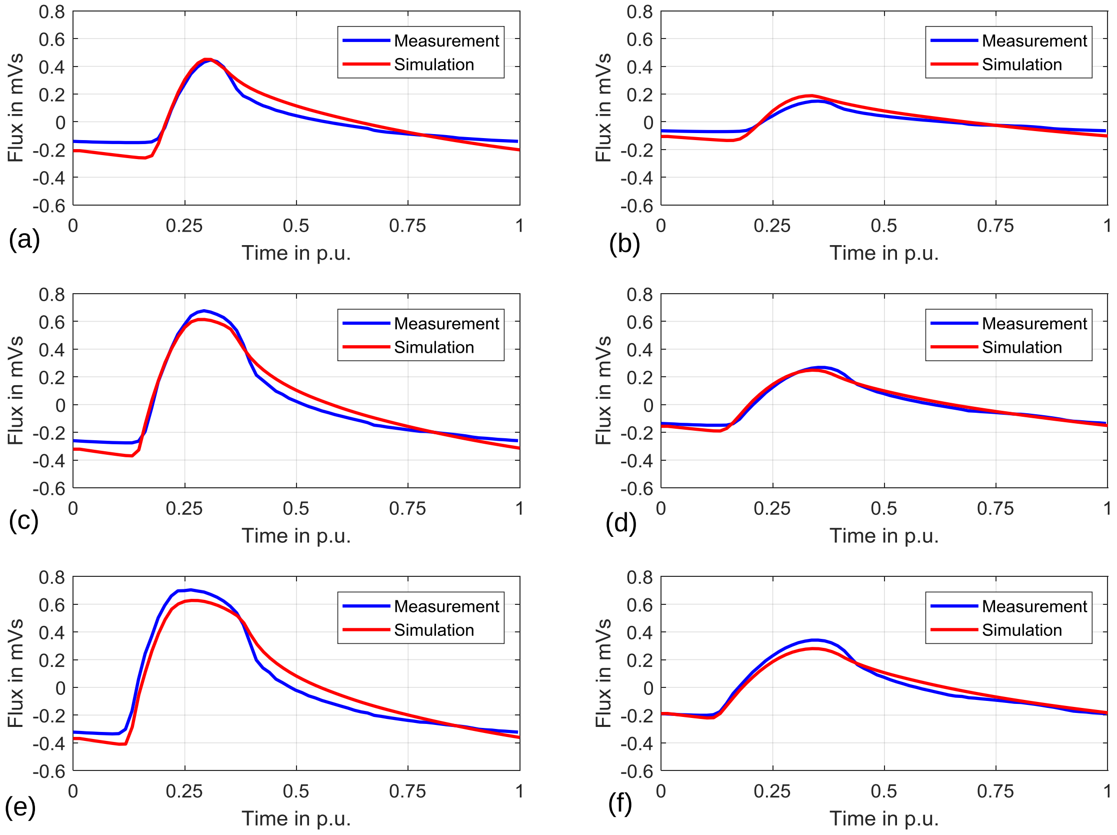

Figure 69: Comparison of AC flux in the tie bar – 10 A DC per phase at (a) Center position and (b) Top position, 30 A DC per phase at (c) Center position and (d) Top position, 50 A DC per phase at (e) Center position and (f) Top position

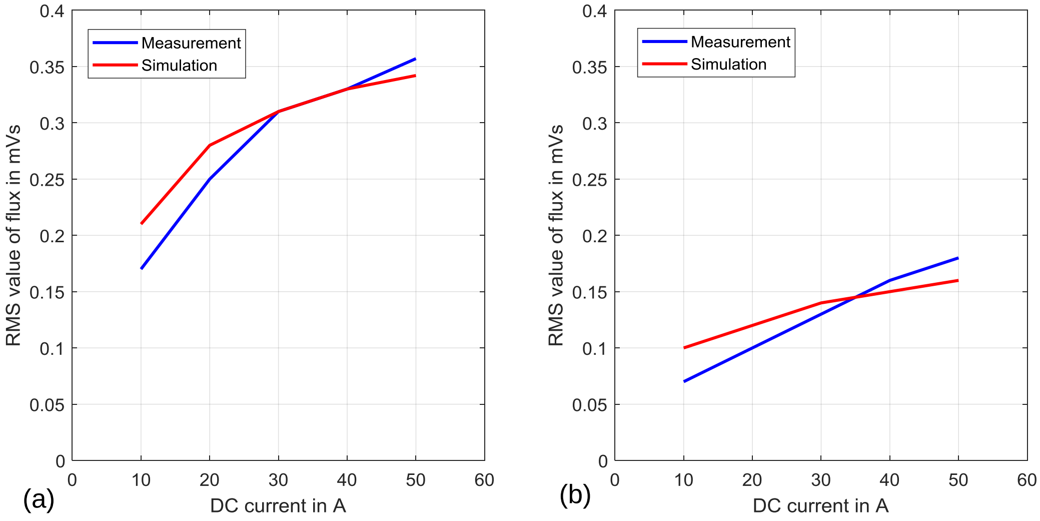

Figure 70: Comparison of the RMS value of the tie bar flux over complete DC range: (a) Center position, (b) Top position

---

[7] It must be noted that the measured voltage must be used for the simulations as already discussed in chapter 4.4.1.2 of this thesis.

5.2.2.2 Calculated tie bar losses during DC experiment

Figure 71 demonstrates the calculated behavior of the tie bar losses over the measured DC levels. As mentioned before, for this simulation it is important to consider the real wave form of the applied voltage during the DC experiment as discussed in chapter 4.4.1.2. The increase of the total losses with the DC level and the loss density distribution over the axial height are captured in the graphic. It can be seen, that the total losses increase non-linear with the DC level and that the loss density in the axial center is higher than the loss density in the height of the axial winding end. With 50 A DC per phase in the high-voltage winding the loss density in the axial center of the tie bar is about 118 % compared to the average loss density over the complete height. On the top in height of the axial winding end the situation is different. Here the local loss density is only about 70 % of the average value.

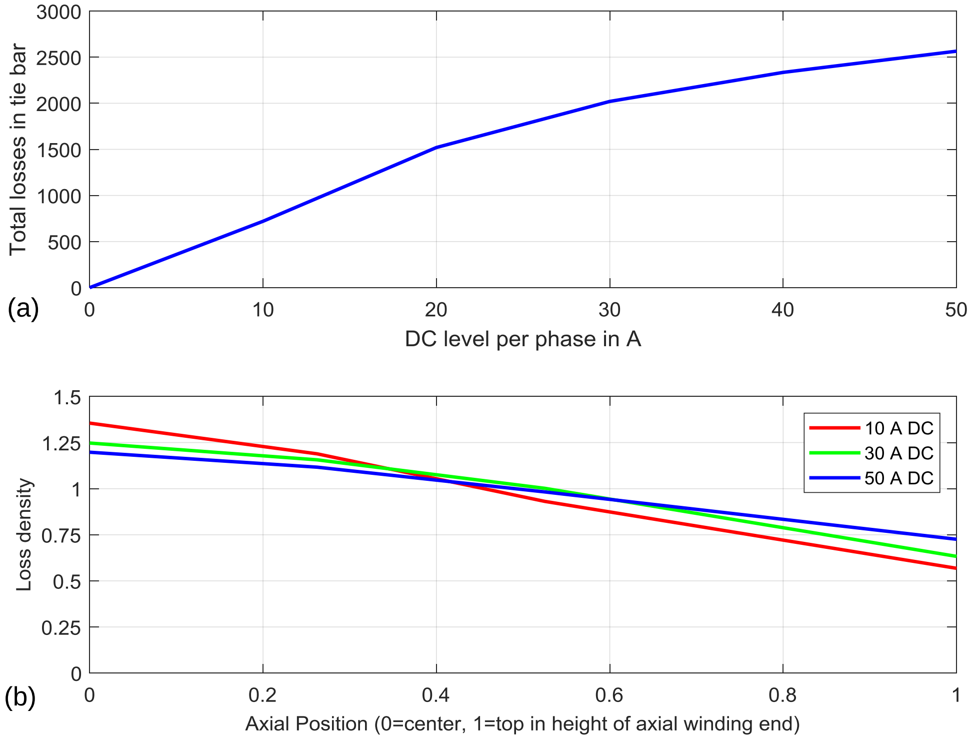

Figure 71: Calculated tie bar losses with the applied voltage during the DC experiment – (a) Increase of total losses with the DC level, (b) Loss distribution over the axial height

5.2.2.3 Comparison of tie bar temperatures

By the help of the demonstrated loss data, the transient temperature behavior of the tie bar for the injected DC profile during the experiment was simulated with the thermal model of chapter 5.1.1. Figure 72 compares the calculated temperatures with the measurement results. It becomes apparent that the measured hotspot in the center of the tie bar (Sensor 1) correlates very well with the simulation. The maximal deviations are in the range of 3 K. The simulation of the top hotspot sensor (Sensor 2) results values slightly higher than the measurement. The deviations are approximately 10 K. Nevertheless, the simulated transient thermal behavior of Sensor 2 is also acceptable because the calculated values are consistently higher. Potential explanations for these deviations are discussed in [29].

In addition to Sensor 1 and Sensor 2, a local oil temperature sensor was installed in the tested transformer, located in the oil duct and in close vicinity to Sensor 2. It should be noted, that the results of such local oil measurements should be used with caution. Nevertheless, Figure 72 demonstrates that the model also simulates the behavior of the local oil sensor accurately. Overall the comparison of the simulation results with the measurements indicates a suitable thermal model to simulate the transient temperature behavior of the tie bar. Table 24 summarizes the measured temperatures at the end of each DC level (steady-state temperature rises above the bottom oil) together with the deviations to the calculation results.

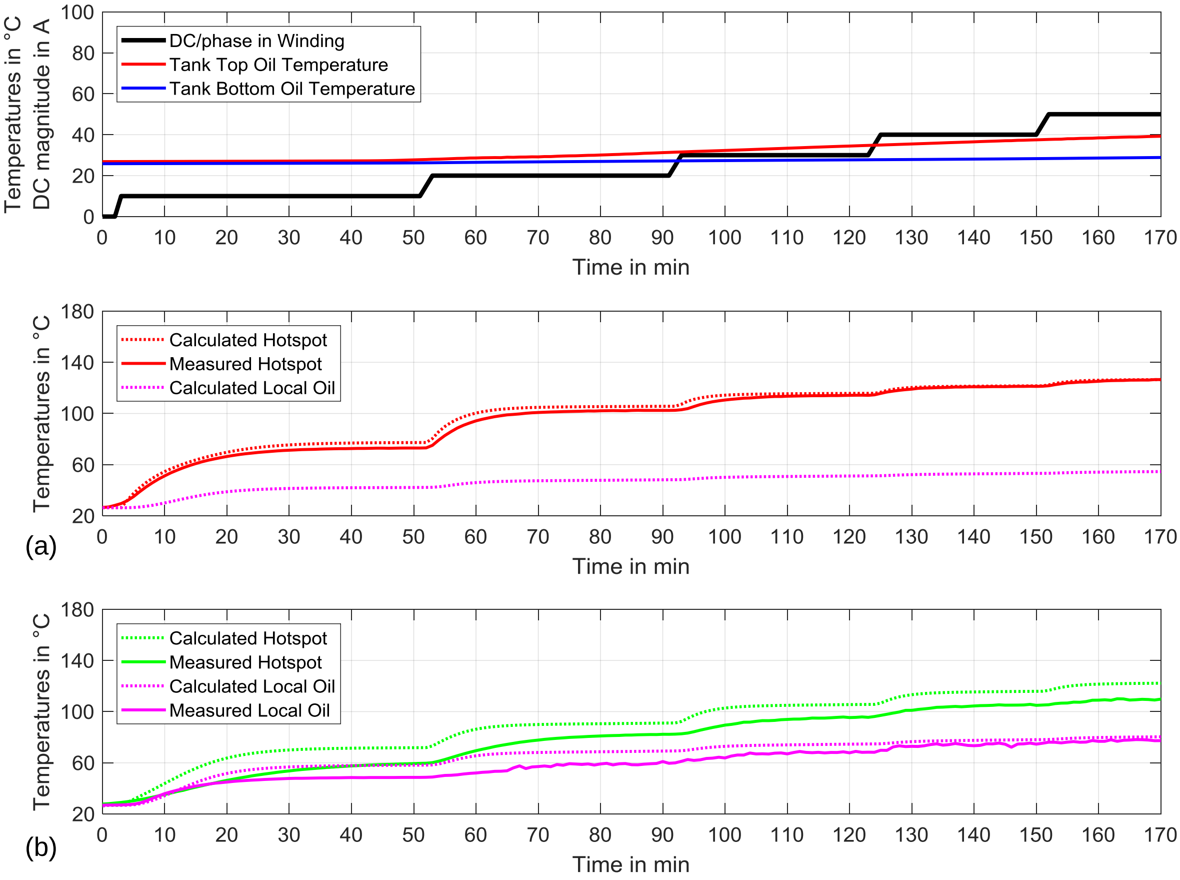

Figure 72: Comparison of (a) Center and (b) Top tie bar temperatures (measurement vs. simulation) [29]

Table 24: Temperatures at steady-state conditions (Hotspot Test no. 1)

DC current	**Sensor 1 (center)**		**Sensor 2 (top)**		**Local oil sensor (top)**		**Bottom oil**
-	Measured value	Deviation	Measured value	Deviation	Measured value	Deviation	Measured value
	°C	K	°C	K	°C	K	°C
10 A DC	73	+2	60	+12	49	+7	26
20 A DC	102	+2	82	+10	61	+6	27
30 A DC	114	+1	96	+10	68	+3	28
40 A DC	121	+1	105	+10	75	+0	28
50 A DC	127	0	110	+11	77	-1	29

5.2.3 Influence of voltage wave form on temperature

As already discussed, the wave form of the applied voltage has an influence on the transformer behavior under DC. Chapter 4.4.1 showed that DC currents in the high-voltage winding may cause down-turns in the applied voltage. It could be shown, that such fluctuations in the voltage provoke at the same DC level lower exciting current peaks compared to conditions with pure sinusoidal voltages. However, not only the exciting current is affected. Figure 74 below shows that also the losses in the tie bar and in further consequence their temperatures are influenced by the voltage wave form.

A measure for the voltage distortion is the total harmonic distortion (THD) of the wave form. This value describes the ratio between the summarized power of the harmonics to the power of the fundamental. The THD value is given with:

$$\mathrm{THD} = \frac{\mathrm{U_2}^2 + \mathrm{U_3}^2 + \cdots + \mathrm{U_n}^2}{\mathrm{U_1}^2} \tag{38}$$

An example for a distorted voltage during a DC experiment and the frequency spectrum is demonstrated in Figure 73. The odd harmonics show significant magnitudes. As a result the THD value of the signal is 9.9 %.

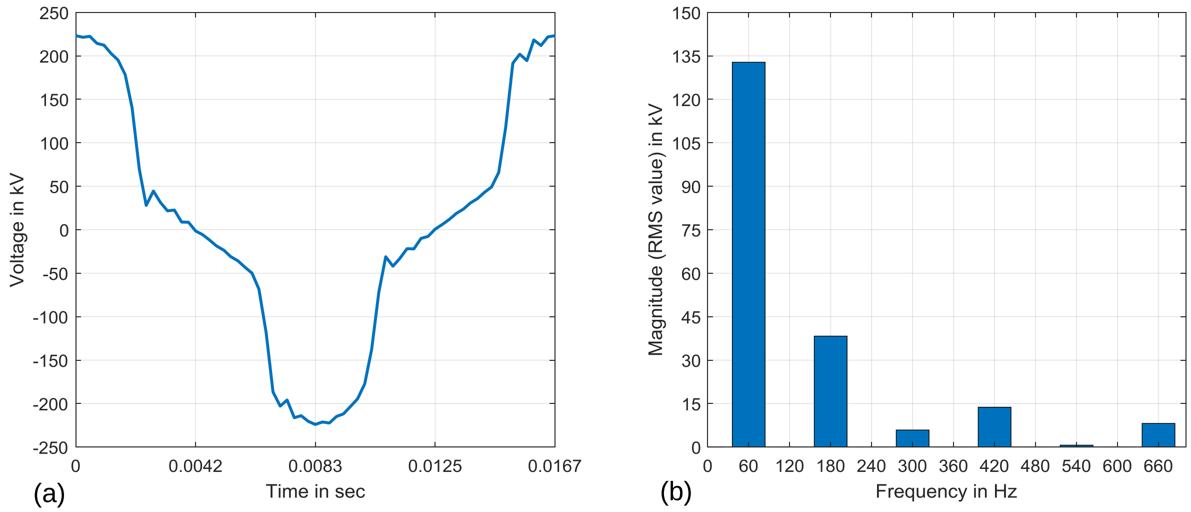

Figure 73: Distorted applied voltage during a DC experiment: (a) Wave form and (b) Frequency spectrum with a THD of 9.9 %

Figure 74 demonstrates the influence of such distorted voltages which occur during laboratory tests on the tie bar temperature. For that purpose the THD values of the measured voltages for each tested DC level is shown in Figure 74a. It can be seen, that the harmonics in the applied voltage increases with the DC level. The reason is the internal voltage drop over the impedance of the test lab generator during the high peak of the exciting current. This means that a larger generator causes smaller harmonics in the voltage compared to a weaker one where the same DC level is tested. Consequently, a strong generator is essential to make DC experiments in test laboratories.

In order to illustrate the influence of such voltage fluctuations, the results of two different simulations are also compared with each other in the figure. One simulation set is done with the distorted voltages during the measurements (red lines), and a second simulation set is carried out with a pure sinusoidal voltage (blue lines). It can be seen from the figure, that different voltage wave forms lead, at the same DC level, to different tie bar losses. Consequently also the hotspot temperatures are different between both cases. With 10 A DC per phase the THD of the measured voltage is about 2 % what lead to a difference of about 14 K in the hotspot temperature. With 50 A DC per phase the THD of the voltage is already 10 % and this causes a temperature difference of about 28 K in the simulation. This observation is also important when the temperature behavior during a GIC storm is evaluated. If voltage fluctuations are present during GIC events, then the temperatures in the transformers may be automatically damped compared to the worst-case condition with a pure sinusoidal applied voltage.

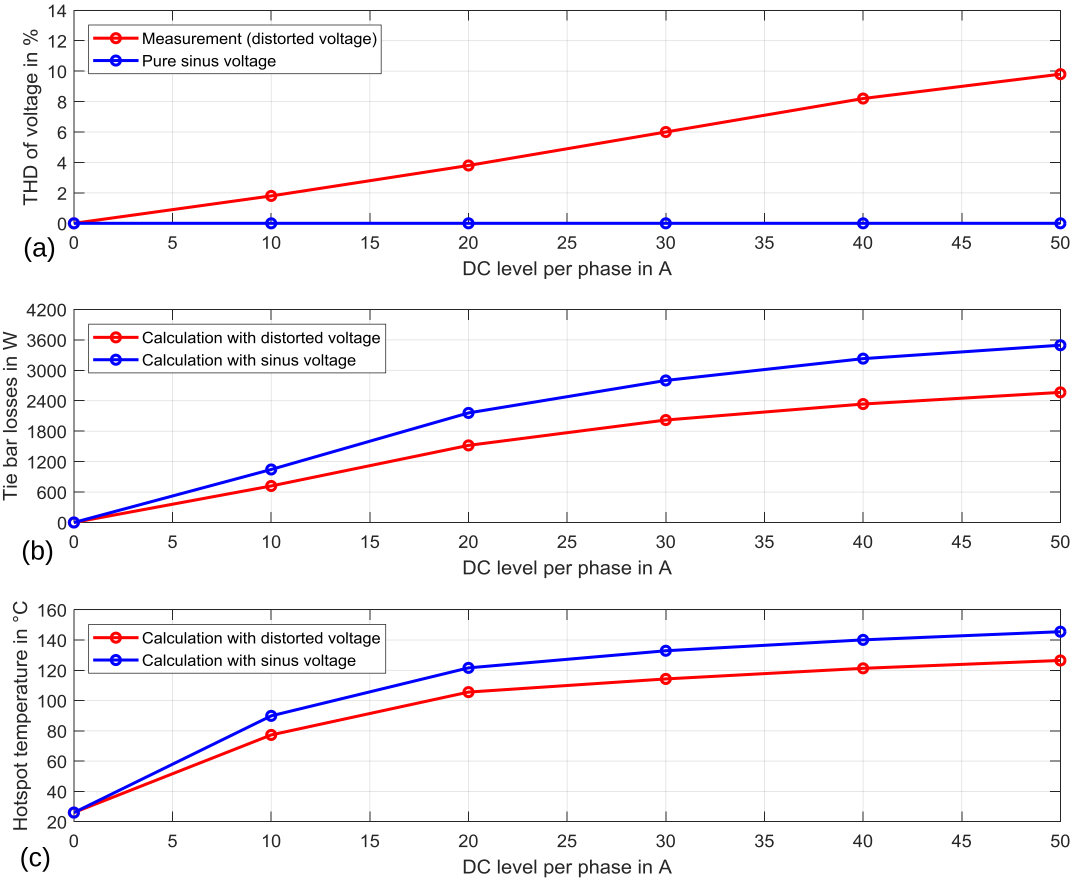

Figure 74: Influence of voltage wave form on hotspot temperature: (a) THD of applied voltage, (b) Tie bar losses and (c) Hotspot temperature

5.2.4 Further DC experiments to verify the hotspot calculation

To ensure the validity of the temperature calculation for the tie bars under core saturation further DC experiments with extra temperature sensors in different transformers were carried out. Table 25 shows the main technical data of these units. In addition the transformer data of Hotspot Test no. 1 is shown in the table.

Table 25: Overview of DC tested power transformers

Transformer	**Core-Type**	**Rated voltage with nominal core flux density**	**Power**	**Typ**	**Maximal tested DC level**
Unit 1	T1	230/√3 kV (1.71 T)	133 MVA	Auto	50 A DC/phase
Unit 2	T4	405/√3 kV (1.69 T)	570 MVA	GSU	25 A DC/phase
Unit 3	T5	420 kV (1.72 T)	200 MVA	Auto	3.9 A DC/phase
Unit 4	T1	500/√3 kV (1.45 T)	117 MVA	SVC	16.6 A DC/phase
Unit 5	T5	345 kV (1.59 T)	575 MVA	PST	33.3 A DC/phase
Unit 5a	T5	345 kV (1.59 T)	575 MVA	PST	50 A DC/phase

At each of the tested power transformers a DC profile was injected into the high-voltage winding, similar as it is was done in the discussed test of Figure 72. However, it must be noted that the maximal testable DC level in the test laboratory depends on the power of the generator and the reactive power consumption of the test circuit. This explains the fact that not each transformer of Table 25 was tested up to 50 A DC per phase.

Figure 75 illustrates an injected DC profile into the high-voltage winding of Unit 2 and the comparison of the measured hotspot temperature by a thermo-couple sensor with the calculated temperature using the thermal model of chapter 5.1. Unfortunately there is a lack of sensor data at the beginning of the test due to a malfunction of the measuring device. Nevertheless, the data starts early enough to see the difference at the end of the 5 A DC period. The measured temperature values in the steady-state conditions and the deviations to the calculation results are listed in Table 26.

Such an analysis was done for each hotspot test. The results of these comparisons are illustrated in Appendix C and the analysis of the data is discussed in chapter 5.2.5 below.

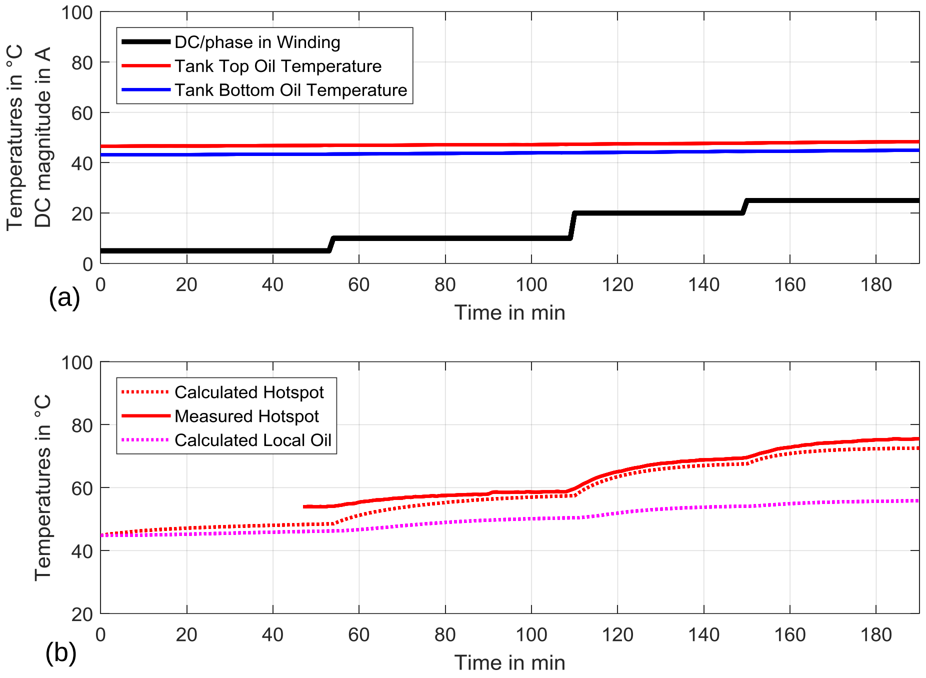

Figure 75: Hotspot test at Unit 2: (a) Injected DC profile and (b) Resulting temperatures

Table 26: Temperatures at steady-state conditions at Unit 2

DC current	**Hotspot sensor**		**Bottom oil**
-	Measured value	Deviation	Measured value
	°C	K	°C
5 A DC	54	-6	43
10 A DC	59	-2	44
20 A DC	69	-2	44
25 A DC	76	-3	45
Average deviation during whole test period: -4.3 K			

5.2.5 Analysis

5.2.5.1 Statistic – measured vs. calculated hotspot temperature

This chapter analyzes the accuracy of the applied hotspot model for tie bars under core saturation. In total the tie bar hotspot temperature of five different transformer designs was measured with different DC levels in the high-voltage windings.

Figure 76 compares the measured steady-state hotspot temperature rises above the bottom oil temperatures with the calculated ones[8]. The graphic demonstrates that the calculations correlate well with the measurements. It must be noted, that only the design data are changed in order to simulate the temperatures for the different transformers. Thermal model parameters like the function for the heat transfer coefficient are fixed for all calculations. Consequently, the demonstrated temperature model in this thesis is a suitable approach to calculate the temperatures of tie bars under core saturation. Some statistical values about the comparison of the measurement data with the simulation results are given in Table 27 below.

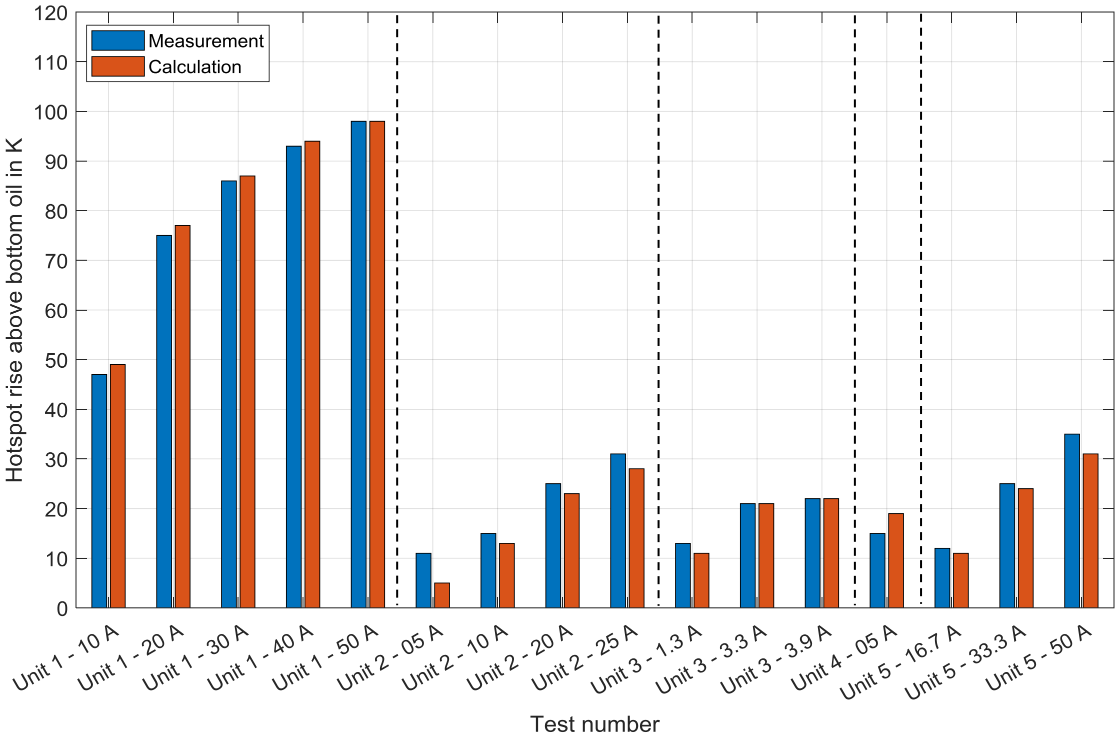

Figure 76: Tie bar hotspot rise in different transformers (measurement vs. calculation)

Table 27: Hotspot statistic – Measurement vs. Calculation

Maximal deviation	-4.3 K
Average deviation	0.1 K

5.2.5.2 Resume

A simple method to evaluate the DC capability of a transformer would be very helpful for power utilities in order to evaluate the risk for a specific a solar storm. For such an evaluation is the DC-caused hotspot temperature rise essential. The demonstrated calculation model for the hotspot temperature of tie bars can be used to answer this question. However, the discussed calculation model uses some design-specific parameters of the transformer and this required information is not always known. Consequently, a more generic hotspot determination would be also of interest.

However, an estimation of the tie bar temperature only with the DC level is not realistic. This becomes obvious by an analysis of the measurement data. Figure 77 shows the measured tie bar hotspot rises above the bottom oil temperature for each tested DC level at different transformers. Significant differences can be seen between the units. With a DC level of e.g.

---

[8] The x-axis indicates the tested unit with the DC level. E.g. Unit 1-10 A means: Hotspot test at Unit 1 with 10 A DC per phase.

50 A per phase the measurement data of Unit 1 shows a temperature rise of almost 100 K whereas Unit 5 shows a hotspot rise of only about 35 K at the same DC level. Another example is when Unit 2 is compared with Unit 3. Unit 3 needs only 4 A DC per phase to reach 20 K temperature rise whereas Unit 2 needs about 20 A DC to reach the same hotspot rise.

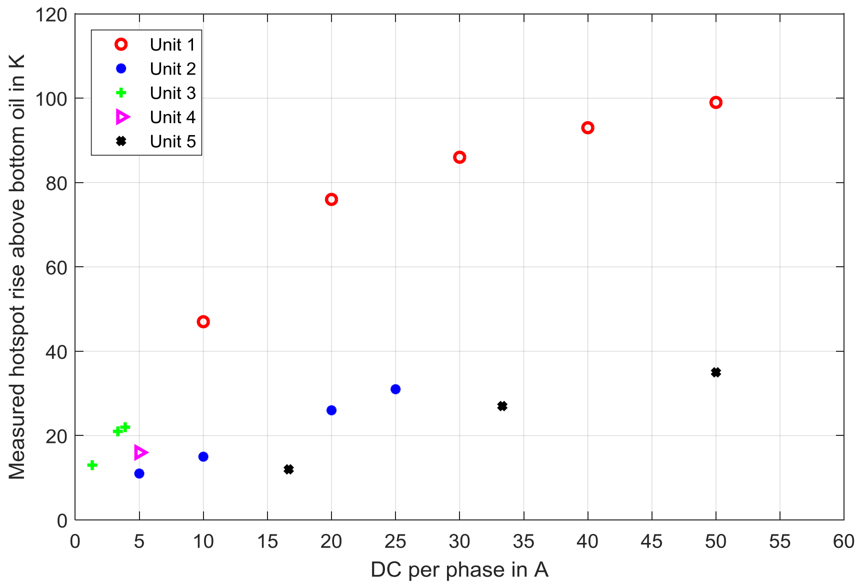

Figure 77: Measured tie bar hotspot rises at different DC levels in different transformers

However to pursue the aim of an estimation method for the tie bar hotspot under DC, Figure 78 illustrates again the measured hotspot rises of this thesis, but the x-axis captures now the calculated peak flux density in the core limb for each measurement point. This approach is more reasonable than the first one which uses only the DC level, because the flux density is really a measure for the saturation condition of the transformer. Therefore the measured hotspot rises follow a trend over the peak flux density. That means that at least the maximal flux density in the core limb must be known to estimate the corresponding hotspot rise. However, a potential design influence of the tie bar itself is not covered in such estimations and therefore the error range of such curves is high. As shown in chapter 5.1.4 before, a different tie bar design can result in significant other temperature rises. Therefore only the transformer manufacturers can make a reliable determination of the DC withstand capability by the help of a design-specific and measurement-proofed calculation model as it is demonstrated in this thesis.

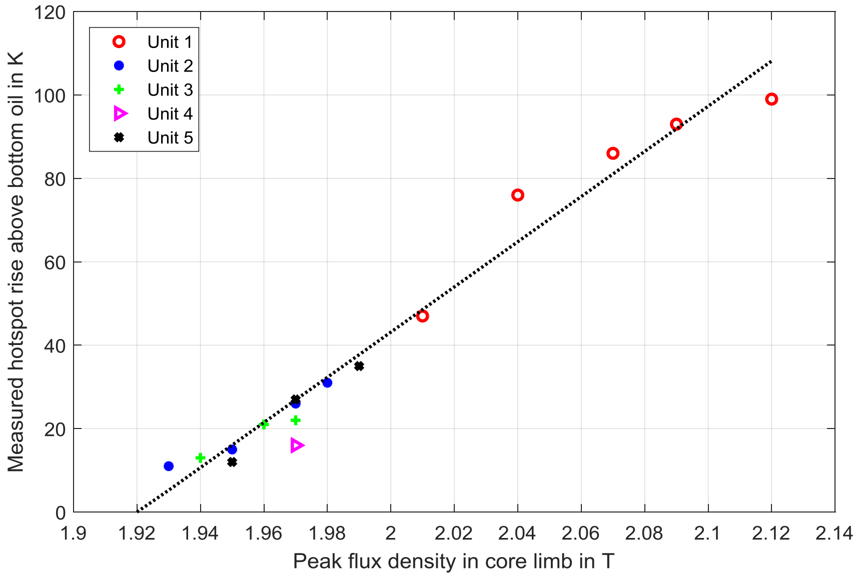

Figure 78: Estimation of tie bar hotspot rise based on peak flux density in core main limb

5.3 Summary

This chapter demonstrated a method to simulate the hotspot temperature of tie bars when a DC profile occurs in the transformer winding. For that purpose two calculation models have been developed. The first one is a thermal model which considers some basic design parameters of the tie bar and the influence of the oil temperature in the transformer tank. The second model is a computation method to determine the losses in the tie bar for a given DC level in the winding. The basis of this model is an electro-magnetic network which calculates the eddy currents in the tie bars which are the reason for the losses during the core saturation.

In order to verify these modeling techniques several DC experiments were carried out in a test laboratory. The first unit was also equipped with flux measuring loops in order to measure the flux behavior. It could be shown that the measured fluxes in the tie bar correlates well with the calculated ones. This indicates that the demonstrated technique to calculate the losses in tie bars is adequate. In addition the transient temperature behavior of the tie bar was measured for different transformer designs and compared with the calculation results of the thermal model. The deviations between the measured and calculated temperatures are small. Therefore the demonstrated models are suitable to simulate the transient temperature behavior of the tie bar under DC excitation.

Furthermore could be shown, that the voltage wave form has an influence on the temperature under DC excitation. Simulations with pure sinusoidal voltages resulted in higher temperatures than calculations which use the measured and distorted voltages during the DC experiments. Therefore also the voltage wave form must be considered for a correct simulation of the hotspot behavior during a solar storm. However, by the help of the demonstrated calculations models is this easily possible.

6 Discussion

6.1 Grid stability

This thesis answers questions about two major issues in the field of risk assessment for power transformers due to GIC. On the one hand the transformer performance to study the grid stability during a solar storm can be determined by the help of the developed calculation models. On the other hand an evaluation of the transformer DC withstand capability is possible, because this thesis shows in detail how to calculate the tie bar hotspot temperature behavior in case of additional DC currents in the transformer winding. The validity of the calculation models was verified with unique DC experiments in a test laboratory. Several transformer designs were tested regarding their harmonic and hotspot performance under DC and the calculation models could be proofed in an accurate manner.

A key subject for the grid stability during a GIC storm is the knowledge of the reactive power demand for the installed transformers in the power network. This is important because a solar event may affect many transformers in the grid and as a consequence the reactive power demand increases significantly what can be a burden for the system. Power utilities study such scenarios in order to identify the risk of a voltage collapse. A procedure of such a case study is shown in [52]. An existing approach to determine the reactive power of a transformer under DC is the commonly called K_Q-factor. This factor describes the increase of the transformer fundamental reactive power demand ΔQ due to a DC current in the winding for a certain voltage level. That means ΔQ is given with[9]:

$$\Delta \mathrm{Q} = \mathrm{K}_{Q} \cdot \mathrm{I}_{\mathrm{DC}} \tag{39}$$

Reference [53] demonstrates some values for the K_Q-factor depending on the core design and the service voltage of the transformer. Certainly the discussed simulation models in chapter 4 are also suitable to determine the fundamental reactive power demand of the transformer for a certain DC level in the winding and calculation results for three different transformer designs, which were studied in chapter 4, are demonstrated in Figure 79. It can be seen from the figure that the simplified approach with one factor is only suitable for single-phase and T5 Core-Type transformers. The behavior of transformers with a T3 Core-Type design cannot be depicted with equation (39). As already demonstrated, for such core designs a certain amount of DC in the winding is needed in order to reach the saturation level. That means the increase of the reactive power starts not at zero and therefore at least one additional parameter is needed to describe the behavior of the reactive power increase with the DC level. Such an adopted formula can be written with

$$\Delta \mathrm{Q} = \max\left\{\left(\mathrm{K}_{Q} \cdot \mathrm{I}_{\mathrm{DC}} + \mathrm{d}_{\mathrm{Q}}\right), 0.0\right\} \tag{40}$$

where the parameter d_Q is used to avoid that the increase of the reactive power starts at zero. Nevertheless, an exact determination of the reactive power over the DC level is not possible by the help of such an estimation formula and a curve with several points to describe the increase of the reactive power with DC is the best option.

---

[9] It must be noted, that the K_Q-factor is only valid for a specific voltage. A change in the applied service voltage leads to a different K_Q-factor.

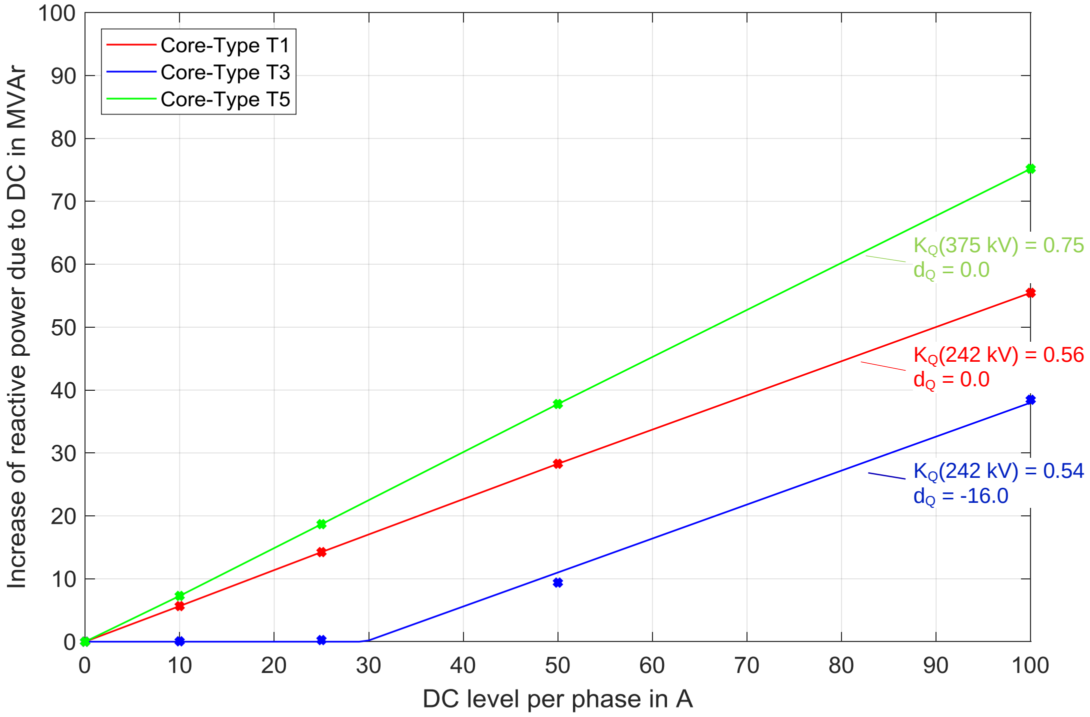

Figure 79: Increase of reactive power due to DC for different transformer designs

6.2 DC withstand capability of transformers

This thesis demonstrated how to calculate the DC-caused hotspot temperature of a tie bar for different types of power transformers and different tie bar designs. In order to determine the transformer DC withstand capability out of it, Figure 80 compares the hotspot behavior of two different tie bars which were studied in chapter 5.1.4. The figure shows that Design 1 neglects GIC effects and Design 2 takes them into account. The temperatures in the figure are based on a Topoil temperature of 80 °C in the transformer tank which represents a realistic condition for full load.

To determine from such curves the permissible DC level in the winding, the maximal allowed temperature for the tie bars must be known. Here the loading guides for liquid immersed power transformers can be used, because these guides give numbers for acceptable hotspot temperatures at steel parts depending on the type of insulation which is in contact with the heated surface ([54], [55]). For a continuous DC excitation the long-time emergency limits of the guides can be used. That means that the maximal hotspot temperature is 140 °C when cellulose material is used for the tie bar insulation and 160 °C when the insulation is based on glass fiber material. For the examples in Figure 80 are 160 °C assumed as permissible temperature. As a consequence Design 1 in the left part of the figure has a DC withstand capability of about 20 A DC per phase whereas Design 2 at the right-hand side does not reach the critical temperature level. This shows that the DC withstand capability can be significantly influenced by the help of suitable design measures. It must be noted that Figure 80 shows the steady-state hotspot temperatures when the DC current is applied continuously in the winding. However, the DC withstand capability is only the basis to evaluate the thermal risk during a solar storm as discussed in the flowing chapter.

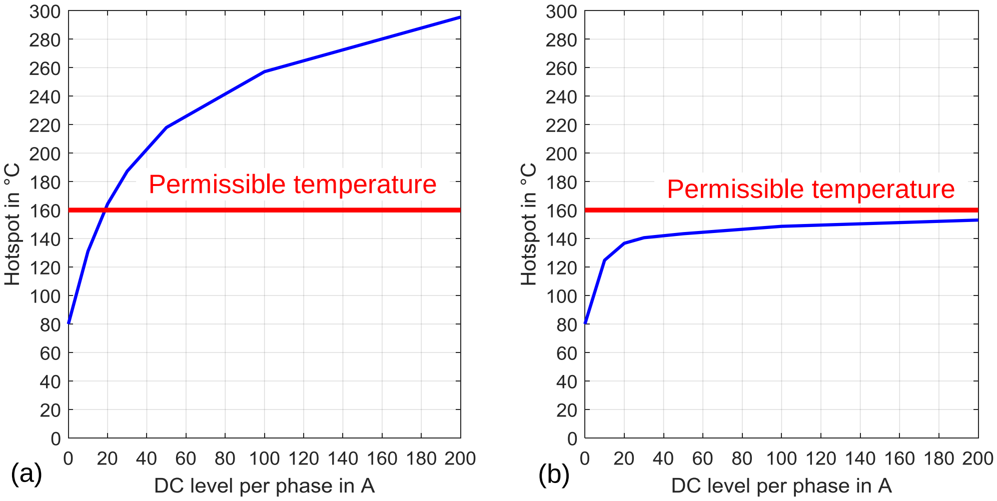

Figure 80: Examples of DC withstand capability curves – GIC effects are (a) in Design 1 neglected and (b) in Design 2 considered

6.3 GIC withstand capability of transformers

As demonstrated in Figure 4, GIC in transformer neutrals have a very dynamic characteristic. Hence two transient influence factors must be considered to analyze the temperature behavior for a GIC profile. The first one is a potential time delay of the GIC magnitudes due to the magnetic behavior of the core and the second one is the thermal time constant of the affected component itself. This means, if a DC voltage occurs at the transformer neutral, then it will take some time in order to reach the full DC current in the winding and only when the core is in saturation significant losses occur which cause additional heating.

To consider such a delay due the magnetic core, the temporal shifting of the core flux away from its symmetrical position with identical peaks in positive and negative direction must be identified as demonstrated in Figure 7. This delay effect may be especially noticeable when a delta-connected low voltage winding is present in the transformer [1]. In that case the velocity of the flux shifting depends on the low voltage winding and such windings have typically a very low ohmic resistance value. The DC current which is flowing in the high-voltage winding of a transformer with a delta-connected low-voltage winding is balanced at first by an equivalent current through the delta connection. Nothing happens to flux in the core at this moment. However, the balancing DC current causes a DC voltage drop across the delta-connected winding according to its ohmic resistance. Consequently, in case of delta-connected low voltage winding u_{DC} can be calculated with:

$$u_{DC} = R_{ohm} \cdot \frac{N_{HV}}{N_{LV}} \cdot I_{GIC} \tag{41}$$

This DC voltage starts to generate the DC flux component in the core which shifts the AC flux away from the symmetrical position. A simplified approach for this process is the solution of the following differential equation which describes the relationship between the DC flux in the core and the DC voltage at the winding.

$$u_{DC} = N_{LV} \cdot \frac{d\Phi_{DC}}{dt} + \frac{\Phi_{DC} \cdot R_{m,DC} \cdot R_{ohm}}{N_{LV}} \tag{42}$$

The magnetic resistance $R_{m,DC}$ in formula (42) is not a constant value and depends on the absolute maximal value of the flux density in the core (AC+DC) and can be calculated with:

$$R_{m,DC} = \frac{l_{DC}}{\mu_0 \cdot \mu_r(B_{max}) \cdot A_c} \tag{43}$$

To reflect that the DC flux in the core can be positive as well as negative, B_{max} is given with:

$$B_{max} = \frac{|\Phi_{DC} + sgn(\Phi_{DC}) \cdot \Phi_{AC}|}{A_C} \tag{44}$$

An example for the calculation of such a delay effect due to the transient behavior of the core flux is demonstrated in Figure 81. The input parameters for this calculation are summarized in Table 28. It can be seen, that the GIC magnitudes which cause really a core saturation are damped compared to the assumed undamped GIC profile at the neutral of transformer. As shown in Figure 3, GIC is caused by a DC voltage at the neutral. Consequently, it could be happening that some DC voltages which occur at the grounded neutral of the high-voltage winding will not cause any additional heating in a transformer, especially when low magnitudes change frequently from positive to negative or vice versa. The reason is that the core is never saturated at these moments. This phenomenon is shown in Figure 81c.

Table 28: Parameter to determine the delay of GIC due to the transient behavior of the core

Parameter	**Value**
A_C	0.7105 m²
l_{DC}	10.0 m
N_{HV}	1050
N_{LV}	60
R_{ohm}	0.0016 Ω
Φ_{AC}	1.0324 Vs

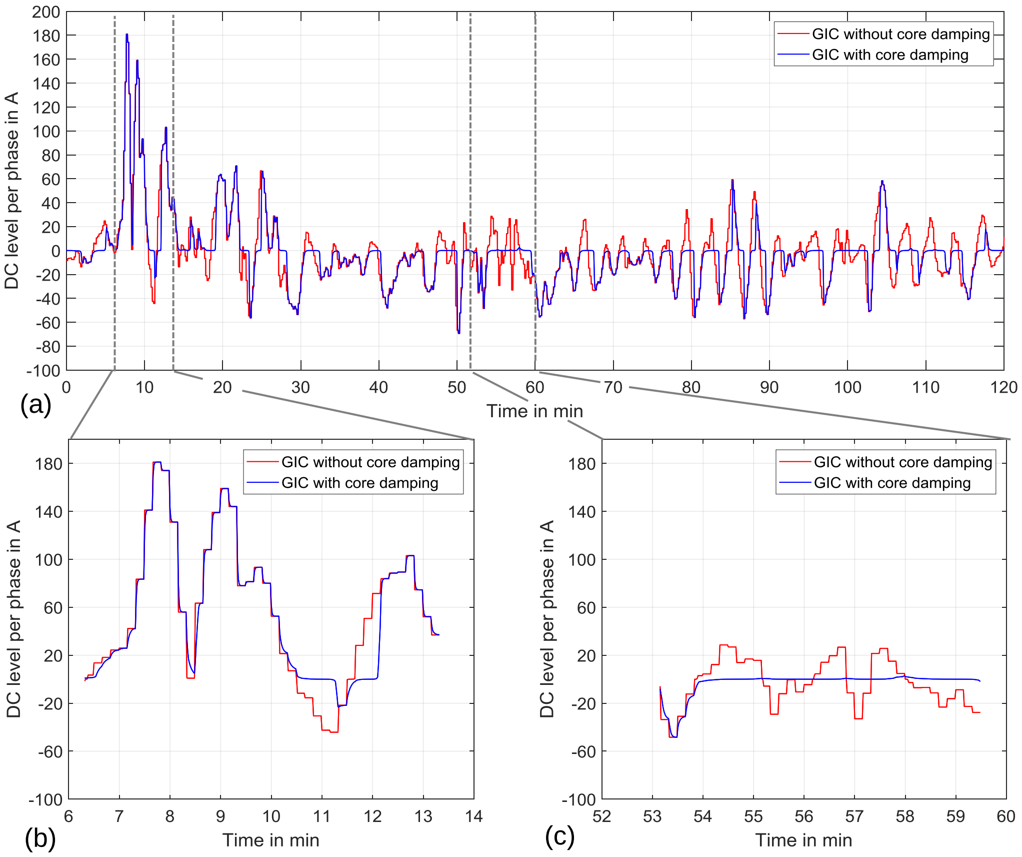

Figure 81: Delay of GIC magnitudes due core flux behavior: (a) Total GIC profile, (b) Zoomed period between minute 6 and 14, (c) Zoomed period between minute 52 and 60

For a determined GIC profile the transient hotspot behavior can be analyzed. For that reason the absolute values of the GIC magnitudes can be built to get a DC profile. Figure 82 shows for both tie bar designs which are demonstrated in Figure 80 the transient temperature behavior assuming the GIC profiles of Figure 81. It can be seen, that Design 1 exceeds the temperatures limits of the standards and causes a heating of more than 200 °C, whereas Design 2 shows only moderate temperature increases with the same GIC profiles. Also when the potential damping due to a delta-connected low-voltage winding is considered the hotspot temperatures of Design 1 are high. Potential risks of such high temperatures are gassing and consequently a tripping of the transformer during the solar storm due to a critical gas concentration in the Buchholz relay[10]. If the temperatures are extremely high, also a degradation of insulation material is possible and the risk of bubbling in the transformer increases [56]. This effect is especially in older transformers with increased moisture contents a topic [57]. However, not only the absolute hotspot temperature determines all potential risks, also a very high temperature gradient between the heated tie bar and the oil temperature in the tank can cause problems. Such high temperature gradients result in significant length variations of the heated material which must be also considered in the transformer design.

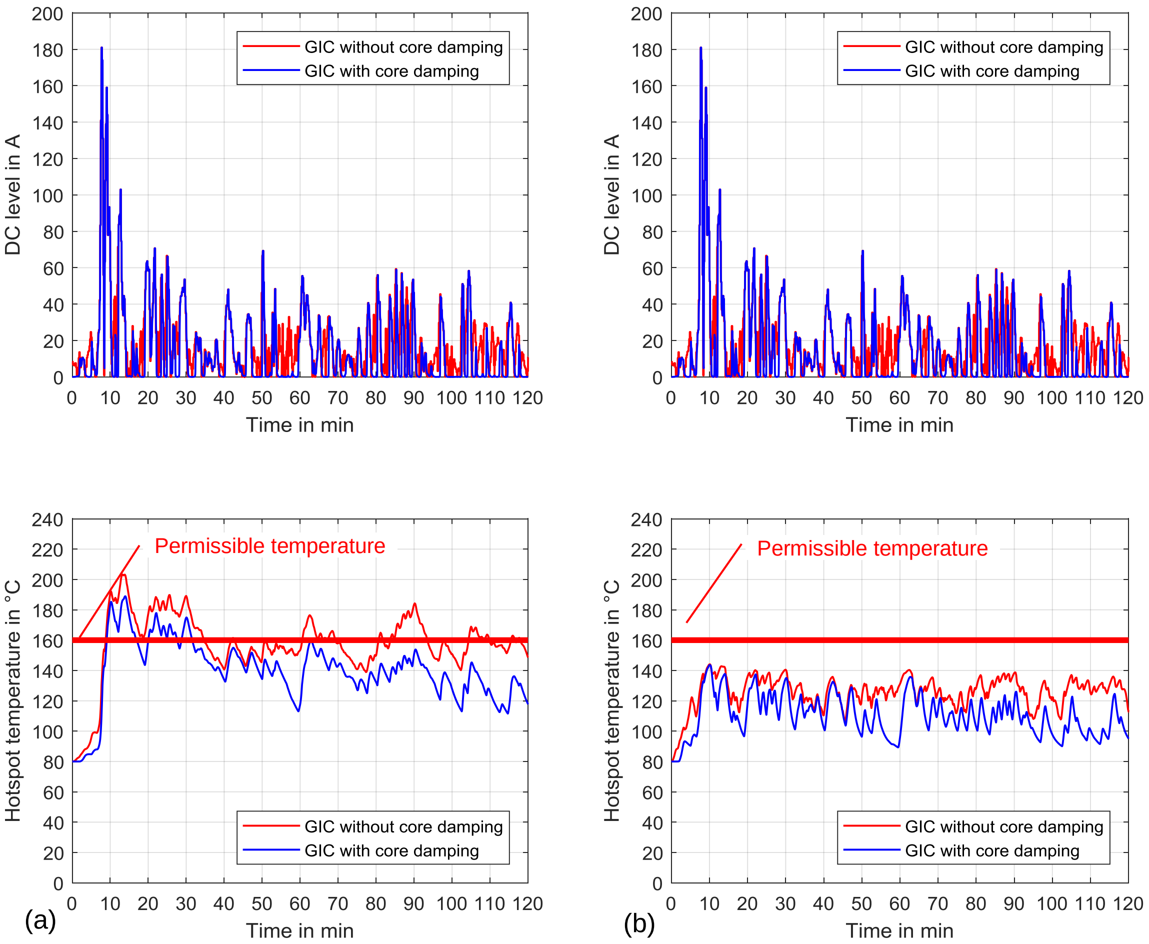

Figure 82: Example for the tie bar heating during GIC profiles: (a) GIC effects are neglected in the design, (b) GIC effects are considered in the design

6.4 *Simplification of GIC signatures for requirements in transformer specifications*

The examples in Figure 80 and Figure 82 show that an overheating of tie bars during a solar storm is possible, when GIC effects are not correctly considered in the transformer design.

---

[10] A Buchholz relay is a safety device in a power transformer.

This opens two main questions. The first one concerns new transformers which are still in the planning stage. Here a suitable requirement for the DC withstand capability must be fulfilled in order to avoid overheating during a certain GIC profile. This question can be answered by the nature of GIC. It can be seen from Figure 82, that low base DC levels can occur longer and that within this longer time period high and short pulses are possible. This characteristic can be covered in a simplified GIC signature as discussed in [1] and demonstrated in Figure 83.

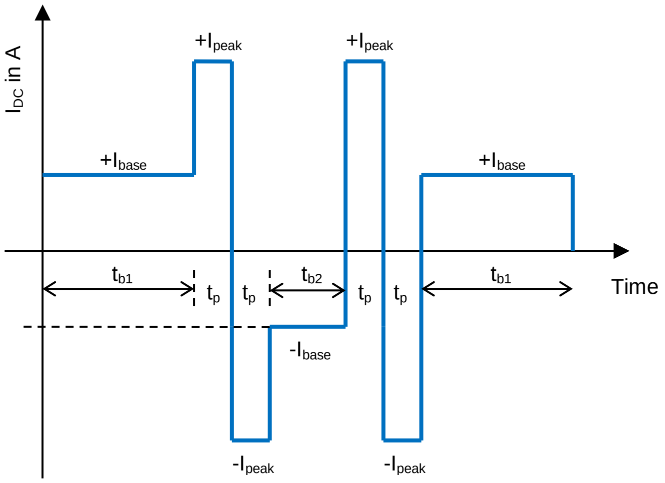

Figure 83: Simplified GIC signature in [1]

However, in respect to cover the thermal behavior of such a simplified GIC profile, it can be further simplified with the assumption that the base level has an infinite long duration. In that way the transformer must be able to withstand such DC base levels (I_{base}) independent from their durations. This postulation is realistic because GIC storms can last up to a few days as already mentioned before in this thesis. Consequently, the simplified DC profile captured in Figure 84 will cover the potential heating during a solar storm and such a simple DC profile can be easily used in transformer specifications as a requirement in order to avoid overheating during GIC storms. This means the manufacturer must ensure that the steady-state hotspot temperatures during the DC base level (I_{base}) is below 160 °C or 140 °C depending of the insulation material and that hotspot temperature after the DC peak level (I_{peak}) is lower than 200 °C or 160 °C.

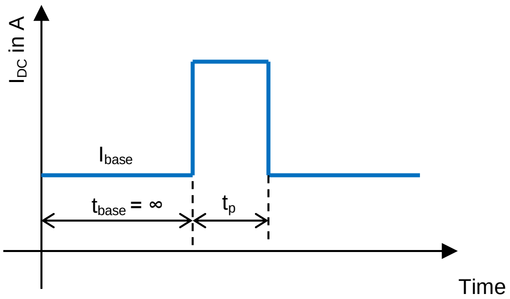

Figure 84: Simplified DC profile to cover thermal behavior of a GIC storm

The required parameters for the simplified DC profile can be derived out of any GIC profile[11]. The magnitude and the duration of the DC peak level (I_{peak}, t_{peak}) are determined with the maximal occurring pulse of the whole GIC storm profile. In order to find the magnitude of the DC base level (I_{base}), the highest 30-minute average of the whole GIC storm profile can be used for instance. This is reasonable, because the thermal time constant of tie bars is small in the range of about 10 minutes and therefore after 30 minutes the steady-state heating of the component is almost reached. For the demonstrated GIC profile in Figure 82 (red line, without damping) the parameters of the simple DC profile are captured in Table 29.

---

[11] The calculation of realistic GIC profiles in transformer neutrals is demonstrated in [58].

Table 29: Parameter for a simplified DC profile to cover the heating of a GIC profile

I_{base}	I_{peak}	t_{peak}
27 A DC/phase	180 A DC/phase	2 minutes

6.5 Screening criteria for GIC affected transformers

The second question regarding the DC withstand capability is much more complex and raises for already existing transformers where no data is available. For such units a screening criterion would be helpful which indicates the maximal permissible GIC profile where no overheating can be expected in the transformer. However, it is obvious that the answer of this question depends on the shape of the DC withstand capability curve and unfortunately this curve can strongly vary between different transformers as shown in Figure 80.

Nevertheless, to demonstrate a potential screening criterion, Figure 85 illustrates the permissible values for DC magnitudes and their durations based on Design 1 of Figure 80. It can be seen, that DC levels up to 20 A DC per phase do not cause a critical hotspot temperature above 160 °C, even if the DC current occurs very long. With higher DC levels the hotspot temperature would exceed 160 °C and the durations of such high DC magnitudes may not exceed a certain period of time in order to keep the hotspot temperature acceptable. Therefore Figure 85 shows also the permissible duration for a certain DC magnitude in order to avoid overheating (180 °C).

However, the big design influence on the steady-state hotspot temperature indicates that a precise screening without design information is not possible. Therefore for new units it is essential that the DC withstand capability is determined from the beginning and for already existing units the vendor must be able to give information regarding the behavior under DC. Only then is an accurate screening ensured.

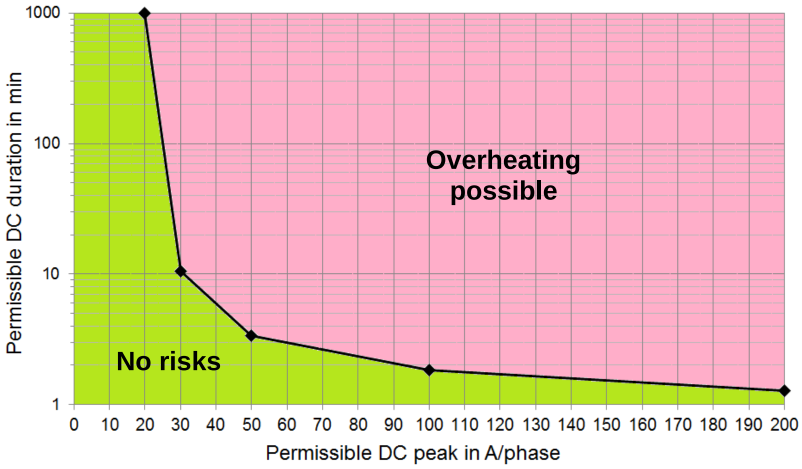

Figure 85: Screening criteria (based on Design 1) to evaluate GIC risks

Summarized can be said, that for new transformers requirements for the DC withstand capability should be specified in order to avoid problems for an expected GIC profile. Then the manufacturer must ensure that the design is able to fulfill these requirements, for instance by the help of a DC test or with a design-specific modelling approach as it is demonstrated in this thesis. For older transformers, where the DC withstands capability is not known, is an accurate screening difficult. Therefore each vendor should be able to determine the DC withstand capability also for already existing units in order to ensure an accurate screening.

7 Future Work

Two topics remain for future work. On the one hand standardized test methods have to be developed in order to measure the main DC parameters of a power transformer. These parameters are the saturation flux linkage, the saturation inductance L_{sat} and the DC zero inductance $L_{DC,0}$. The knowledge of these parameters is valuable, because the transformer behavior under DC can be determined with these parameters as demonstrated in chapter 4.5. A second topic for the future is the advancement of the electro-magnetic network model. Figure 80 showed that a suitable tie bar design shows acceptable hotspot temperatures, also for high GIC peaks. Therefore, other components like the transformer windings may become more critical at very high DC levels. Consequently, the next step is the development of a model which is also suitable to simulate the effect of GIC on the winding hotspot. For that purpose the magnetic models in chapter 4.1 must be extended to allow load simulations. This could be reached by the modeling of several windings in the magnetic network. However, to verify such a load model, a test setup for a DC experiment under load must be develop. Up to now DC tests are always done in the no-load condition. The idea to reach the ambition of a load test is to use two transformers with a voltage regulation on the high-voltage system. Figure 86 shows a potential test circuit for this purpose. If the tap positions of these transformers are in opposite direction (maximal vs. minimal tap position), then an AC load current is expected in addition to the DC current. That means that with an appropriate DC source also load scenarios with DC would be testable in order to prove different simulations models under load.

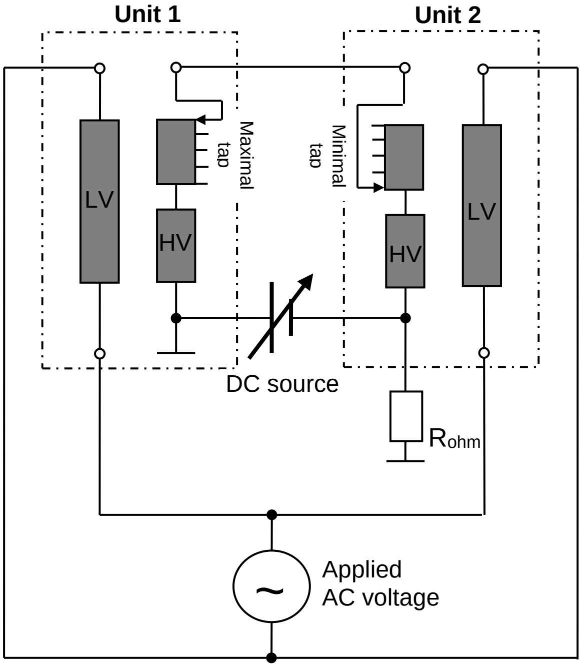

Figure 86: Idea for a test setup for a DC test with load

8 Summary

This thesis discusses the impacts of solar storms on power transformers and provides calculation models to quantify the effects on different types of transformer designs.

Chapter 2.2 illustrates the main problems which can occur at the operation of power transformers during solar storms. One the one hand additional harmonics and large reactive power swings are present in the power system and on the other hand the temperatures of internal components in affected transformers are increasing. Such problems are documented in different power grids in the past (Table 1). Geomagnetical Induced Currents (GIC) in grounded transformer neutrals are the reason for these unwanted effects during a solar storm. This GIC phenomenon is a series of DC pulses which influence the nominal AC operation of transformers as discussed in chapter 2.3. A DC current in a transformer winding causes an offset in the core flux and consequently the saturation level of core material can be reached. This explains the occurrence of the additional harmonics, the increased reactive power demand and the rising temperatures during a solar storm, because if the core flux reaches the saturation level, then additional stray flux can heat up transformer components and a significant peak occurs in the exciting current of the transformer (Figure 5).

This indicates that two types of calculation models are required in order to simulate critical GIC effects. The first model should enable the calculation of the wave form of the exciting current in case of an additional DC current in the excited transformer winding. In that way the harmonics as well as the increased reactive power consumption can be determined. The second model is required in order to simulate the increase of the internal hotspot temperature in case of a GIC event. However, as shown in chapter 3.2, different designs of power transformers are installed in power grids and differences in the design influence also the effects of the GIC in the transformer. Therefore design-specific approaches for the calculation models have been developed in this thesis to close current research gaps.

Chapter 4 shows how to calculate the wave form of the exciting current for a certain power transformer design. The structure of different electro-magnetic network models and their parametrization is discussed for different types of single-phase and three-phase transformers. As shown in chapter 4.2.3, for all types of single-phase units the air-core inductance is the major parameter which determines the wave form of the exciting current. At three-phase transformers is the calculation of the exciting current more complex as shown in chapter 4.3.2. Here significant differences occur between the two possible core designs for three-phase units (T3 and T5). A three-phase transformer with a T3 core needs a certain amount of a DC current in the excited winding in order to reach the core saturation. Below these DC levels no additional harmonics occur. The consequence is a kind of offset in the wave form of the exciting current together with the three main peaks during the saturation of the main core limbs. This contrasts with a three-phase transformer with a T5 core where the saturation starts already at very low DC levels. Furthermore, additional peaks are present in the exciting current of a T5 core unit. These peaks are caused by the saturation of the yokes and the return limbs (Figure 36). In order to verify the calculated effects and to ensure the validity of the simulation models, different DC experiments were carried out in a test laboratory. Different single-phase and three-phase units have been tested and the results were compared with the corresponding calculation results. This verification of the harmonic model is shown in chapter 4.4 and a good correlation between the measured and calculated currents was achieved for each experiment.

Chapter 5 discusses the second simulation model which is needed to evaluate the risk of a GIC event on a power transformer. This chapter gives an approach to simulate the temperature of tie bars in detail. These are structural components for the mechanical stability of the active part. In order to reach such a calculation model the simulation technique of chapter 4 has been extended. In that way it is also possible to calculate the additional losses in the tie bar in case of an additional DC current in the winding, because this modeling technique simulates the occurring eddy currents in the material as shown in chapter 5.1.2. Nevertheless, also here are significant differences due to design variations possible as discussed in 5.1.4, but with the demonstrated calculation technique such differences can be considered. The validation of this hotspot model has been done with unique DC experiments, using additional temperature sensors and flux measuring loops in transformers. The verification process is discussed in chapter 5.2. In total five different transformers have been tested with different DC profiles and a good correlation between the measurement and simulation was reached (Figure 76).

By help of the developed calculation models different aspects for the operation of power transformers during a solar storm have been discussed in chapter 6. One major question is the grid stability during a GIC event due to the increase of the reactive power demand in the power system. To answer this question the harmonic model of chapter 4 can be used. A further question which is discussed in chapter 6 are differences in the DC withstand capability of a power transformer. Figure 80 shows that the tie bar temperatures due to a DC excitation can be significant influenced by the design of a power transformer. Design 1 represents an option where the steady-state hotspot temperatures of the tie bar reaches critical temperature levels of about 300 °C, whereas Design 2 is optimized in respect to DC and shows only a moderate and acceptable temperature increase. Such DC withstand capability curves are fundamental to determine the temperature behavior during a solar storm. However, to determine the hotspot behavior for a GIC profile two transient effects must be considered as shown in chapter 6.3. The first one is a delay effect due to the magnetic behavior of the core and the second one the thermal time constant of the tie bar itself. An example with a certain GIC profile showed that these transient effects lead to a significant damping of the hotspot temperatures. This means under GIC the temperatures are much lower than the temperatures what are achieved in the steady-state DC condition. However, Design 1 shows also during the GIC profile high temperatures. (Figure 82).

Chapter 6.4 shows how power utilities can specify a DC profile in specifications for new transformers. In that way problems due to GIC can be avoided because the manufacturer must ensure that the design is able to fulfill these requirements. This can be done with a design-specific modeling approach as shown in this thesis and by the help of an DC experiment in the test bay of the manufacturer.

The last question which is discussed in chapter 6 is a screening criterion for GIC affected transformers. However, the output of such a screening depends strongly on the DC withstand capability of the transformer. Figure 85 shows an example with Design 1 which neglects GIC effects. However, a screening of already existing transformers is complex and requires always some design information as shown in this thesis. Only with these design parameters of the transformer is a reliable risk evaluation for a specific solar storm possible.

9 References

[1] IEEE C57.163, *"IEEE Guide for Establishing Power Transformer Capability while under Geomagnetic Disturbances"*, 2015.

[2] K. R. Lang, *"The Cambridge Encyclopedia of the Sun"*, pp. 167-168, Cambridge University Press, 2001.

[3] A. Hanslmeier, *"Die Sonne als Stern und das Wetter im Weltraum"*, pp. 78-82, bookboon.com, 2016.

[4] NASA, *"Number of Sunpots"*, Available at: https://www.nasa.gov/images/content/599325main_ssn_yearly.jpg.

[5] J. Elovaara, P. Lindblad, A. Viljanen, T. Mäkinen, R. Pirjola, S. Larsson and B. Kielen, *"Geomagnetically Induced Currents in the Nordic power system and their effects on equipment, control, protection and operation"*, CIGRE, Paris, Report 36-301, 1992.

[6] A. W. P. Thomson, A. J. McKay, E. Clarke and S. J. Reay, *"Surface electric fields and geomagnetically induced currents in the Scottish Power grid during the 30 October 2003 geomagnetic storm"*, Space Weather Vol. 3, Report S11002, 2005.

[7] C. T. Gaunt and G. Coetzee, *"Transformer failures in regions incorrectly considered to have low GIC-risk"*, IEEE Power Tech, Lausanne, ISBN 978-1-4244-2189-3, 2007.

[8] R. A. Walling, *"Potential Impacts of Harmonics on Bulk System Integrity during Geomagnetic Disturbances"*, IEEE Power & Energy Society General Meeting, Vancouver, ISSN: 1932-5517, 2013.

[9] L. Bolduc, *"GIC observations and studies in the Hydro-Quebec power system"*, Journal of Atmospheric and Solar Terrestrial Physics: Vol. 64, pp. 1793-1802, 2002.

[10] R. Girgis, *"Effects of GIC on Power Transformers and Power Systems"*, Transmission and Distribution Conference and Exposition (T&D), IEEE PES, Orlando, Florida, ISSN: 2160-8555, 2012.

[11] I. A. Erinmez, J. G. Kappenman and W. A. Radasky, *"Management of the geomagnetically induced current risks on the national grid company's electric power transmission system"*, Journal of atmospheric and solar terrestrial physics: Vol 64, pp. 743-756, 2002.

[12] J. Kappenman, *"Geomagnetic Storms and Their Impacts on the U.S. Power Grid"*, Oak Ridge National Laboratory, Tennessee, 2010, Available at: https://www.ferc.gov/industries/electric/indus-act/reliability/cybersecurity/ferc_meta-r-319.pdf.

[13] M. Wik, R. Pirjola, H. Lundstedt, A. Viljanen, P. Wintoft and A. Pulkkinnen, *"Space weather events in July 1982 and October 2003 and the effects of geomagnetically induced currents on Swedish technical systems"*, Annales Geophysicae No. 27, pp. 1775-1787, 2009.

[14] M. Myllys, A. Viljanen, O. A. Rui and T. M. Ohnstad, *"Geomagnetically induced currents in Norway: the northernmost high-voltage power grid in the world"*, Space Weather Space Climate 4, Report A10, 2014.

[15] Chung-Ming Liu, Lian-Guang Liu and R. Pirjola, *"Geomagnetically Induced Currents in the High-Voltage Power Grid in China"*, IEEE Transaction on Power Delivery: Vol. 24, pp. 2369-2374, 2009.

[16] T. Halbedl, H. Renner and G. Achleitner, *"Analysis of the Impact of Geomagnetic Disturbances on the Austrian Transmission Grid"*, CIGRE, Paris, Report C3-101, 2016.

[17] R. A. Marshall, H. Gorniak, T. Van Der Walt, C. L. Waters, M. D. Sciffer, M. Miller, M. Dalzell, T. Daly, P. Pouferis, G. Hesse and P. Wilkinson, *"Observations of*

geomagnetically induced currents in the Australian power network", Space Weather: Vol. 11, pp. 6-16, 2013.

[18] J. Koen and T. Gaunt, *"Geomagnetically Induced Currents in the Southern African Electricity Transmission Network"*, IEEE Power Tech Conference, Bologna, Italy, ISBN: 0-7803-7967-5, 2003.

[19] A. W. P. Thomson, T. D. G. Clark and E. Clarke, *"Monitoring Geomagnetically Induced Current in the Scottish Power Grid"*, Available at: http://swe.ssa.esa.int/TECEES/spweather/workshops/SPW_W3/PROCEEDINGS_W3/BGS_gic.pdf.

[20] W. Chandrasena, S. Shelemy and D. Jacobson, *"A Review of Geomagnetic Disturbance (GMD) Effects in Manitoba"*, IEEE Power & Energy Society General Meeting, Vancouver, ISSN: 1932-5517, 2013.

[21] A. Pulkkinnen, S. Lindahl, A. Viljanen and R. Pirjola, *"Geomagnetic storm of 29-31 October 2003: Geomagnetically Induced Currents and their relation to problems in the Swedish high-voltage power transmission system"*, Space Weather: Vol. 3, Report S08C03, 2005.

[22] NERC, *"Transformer Thermal Impact Assessment"*, White Paper: Available at: https://www.nerc.com/pa/Stand/Project201303GeomagneticDisturbance Mitigation/Thermal_Impact_Assessment _2017_October_Clean.pdf.

[23] NASA, *"A Super Solar Flare"*, Available at: https://science.nasa.gov/science-news/science-at-nasa/2008/06may_carringtonflare, 2008.

[24] J. Raith and U. Schichler, *"Methods to Improve the Grid Resiliency under the Influence of GIC"*, CIGRE, Vancouver, Canada, Report 765, 2016.

[25] E. Reiplinger, *"Geräuscherhöhungen bei Großtransformatoren bei gleichstromüberlagerten Netzen"*, Elektrizitätswirtschaft, Jg. 91 Heft 6, pp. 278-284, 1992.

[26] Yan Li, Yanchao gao, Longnv Li, Di Zhang and Fangxu Han, *"Effects of DC Magnetic Bias on the Magnetic and Sound Fields of Transformer"*, Energy and Power Engineering: Vol. 5, No. 4B, pp. 1097-1100, 2013.

[27] H. Passath and F. Bachinger, *"Direct Current in the Power Grid and its Compensation"*, MATPOST, Lyon, France, 2015.

[28] F. Klammler, G. Leber, P. Hamberger, C. Neururer and W. Paulmair-Sattler, *"DC impact on noise and losses on transformers and the possibility of compensation"*, CIGRE A2, Cracow, Poland, 2017.

[29] J. Raith and U. Schichler, *"Risk Assessment of Electrical Equipment under the Influence of GIC"*, CMD 2016, Xi'An, ISBN: 978-1-5090-3397-3, 2016.

[30] W. Seitlinger, *"Transformer model, based on the magnetic circuit"*, CIGRE, Report A2-205, Paris, 2006.

[31] EMTP software, Available at: https://www.emtp-software.com/.

[32] J. Raith and S. Außerhofer, *"GIC strength verification of power transformers in a high voltage laboratory"*, University of Cape Town - GIC workshop, South Africa, 2014.

[33] M. Beltle, M. Schühle and S. Tenbohlen, "Influences of Direct Currents on Power Transformers caused by AC-HVDC Interactions in Hybrid Grids", International Symposium on High Voltage Engineering, Pilsen, Czech Republic, 2015.

[34] M. Beltle, M. Siegel, M. Gnädig, S. Tenbohlen, U. Sundermann and F. Schatzl, *"Beeinflussung von Leistungstransformatoren in Hybridnetzen"*, ETG Kongress, Berlin, ISBN: 978-3-8007-3550-1, 2013.

[35] M. Pfeiffer, S. Hedtke and C. M. Franck, *"Corona Current Coupling in Bipolar HVDC and Hybrid HVAC/HVDC Overhead Lines"*, IEEE Transactions on Power Delivery: Vol 33, pp. 393-402, 2018.

[36] Technologies for Transmission System, Available at: https://tyndp.entsoe.eu/2016/insight-reports/technology/.

[37] R. Girgis, K. Vedante and G. Burden, *"Methodology for evaluating the impact of GIC and GIC capability of power transformer designs"*, IEEE Power & Energy Society General Meeting, Vancouver, Canada, ISSN: 1932-5517, 2013.

[38] R. Girgis and K. Vedante, *"A Process for Evaluating the Degree of Susceptibility of a fleet of Power Transformers to Effects of GIC"*, IEEE PES T&D Conference and Exposition, Chicago, USA, ISSN: 2160-8555, 2014.

[39] K. Heuck, K. D. Dettmann and D. Schulz, *Elektrische Energieversorgung*, pp. 556 ff., Springer Verlag, 2007.

[40] R. A. Walling and A. H. Khan, *"Characteristics of transformer exciting current during geomagnetic disturbances"*, IEEE Transaction on Power Delivery: Vol. 6, No. 4, pp. 1707-1714, 1991.

[41] J. Raith, B. Wagner and S. Außerhofer, *"Risk evaluation for power transformers during solar storms"*, CIGRE SC A2 Colloquium, Report PS1-ID037, Zürich, 2013.

[42] M. Lahtinen and J. Elovaara, *"GIC Occurrences and GIC Test for 400 kV System Transformer"*, IEEE Transactions on Power Delivery: Vol. 17, No. 2, pp. 555-561, 2002.

[43] P. Picher, L. Bolduc, A. Dutil and V. Q. Pham, *"Study of the acceptable DC current limit in core-form power transformers"*, IEEE Transactions on Power Delivery: Vol. 12, No. 1, pp. 257-265, 1997.

[44] W. Seitlinger, *"A Thermo-Hydraulic Transformer Model"*, Conference of Electrical Power Supply Industry, Manila, 2000.

[45] G. Gotter, *"Erwärmung und Kühlung elektrischer Maschinen"*, pp. 42-44: Springer Berlin-Heidelberg, 1954.

[46] VDI-Gesellschaft Verfahrenstechnik und Chemieingenieurwesen, *VDI Heat Atlas*, pp. 1056 ff., Springer Verlag, 2010.

[47] O. Biro, G. Koczka, G. Leber, K. Preis and B. Wagner, *"Finite Element Analysis of Three-Phase Three-Limb Power Transformers Under DC Bias"*, IEEE Transactions on Magnetics: Vol. 50, ISSN: 0018-9464, 2014.

[48] O. Biro, G. Koczka and K. Preis, *"Finite element solution of nonlinear eddy current problems with periodic excitation and its industrial applications"*, Applied Numerical Mathematics 79, pp. 3-17, 2014.

[49] O. Biro and K. Preis, *"An efficient time domain method for nonlinear periodic eddy currents"*, IEEE Transaction on Magnetics, Vol. 42, No. 4, pp. 695-698, 2006.

[50] G. Koczka, S. Außerhofer, O. Biro and K. Preis, *"Optimal Convergence of the Fixed-Point Method for Nonlinear Eddy Current Problems"*, IEEE Transactions on Magnetics: Vol. 45, No. 3, pp. 948-951, 2009.

[51] G. Koczka and O. Biro, *"Fixed-point method for solving nonlinear periodic eddy current problems with T,Phi-Phi formulation"*, COMPEL Journal, pp. 1444-1452, 2010.

[52] K. S. Shetye, T. J. Overbye, Q. Qiu and J. Fleeman, *"Geomagnetic Disturbance Modeling Results for the AEP System: A Case Study"*, IEEE Power & Energy Society General Meeting, Vancouver, Canada, ISSN: 1932-5517, 2013.

[53] D. Xuzhu, Y. Liu and J. G. Kappenman, *"Comparative analysis of exciting current harmonics and reactive power consumption from GIC saturated transformers"*, IEEE

Power Engineering Society Winter Meeting, Columbus, USA, ISBN: 0-7803-6672-7, 2001.

[54] IEC 60076-7, *"Loading guide for mineral-oil-immersed power transformers"*, 2018.

[55] IEEE C57.91, *"IEEE Guide for Loading Mineral-Oil-Immersed Transformers and Step-Voltage Regulators"*, 2011.

[56] M. Koch and S. Tenbohlen, *"Wasser in Leistungstransformatoren - Richtig messen und den Zustand beurteilen"*, Stuttgarter Hochspannungs-Symposium, 2006.

[57] M. Scala, *"Moisture Assessment in Transformers including Overloading Limits"*, CIGRE, Report A2-202, Paris, 2008.

[58] NERC, *"Application Guide: Computing Geomagnetically-Induced Current in the Bulk-Power System"*, USA, 2013, Available at: https://www.nerc.com/comm/PC/Geomagnetic%20Disturbance%20Task%20Force%20GMDTF%202013/GIC%20Application%20Guide%202013_approved.pdf.

Appendix A – Symbols

Symbol	Unit	Description
α	W·m^{-2}·K^{-1}	Heat transfer coefficient (surface to oil)
β_{om}	K^{-1}	Thermal expansion coefficient at temperature T$_{om}$
κ	Ω^{-1}·m^{-1}	Electrical conductivity of tie bar material
λ	W·m^{-1}·K^{-1}	Thermal conductivity of insulation material
μ_0	N·A^{-2}	Magnetic field constant
μ_r	V·s·A^{-1}· m^{-1}	Relative permeability value of material
ρ_{om}	kg·m^{-3}	Density of oil at temperature T$_{om}$
$\Delta \mathrm{Q}$	MVAr	Increase of reactive power demand due to DC
Θ_b	A	Magneto-motive force
Φ_b	V·s	Magnetic flux in a resistance branch
Φ_l	V·s	Magnetic flux in a magnetic loop
Ψ	V·s	Flux linkage
a_{layer}	m	Circumference of a tie bar layer
A_α	m^2	Surface in contact with oil
A_λ	m^2	Surface in contact with insulation
A_C	m^2	Cross section of main limb
$\mathrm{A}_{\mathrm{layer}}$	m^2	Cross section of a tie bar layer
A_m	m^2	Magnetic cross section
A_{RL}	m^2	Cross section of return limb
A_S	m^2	Sum of axial tank shield cross sections
A_Y	m^2	Cross section of yoke
B	T	Flux density
$\mathrm{B}_{\mathrm{layer}}$	T	Flux density in tie bar layer
$\mathrm{B}_{L,ij}$	T	Flux density in limb in phase i and axial section j
B_y	T	Flux density in yoke part
B_{Ta}	T	Flux density in tank wall part a
B_{Tb}	T	Flux density in tank wall part b
B_S	T	Flux density in axial tank shields
$c_{p,om}$	W·s·kg^{-1}·K^{-1}	Specific heat capacity of oil at temperature T$_{om}$
d_{layer}	m	Thickness of a tie bar layer
d_{ins}	m	Thickness of insulation around tie bar
d_w	m	Average thickness of tank wall
d_Q	MVAr	Additional factor to describe the increase of reactive power demand due to DC
$\mathbf{D}$	-	Flux linkage matrix
D_C	m	Diameter of main core limb
D_I	m	Inner diameter of winding
D_O	m	Outer diameter of winding
D_{oil}	K	Longitudinal oil gradient at tie bar along height

Symbol	Unit	Description
f	Hz	Frequency
f_1	m	Manufacturer specific geometry function
f_2	m	Manufacturer specific geometry function
f_3	m	Manufacturer specific distances
$f(T_{om})$	-	Influence of oil temperature on heat transfer coefficient
g	$\mathrm{kg \cdot s^{-2}}$	Force of gravity
$g_{src-oil}$	K	Local temperature gradient between tie bar surface and oil
H	$\mathrm{A \cdot m^{-1}}$	Magnetic field strength
$H_{L,ij}$	$\mathrm{A \cdot m^{-1}}$	Magnetic field strength in limb in phase i and axial section j
H_y	$\mathrm{A \cdot m^{-1}}$	Magnetic field strength in yoke part
H_{Ta}	$\mathrm{A \cdot m^{-1}}$	Magnetic field strength in tank wall part a
H_{Tb}	$\mathrm{A \cdot m^{-1}}$	Magnetic field strength in tank wall part b
H_S	$\mathrm{A \cdot m^{-1}}$	Magnetic field strength in axial tank shields
H_{ax}	m	Axial height of a tie bar element
$\mathrm{H_{layer}}$	$\mathrm{A \cdot m^{-1}}$	Magnetic field strength in tie bar layer
H_{src}	m	Total height of heat source
I	A	Current
I_{base}	A	DC base level in simplified GIC profile
I_{ex}	A	Exciting current
$\mathrm{I_{eddy,RMS}}$	A	RMS value of eddy current in a tie bar layer
I_{peak}	A	DC peak level in simplified GIC profile
K_α	-	Leading factor in the function for the heat transfer coefficient
$K_{loss,center}$	-	Loss density factor in tie bar in axial center
$K_{loss,top}$	-	Loss density factor in tie bar in the height of axial winding end
K_Q	$\mathrm{MVAr \cdot A^{-1}}$	Factor to describe the increase of reactive power demand due to DC
l_m	m	Magnetic length
l_{DC}	m	Magnetic length of major DC flux path
L_1	m	Height of core limb
L_2	m	Height of main yoke
L_3	m	Distance between limb center to limb center
L_4	m	Distance main limb center to return limb center
L_5	m	Tank width
L_6	m	Tank length
L_7	m	Tank height
L_8	m	Height of tank shields
L_9	m	Stacking height of innermost yoke package
L_{10}	m	Stacking height of yoke
L_{11}	m	Length of outermost yoke package
$\mathrm{L_{DC-0}}$	H	DC zero-sequence inductance
$\mathrm{L_{sat}}$	H	Saturation inductance of excited winding

Symbol	Unit	Description
$\dot{m}$	$kg \cdot s^{-1}$	Mass flow in oil duct
mc_{src}	$W \cdot s \cdot K^{-1}$	Heat capacity of heat source (= tie bar)
mc_{oil}	$W \cdot s \cdot K^{-1}$	Heat capacity of oil
N_{turns}	-	Number of DC-carrying turns
N_{HV}	-	Number of turns in the high-voltage winding
N_{LV}	-	Number of turns in the low-voltage winding
P_{α}	W	Dissipated losses to local oil
P_{λ}	W	Dissipated losses via insulation
$\mathrm{P_{eddy,i}}$	W	Eddy losses of layer i
$P_{tot,src}$	W	Total losses in heat source (= tie bar)
$Q_{gen,src}$	W·s	Generated energy in source
$Q_{dis,oil}$	W·s	Dissipated energy via oil
$Q_{dis,ins}$	W·s	Dissipated energy via insulation
Q_{flow}	W·s	Transported energy by oil flow
$Q_{store,oil}$	W·s	Stored energy in oil
$Q_{store,src}$	W·s	Stored energy in source
R_{hyd}	$Pa \cdot s\ kg^{-1}$	Hydraulic resistance of tie bar cooling arrangement
R_m	$A \cdot V^{-1} \cdot s^{-1}$	Magnetic resistance
$R_{m,const}$	$A \cdot V^{-1} \cdot s^{-1}$	Constant part of magnetic resistance
$R_{m,DC}$	$A \cdot V^{-1} \cdot s^{-1}$	Magnetic resistance of major DC flux path
$\mathrm{R_{mag,layer,i}}$	$A \cdot V^{-1} \cdot s^{-1}$	Magnetic resistance of layer i
R_{ohm}	Ω	Ohmic resistance
$\mathrm{R_{ohm,eddy,i}}$	Ω	Ohmic resistance of eddy current turn i
t	s	Time
t_{base}	min	Duration of DC base level in simplified GIC profile
t_{peak}	min	Duration of DC peak level in simplified GIC profile
T	-	Structural matrix
THD	%	Total harmonic distortion
$T_{bot,oil}$	°C	Bottom oil temperature in transformer tank
T_{center}	°C	Surface temperature of tie bar in axial center
T_{om}	$\Omega^{-1} \cdot m^{-1}$	Local oil temperature in tie bar oil duct
T_{src}	°C	Surface temperature of tie bar
T_{top}	°C	Surface temperature of tie bar on top in height of winding end
$T_{top,oil}$	°C	Top oil temperature in transformer tank
U	V	Voltage
x_{α}	-	Exponent in the function for the heat transfer coefficient

Appendix B – Magnetic resistances

This appendix shows the calculation of the magnetic resistances in the electro-magnetic network structures for the investigated core designs. As already mentioned before a magnetic resistance is given with

$$R_m = \frac{l_m}{\mu_0 \cdot \mu_r \cdot A_m} \tag{45}$$

where A_m is the cross section of the material, l_m the magnetic length and μ_r the relative permeability which is a parameter for the magnetic conductivity. The following tables show the determination of the magnetic lengths and cross sections for all required magnetic resistances.

Variable magnetic resistances

<table>
<tr><th>Formula</th><th colspan="6">Sketch</th></tr>
<tr><td rowspan="4">$\boldsymbol{R_{L,ij} = \frac{0.333 \cdot L_1}{\mu_0 \cdot A_C} \cdot \frac{1}{\mu_r(B_{L,ij}, H_{L,ij})}}$</td><td colspan="2">*Core-Type T1*</td><td colspan="2">*Core-Type T2*</td><td colspan="2">*Core-Type T4*</td></tr>
<tr><td colspan="2">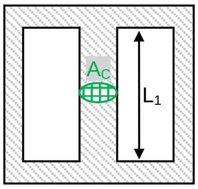
$i = 1, j = 1...3$</td><td colspan="2">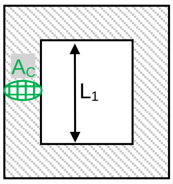
$i = 1 ... 2, j = 1 ... 3$</td><td colspan="2">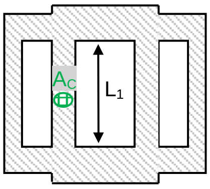
$i = 1 ... 3, j = 1 ... 3$</td></tr>
<tr><td colspan="3">*Core-Type T3*</td><td colspan="3">*Core-Type T5*</td></tr>
<tr><td colspan="3">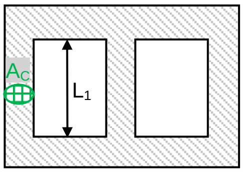
$i = 1 ... 2, j = 1 ... 3$</td><td colspan="3">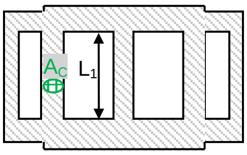
$i = 1 ... 3, j = 1 ... 3$</td></tr>
<tr><td rowspan="6">$\boldsymbol{R_Y = \frac{l_y}{\mu_0 \cdot n \cdot A_Y} \cdot \frac{1}{\mu_r(B_Y, H_Y)}}$</td><td colspan="2">*Core-Type T1*</td><td colspan="2">*Core-Type T2*</td><td colspan="2">*Core-Type T4*</td></tr>
<tr><td colspan="2">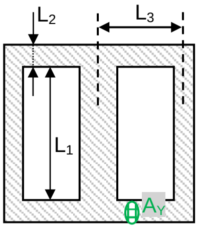 </td><td colspan="2">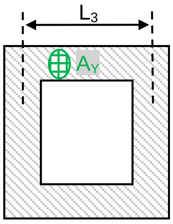 </td><td colspan="2">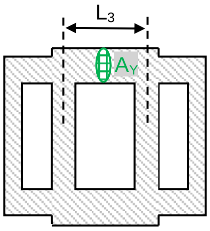 </td></tr>
<tr><td colspan="2">$l_y = 2 \cdot L_3 + 2 \cdot L_2 + L_1$
$n = 2$</td><td colspan="4">$l_y = 2 \cdot L_3$
$n = 1$</td></tr>
<tr><td colspan="3">*Core-Type T3*</td><td colspan="3">*Core-Type T5*</td></tr>
<tr><td colspan="3">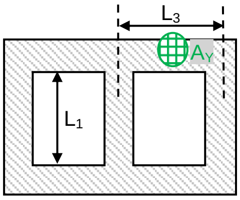 </td><td colspan="3">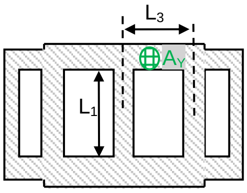 </td></tr>
<tr><td colspan="6">$l_y = 2 \cdot L_3$
$n = 1$</td></tr>
</table>

<table>
<tr><th>Formula</th><th colspan="2">Sketch</th></tr>
<tr><td rowspan="4">

$$R_{RL,i} = \frac{L_{RL}}{\mu_0 \cdot A_{RL}} \cdot \frac{1}{\mu_r(B_{RL,i}, H_{RL,i})}$$

$$L_{RL} = 2 \cdot L_4 + L_2 + L_1$$

</td><td colspan="2">

Only required for

</td></tr>
<tr><td>

Core-Type T4

</td><td>

Core-Type T5

</td></tr>
<tr><td>

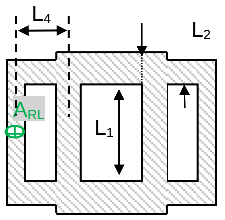

</td><td>

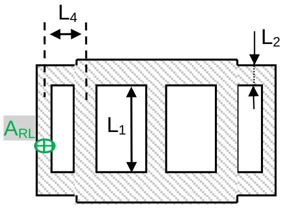

</td></tr>
<tr><td colspan="2">

$i = 1 \dots 2$

</td></tr>
<tr><td>

$$R_{Ta} = \frac{L_7 - L_8}{\mu_0 \cdot A_T} \cdot \frac{1}{\mu_r(B_{Ta}, H_{Ta})}$$

$$R_{Tb} = \frac{L_7}{\mu_0 \cdot A_T} \cdot \frac{1}{\mu_r(B_{Tb}, H_{Tb})}$$

$$A_T = 2 \cdot L_5 \cdot d_w + 2 \cdot d_w \cdot (L_6 - 2 \cdot d_w)$$

</td><td colspan="2">

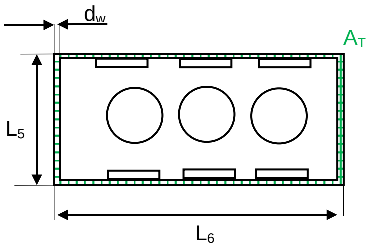

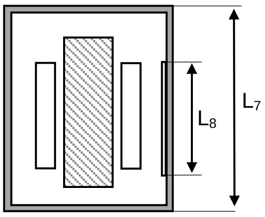

</td></tr>
<tr><td>

$$R_S = \frac{L_8}{\mu_0 \cdot A_S} \cdot \frac{1}{\mu_r(B_S, H_S)}$$

</td><td colspan="2">

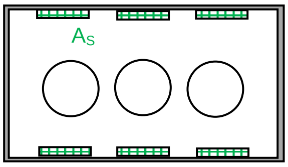

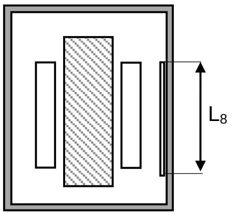

</td></tr>
<tr><td rowspan="2">

$$R_{Ci,j} = \frac{2 \cdot L_3}{\mu_0 \cdot A_{Ci}} \cdot \frac{1}{\mu_r(B_{Ci,j}, H_{Ci,j})}$$

$$R_{Co,j} = \frac{L_5 - D_C}{\mu_0 \cdot A_{Co}} \cdot \frac{1}{\mu_r(B_{Co,j}, H_{Co,j})}$$

$$A_{Ci} = D_C \cdot d_w$$

$$A_{Co} = (L_6 - 2 \cdot L_3) \cdot d_w$$

</td><td colspan="2">

only for Core-Type T5 required

</td></tr>
<tr><td colspan="2">

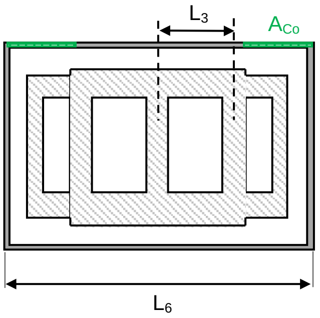

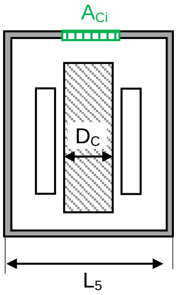

</td></tr>
</table>

Constant magnetic resistances

Formula	Sketch
$\boldsymbol{R_1 = \frac{0.5 \cdot (D_I - D_C)}{\mu_0 \cdot A_2}}$ $A_1 = \frac{\left(\frac{D_I + D_O}{2} + D_C\right)}{2} \cdot \pi \cdot \frac{L_1}{2}$	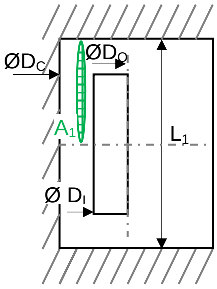 ØD_C ØD_O A₁ L₁ Ø D_I
$\boldsymbol{R_2 = \frac{0.333 \cdot L_1}{\mu_0 \cdot A_2}}$ $A_2 = \frac{\left({f_1}^2 - {D_C}^2\right) \cdot \pi}{4}$ $f_1 = f(D_I, D_O)$	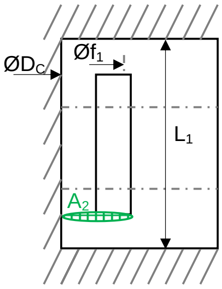 ØD_C Øf₁ L₁ A₂
$\boldsymbol{R_3 = \frac{0.333 \cdot L_1}{\mu_0 \cdot A_3}}$ $A_3 = \frac{\left({f_2}^2 - {D_C}^2\right) \cdot \pi}{4}$ $f_2 = f(D_I, D_O)$	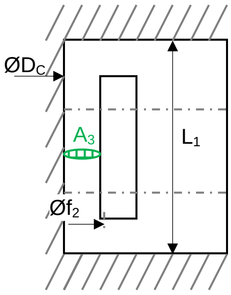 ØD_C A₃ L₁ Øf₂
$\boldsymbol{R_4 = \frac{L_7 - L_8}{\mu_0 \cdot A_{\mathrm{out}}}}$ $\boldsymbol{R_5 = \frac{L_8}{\mu_0 \cdot A_{\mathrm{out}}}}$ $A_{out} = 2 \cdot (L_5 + 2 \cdot f_3) \cdot f_3 + 2 \cdot L_6 \cdot f_3$	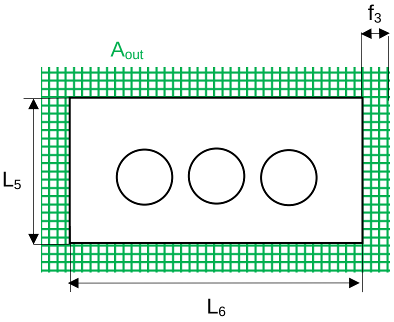 f₃ A_{out} L₅ L₆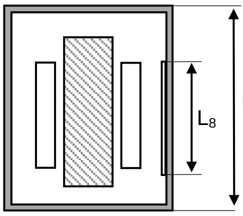

<table>
<tr><th>Formula</th><th>Sketch</th></tr>
<tr><td>

$$\boldsymbol{R_6} = \frac{\boldsymbol{L_1}}{\boldsymbol{\mu_0}\cdot\boldsymbol{A_6}}$$

$$A_6 = \frac{1}{n}\cdot\left(L_5\cdot L_6 - n\cdot\frac{{D_O}^2\cdot\pi}{4}\right)$$

</td><td>
<table>
<tr><td><i>Core-Type T1</i></td><td><i>Core-Type T2</i></td><td><i>Core-Type T4</i></td></tr>
<tr><td>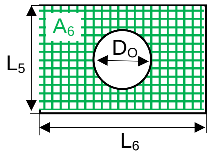
</td><td colspan="2">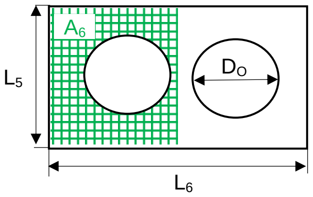
</td></tr>
<tr><td>$n = 1$</td><td colspan="2">$n = 2$</td></tr>
<tr><td colspan="2"><i>Core-Type T3</i></td><td><i>Core-Type T5</i></td></tr>
<tr><td colspan="3">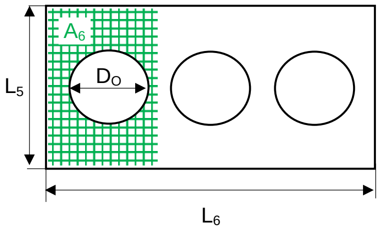
</td></tr>
<tr><td colspan="3">$n = 3$</td></tr>
</table>
</td></tr>
<tr><td>

$$\boldsymbol{R_7} = \frac{\mathbf{1}}{\sum_{i=1}^{n+2}\frac{\mathbf{1}}{\boldsymbol{R_{a,i}}}}$$

$$d_1 = 0.5\cdot(L_5 - L_{10})$$

$$d_2 = 0.5\cdot\sqrt{\left(\frac{L_{10}}{2} - L_9\right)^2 + \left(L_2 - \frac{L_{11}}{2}\right)^2}$$

$$\alpha = acos\left(\frac{0.5\cdot L_{10} - L_9}{2\cdot d_2}\right)$$

$$d_3 = d_1 + 2\cdot d_2\cdot cos(\alpha)$$

$$d_4 = 0.5\cdot(L_7 - L_1 - 2\cdot L_2)$$

$$d_5 = d_4 + 2\cdot d_2\cdot sin(\alpha)$$

$$d_6 = L_2 + d_4 - d_5$$

$$l_y = 2\cdot L_3 + L_2$$

$$R_{a,1} = \frac{d_4}{\mu_0\cdot L_9\cdot\frac{l_y}{m}}$$

$$R_{a,i} = \frac{l_i}{\mu_0\cdot\left(\frac{2\cdot d_2 + d_5 + d_3}{2\cdot n}\right)\cdot\frac{l_y}{m}}$$

$$R_{a,n+2} = \frac{d_1}{\mu_0\cdot d_6\cdot\frac{l_y}{m}}$$

</td><td>
<table>
<tr><td><i>Core-Type T1</i></td><td><i>Core-Type T2</i></td><td><i>Core-Type T4</i></td></tr>
<tr><td>$m = 1$</td><td colspan="2">$m = 2$</td></tr>
<tr><td colspan="2"><i>Core-Type T3</i></td><td><i>Core-Type T5</i></td></tr>
<tr><td colspan="3">$m = 3$</td></tr>
<tr><td colspan="3">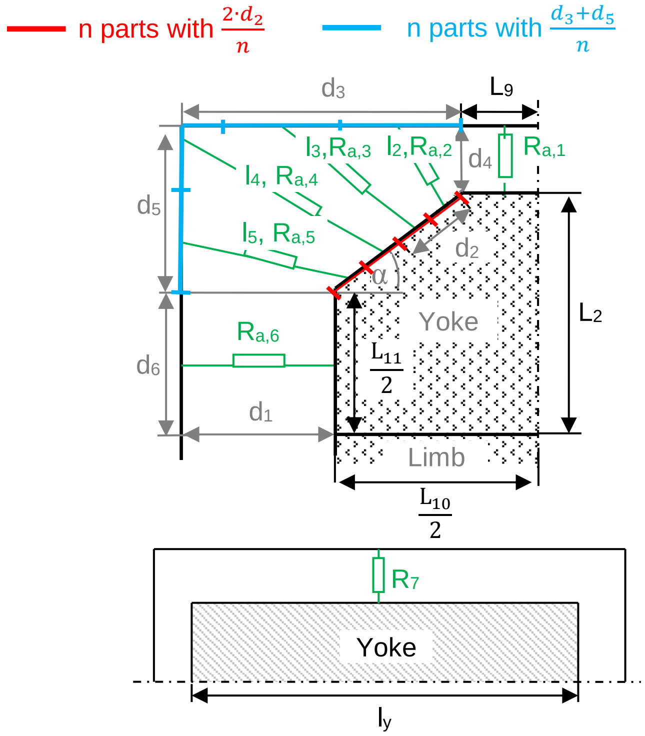
n parts with $\frac{2\cdot d_2}{n}$
n parts with $\frac{d_3+d_5}{n}$
d3
L9
l3,Ra,3
l2,Ra,2
Ra,1
d4
l4, Ra,4
d5
l5, Ra,5
d2
α
Yoke
L2
Ra,6
d6
$\frac{L_{11}}{2}$
d1
Limb
$\frac{L_{10}}{2}$
R7
Yoke
ly

</td></tr>
</table>
</td></tr>
</table>

Appendix C – Experiments to verify hotspot calculation

Overview

This appendix shows the analysis of each DC experiment which was carried out to verify the hotspot calculation. For each tested transformer the deviations between the measured and calculated temperatures are shown.

Table 30: Overview of DC tested power transformers

Transformer	Core-Type	Rated voltage with nominal core flux density	Power	Typ	Max. tested DC level
Unit 1	T1	230/√3 kV (1.71 T)	133 MVA	Auto	50 A DC/phase
Unit 2	T4	405/√3 kV (1.69 T)	570 MVA	GSU	25 A DC/phase
Unit 3	T5	420 kV (1.72 T)	200 MVA	Auto	3.9 A DC/phase
Unit 4	T1	500/√3 kV (1.45 T)	117 MVA	SVC	16.6 A DC/phase
Unit 5	T5	345 kV (1.59 T)	575 MVA	PST	33.3 A DC/phase
Unit 5a	T5	345 kV (1.59 T)	575 MVA	PST	50 A DC/phase

Results of hotspot test at Unit 1

Table 31: Temperatures in steady-state conditions at Unit 1

DC current	Sensor 1 (center)		Sensor 2 (top)		Local oil sensor (top)		Bottom oil
-	Measured value	Deviation	Measured value	Deviation	Measured value	Deviation	Measured value
	°C	K	°C	K	°C	K	°C
10 A DC	73	+2	60	+12	49	+7	26
20 A DC	102	+2	82	+10	61	+6	27
30 A DC	114	+1	96	+10	68	+3	28
40 A DC	121	+1	105	+10	75	+0	28
50 A DC	127	0	110	+11	77	-1	29

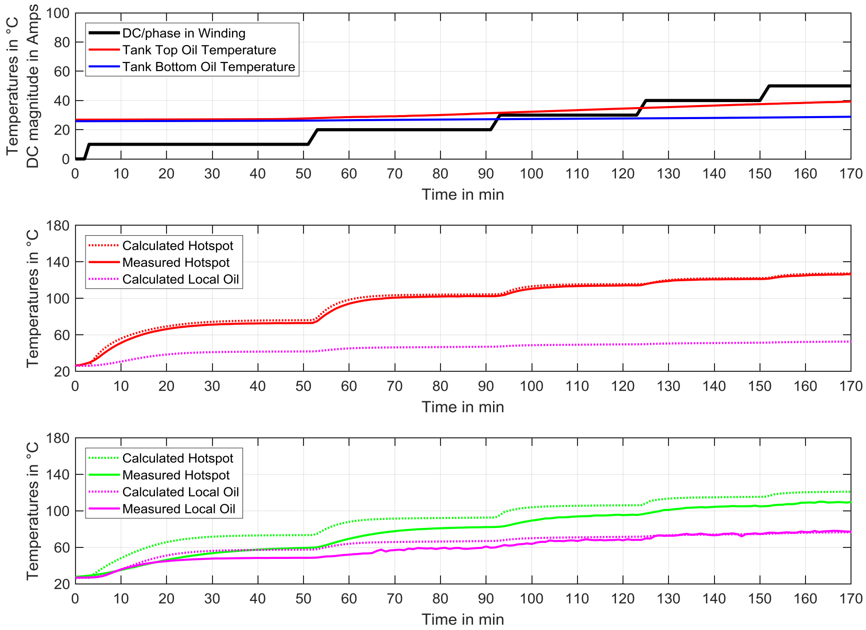

Figure 87: Results of hotspot test at Unit 1

Results of hotspot test at Unit 2

Table 32: Temperatures in steady-state conditions at Unit 2

DC current	**Hotspot sensor**		**Bottom oil**
-	Measured value	Deviation	Measured value
	°C	K	°C
5 A DC	54	-6	43
10 A DC	59	-2	44
20 A DC	69	-2	44
25 A DC	76	-3	45
Average deviation during whole test period: -4.3 K			

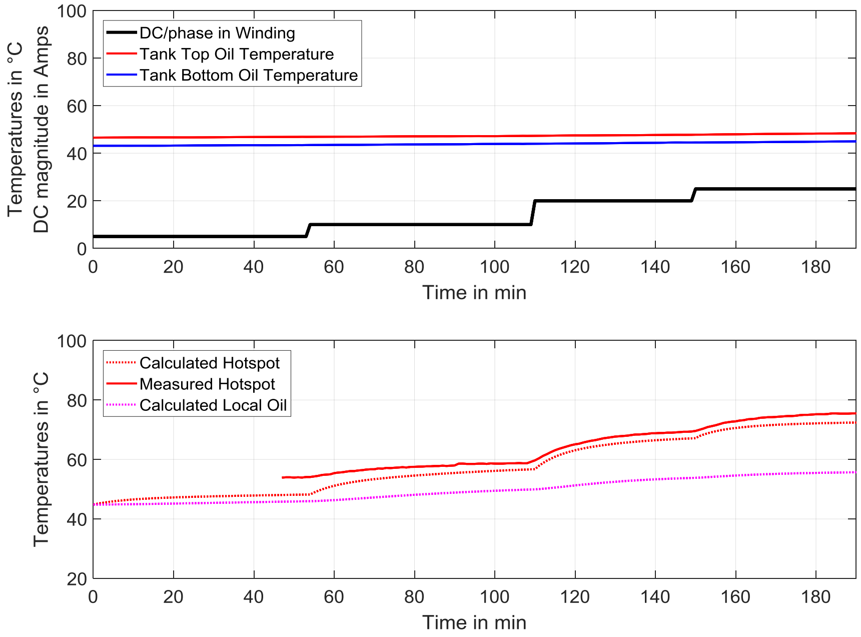

Figure 88: Results of hotspot test at Unit 2

Results of hotspot test at Unit 3

Table 33: Temperatures in steady-state conditions at Unit 3

DC current	**Hotspot sensor**		**Bottom oil**
-	Measured value	Deviation	Measured value
	°C	K	°C
1.3 A DC	39	-2	26
3.3 A DC	49	+0	28
3.9 A DC	52	+0	30
Average deviation during whole test period: -0.3 K			

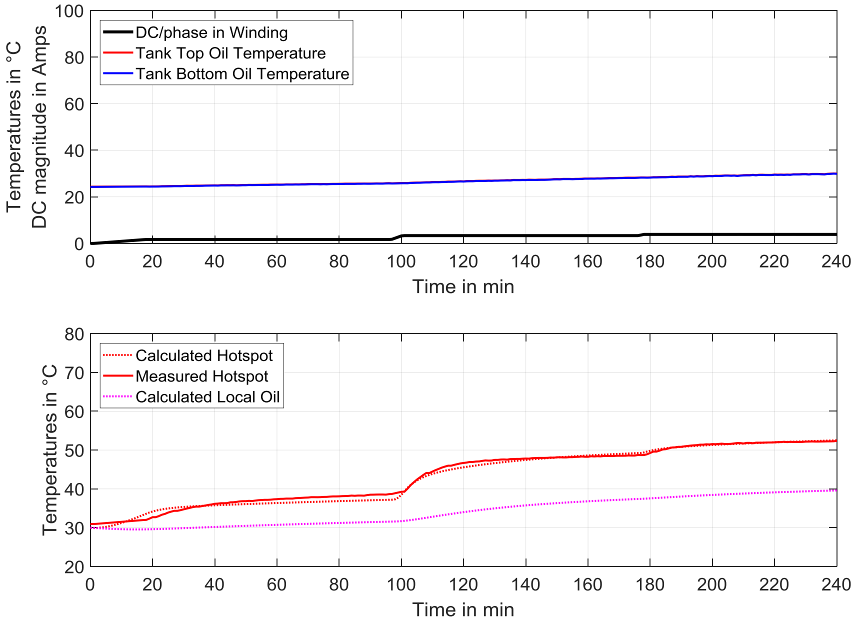

Figure 89: Results of hotspot test at Unit 3

Results of hotspot test at Unit 4

Table 34: Temperatures in steady-state conditions at Unit 4

DC current	**Hotspot sensor**		**Bottom oil**
-	Measured value	Deviation	Measured value
	°C	K	°C
5.0 A DC	51	+4	36
Average deviation during whole test period: +3.3 K			

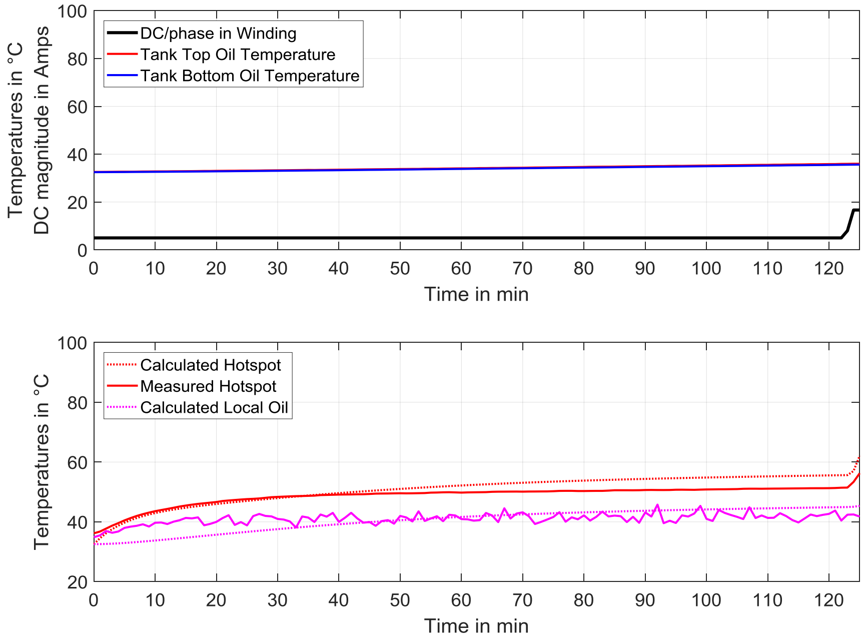

Figure 90: Results of hotspot test at Unit 4

Results of hotspot test at Unit 5

Table 35: Temperatures in steady-state conditions at Unit 5

DC current	Hotspot sensor		Bottom oil
-	Measured value	Deviation	Measured value
	°C	K	°C
16.7 A DC	36	-1	24
33.3 A DC	50	-2	25
50 A DC	60	-4	25
Average deviation during whole test period: -0.9 K			

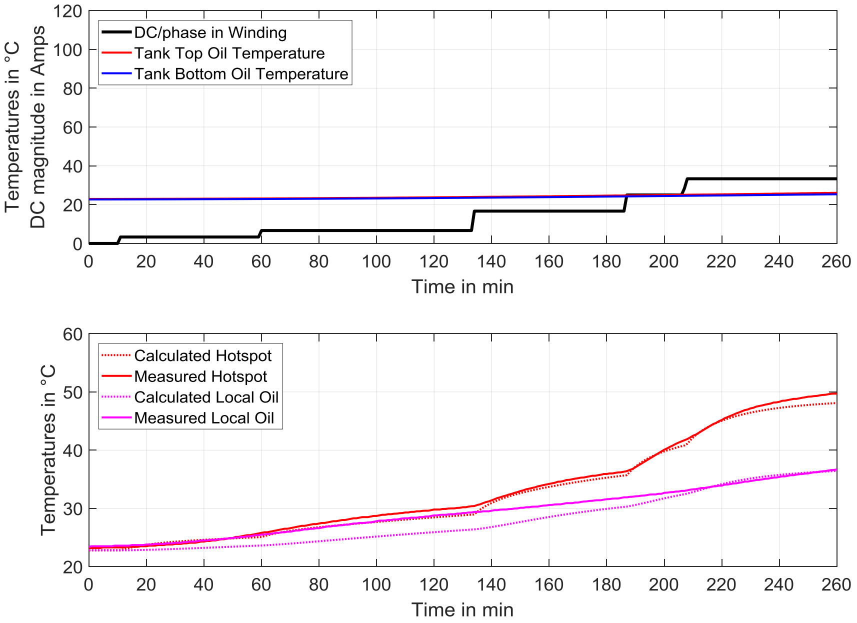

Figure 91: Results of hotspot test at Unit 5

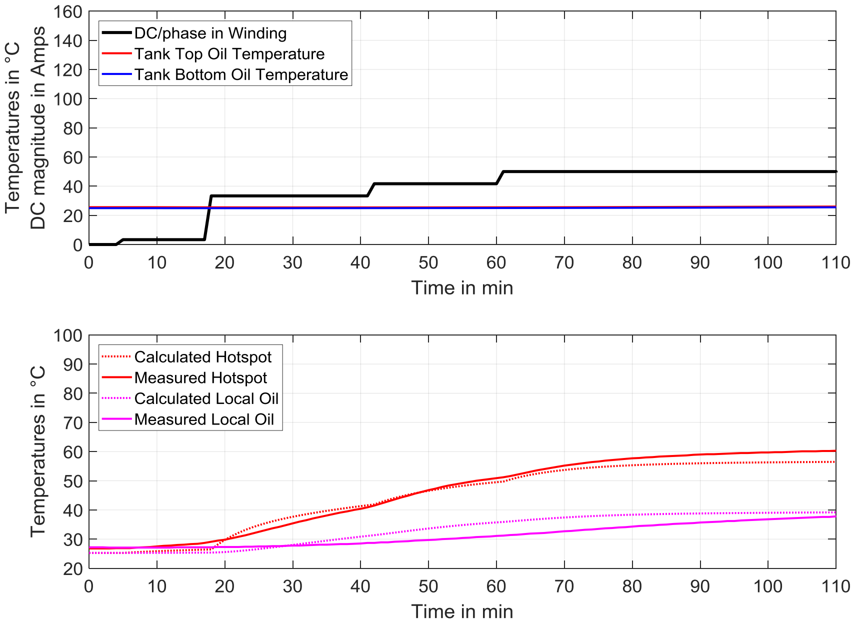

Figure 92: Results of second hotspot test at Unit 5

Appendix D – List of Figures

Figure 1: Idea of a design-specific risk assessment method for GIC effects 2
Figure 2: Yearly average sunspot numbers (1960-2010) [4] 3
Figure 3: Simplified flow of a Geomagnetically Induced Current (GIC) 4
Figure 4: Potential GIC profiles in grounded neutrals [24] 6
Figure 5: Disorder of nominal transformer operation due to DC [29] 7
Figure 6: Example of a grounded transformer winding with AC and DC excitation 7
Figure 7: Transient behavior of flux in a transformer core in case of an additional DC excitation – (a) DC voltage at neutral, (b) Flux density in core, (c) Exciting current in winding 8
Figure 8: Transient behavior of a hotspot temperature in case of an additional DC current in a transformer winding – (a) Additional DC current in the winding, (b) Observed increase of hotspot temperature in [32] 9
Figure 9: AC/DC hybrid transmission line [36] 10
Figure 10: Strategy to develop a design-specific risk assessment model for GIC effects 13
Figure 11: Classification of power transformers in respect to their GIC sensitivity 14
Figure 12: Sketch of Core-Type T1 (longitudinal section view) 14
Figure 13: Sketch of Core-Type T2 (longitudinal section view) 15
Figure 14: Sketch of Core-Type T3 (longitudinal section view) 15
Figure 15: Sketch of Core-Type T4 (longitudinal section view) 16
Figure 16: Sketch of Core-Type T5 (longitudinal section view) 16
Figure 17: Development procedure of a model to calculate harmonics (illustrated by the help of a T3 core transformer) 17
Figure 18: Approach for a simplified hotspot calculation model 18
Figure 19: Electro-Magnetic Modeling (Left: Electrical circuit of a winding, Center: Linkage to magnetic system, Right: Electro-magnetic model) 19
Figure 20: Unknown variables over a total time period 20
Figure 21: Matrix equation of an electro-magnetic model 20
Figure 22: Nonlinear B-H curve of magnetic material 21
Figure 23: Non-linear matrix equation of an electro-magnetic model 22
Figure 24: Electric circuit for single-phase transformers (one-wounded limb) 22
Figure 25: Electro-magnetic network for transformers with a T1 Core-Type 23
Figure 26: Simplified modeling of different transformer areas with magnetic resistances 23
Figure 27: Electrical circuit for single-phase transformers (two-wounded limbs) 26
Figure 28: Electro-magnetic network for transformers with a T2 Core-Type 26
Figure 29: Electro-magnetic network for transformers with a T4 Core-Type 27
Figure 30: Core saturation of different single-phase transformers due to additional DC – Exciting current with (a) 30 A DC and (b) 100 A DC per phase, Flux linkage of a T1 Core-Type with (c) 30 A DC and (d) 100 A DC per phase, Flux linkage of a T2 Core-Type with (e) 30 A DC and (f) 100 A DC per phase, Flux linkage of a T4 Core-Type with (g) 30 A DC and (h) 100 A DC per phase 29
Figure 31: Harmonics of exciting current due to additional DC in single-phase transformers – RMS value of (a) Fundamental, (b) 1st harmonic, (c) 2nd harmonic, (d) 3rd harmonic, (e) 4th harmonic, (f) 5th harmonic 29
Figure 32: Simplified saturation characteristic of single-phase units (Ψ-I curve) 30
Figure 33: Electrical circuit for three-phase transformers 31
Figure 34: Electro-magnetic network for transformers with a T3 Core-Type 32
Figure 35: Electro-magnetic network for transformers with a T5 Core-Type 32
Figure 36: Core saturation in T3 and T5 Core-Type transformers due to DC – (a) Exciting current of a (a) T3 Core-Type and (b) T5 Core-Type, Saturation of main limbs at a (c) T3 Core-Type and (d) T5 Core-Type, Saturation of yokes in a (e) T3 Core-Type and a (f) T5 Core-Type, (g) Saturation of return limbs of a T5 Core-Type ..35
Figure 37: Harmonics of exciting current due to DC at three-phase transformers – RMS value of (a) Fundamental, (b) 1st harmonic, (c) 2nd harmonic, (d) 3rd harmonic, (e) 4th harmonic, (f) 5th harmonic 36
Figure 38: Sketch of a DC test circuit 37

Figure 39: Measured currents: (a) I_{H1} – of high-voltage winding, (b) I_{L1} – of low-voltage winding, (c) $I_{ex,H}$ – Exciting current 37
Figure 40: Equivalent circuit diagram of a transformer 38
Figure 41: Measured vs. simulated exciting currents at (a) Unit 1 and (b) Unit 2 38
Figure 42: Increase of harmonics with DC (Measurement vs. Simulation) – RMS value of (a) Fundamental, (b) 1st harmonic, (c) 2nd harmonic, (d) 3rd harmonic, (e) 4th harmonic, (f) 5th harmonic 39
Figure 43: Measured voltages during DC experiment at (a) Unit 1 and (b) Unit 2 40
Figure 44: Measured vs. simulated exciting currents using measured voltage at (a) Unit 1 and (b) Unit 2 40
Figure 45: Test circuit for DC experiments with T3 Core-Type transformers 41
Figure 46: Currents in test circuit for the T3 Core-Type transformer: (a) $I_{H1,2,3}$ – high-voltage winding, (b) $I_{W1,2,3}$ – low-voltage winding, (c) $I_{ex1,2,3,HV}$ – Exciting current 42
Figure 47: Supply current of each phase in Unit 1 with (a) 75 A DC in neutral and (b) 90 A DC in neutral 43
Figure 48: Supply current of each phase in Unit 2 with (a) 35 A DC in neutral and (b) 40 A DC in neutral 43
Figure 49: Increase of fundamental reactive power of T3 Core-Type transformers (Measurement vs. Calculation) 44
Figure 50: Test circuit for a DC experiment with a T5 Core-Type transformer 45
Figure 51: Currents in test circuit for the T5 Core-Type transformer – (a) Current in HV winding, (b) Current in delta winding of LV system, (c) Exciting current with enhancements in addition to the major peaks 45
Figure 52: Exciting current of each phase in the tested T5 Core-Type transformer with (a) 5 A DC in neutral and (b) 20 A DC in neutral 46
Figure 53: Simplified calculation method for single-phase units 47
Figure 54: Simplified calculation for three-phase units with a T3 Core-Type 48
Figure 55: Zero-sequence impedances: (a) Common phenomenon vs. (b) DC phenomenon 49
Figure 56: Exciting current of a single-phase transformer determined by different methods with (a) 10 A DC per phase and (b) 50 A DC per phase 49
Figure 57: Exciting current in one phase of a three-phase transformer with a T3 core determined by different methods with (a) 3.33 A DC per phase and (b) 13.33 A DC per phase 50
Figure 58: Sketch of a T1 Core-Type with a tie bar on the main limb (half model) 53
Figure 59: Simplified temperature model for tie bars near by the core [29] 54
Figure 60: Energy equations of thermal model 54
Figure 61: Sketch of tie bar geometry (top view on cross section) 56
Figure 62: Eddy current distribution in a single tie bar due to core saturation (top view on cross section) 56
Figure 63: Extension of an electro-magnetic network with tie bar elements 57
Figure 64: (a) Calculated magnetic flux and (b) Eddy currents in different tie bar layers 58
Figure 65: Non-uniform loss distribution in tie bar along the height 58
Figure 66: Influence of tie bar design on (a) Loss density and (b) Hotspot temperature under DC 59
Figure 67: Influence of tank oil temperature on hotspot rise of tie bar above tank bottom oil (DC per phase = 50 A) 60
Figure 68: Location of temperature sensors and flux measure loops (Hotspot test no. 1) 60
Figure 69: Comparison of AC flux in the tie bar – 10 A DC per phase at (a) Center position and (b) Top position, 30 A DC per phase at (c) Center position and (d) Top position, 50 A DC per phase at (e) Center position and (f) Top position 61
Figure 70: Comparison of the RMS value of the tie bar flux over complete DC range: (a) Center position, (b) Top position 61
Figure 71: Calculated tie bar losses with the applied voltage during the DC experiment – (a) Increase of total losses with the DC level, (b) Loss distribution over the axial height 62
Figure 72: Comparison of (a) Center and (b) Top tie bar temperatures (measurement vs. simulation) [29] 63

Figure 73: Distorted applied voltage during a DC experiment: (a) Wave form and (b) Frequency spectrum with a THD of 9.9 % 64
Figure 74: Influence of voltage wave form on hotspot temperature: (a) THD of applied voltage, (b) Tie bar losses and (c) Hotspot temperature 65
Figure 75: Hotspot test at Unit 2: (a) Injected DC profile and (b) Resulting temperatures 66
Figure 76: Tie bar hotspot rise in different transformers (measurement vs. calculation) 67
Figure 77: Measured tie bar hotspot rises at different DC levels in different transformers ...68
Figure 78: Estimation of tie bar hotspot rise based on peak flux density in core main limb ..68
Figure 79: Increase of reactive power due to DC for different transformer designs 72
Figure 80: Examples of DC withstand capability curves – GIC effects are (a) in Design 1 neglected and (b) in Design 2 considered 73
Figure 81: Delay of GIC magnitudes due core flux behavior: (a) Total GIC profile, (b) Zoomed period between minute 6 and 14, (c) Zoomed period between minute 52 and 60 74
Figure 82: Example for the tie bar heating during GIC profiles: (a) GIC effects are neglected in the design, (b) GIC effects are considered in the design 75
Figure 83: Simplified GIC signature in [1] 76
Figure 84: Simplified DC profile to cover thermal behavior of a GIC storm 76
Figure 85: Screening criteria (based on Design 1) to evaluate GIC risks 77
Figure 86: Idea for a test setup for a DC test with load 79
Figure 87: Results of hotspot test at Unit 1 95
Figure 88: Results of hotspot test at Unit 2 96
Figure 89: Results of hotspot test at Unit 3 97
Figure 90: Results of hotspot test at Unit 4 97
Figure 91: Results of hotspot test at Unit 5 98
Figure 92: Results of second hotspot test at Unit 5 98

Appendix E – List of Tables

Table 1: Several GIC-caused problems in power grids.. 5
Table 2: Expected GIC effects according to IEEE C57.163...11
Table 3: Transformer susceptibility to the effect of GIC (IEEE C57.163) [1] 11
Table 4: Abstract of GIC-caused hotspot temperatures according to NERC [22].............12
Table 5: Calculation of variable magnetic resistances in the network of a T1 Core-Type .24
Table 6: Calculation of constant magnetic resistances in the network of a T1 Core-Type 24
Table 7: Technical data of single-phase transformers under investigation 27
Table 8: Design-specific parameter of single-phase transformers under investigation (lengths in the table are in [m], cross sections are in [m²])................................27
Table 9: DC flux distribution [in Vs] of Unit 1 (Core-Type T1) 28
Table 10: DC flux distribution [in Vs] of Unit 2 (Core-Type T2) 28
Table 11: DC flux distribution [in Vs] of Unit 3 (Core-Type T4) 28
Table 12: Relationship between air-core inductance and the exciting current 31
Table 13: Three-phase transformers under investigation 33
Table 14: Design-specific parameter of three-phase transformers under investigation (lengths in the table are in [m], cross sections are in [m²])................................33
Table 15: DC flux distribution [in Vs] of Unit 4 (Core-Type T3) 33
Table 16: DC flux distribution [in Vs] of Unit 5 (Core-Type T5) 34
Table 17: Technical data of tested single-phase transformers 38
Table 18: Harmonic analysis – Measurement vs. Simulation 39
Table 19: Technical data of tested three-phase transformers with a T3 Core-Type............42
Table 20: Technical data of tested three-phase transformer with a T5 Core-Type.............45
Table 21: Required transformer parameters for a simplified calculation 49
Table 22: Design-specific transformer parameters for loss investigation (lengths in the table are in [m], cross sections are in [m²])..55
Table 23: Different tie bar designs under investigation..59
Table 24: Temperatures at steady-state conditions (Hotspot Test no. 1)...........................63
Table 25: Overview of DC tested power transformers...65
Table 26: Temperatures at steady-state conditions at Unit 2...66
Table 27: Hotspot statistic – Measurement vs. Calculation 67
Table 28: Parameter to determine the delay of GIC due to the transient behavior of the core...74
Table 29: Parameter for a simplified DC profile to cover the heating of a GIC profile 77
Table 30: Overview of DC tested power transformers...95
Table 31: Temperatures in steady-state conditions at Unit 1...95
Table 32: Temperatures in steady-state conditions at Unit 2...96
Table 33: Temperatures in steady-state conditions at Unit 3...96
Table 34: Temperatures in steady-state conditions at Unit 4...97
Table 35: Temperatures in steady-state conditions at Unit 5...98